Search for New Mesons in Proton-Antiproton Annihilation into $\omega\pi^0\pi^0$ and $\omega\eta\pi^0$

Dissertation
zur
Erlangung der naturwissenschaftlichen Doktorwürde
(Dr. sc. nat.)
vorgelegt der
Mathematisch-naturwissenschaftlichen Fakultät
der
Universität Zürich

von
Peppino B. Giarritta
von
Schwyz

begutachtet von
Prof. Dr. Claude Amsler

Zürich 2000

Die vorliegende Arbeit wurde von der Mathematisch-naturwissenschaftlichen Fakultät der Universität Zürich auf Antrag von Prof. Dr. C. Amsler und Prof. Dr. P. Truöl als Dissertation angenommen.

Abstract

The aim of this thesis is to search for new meson resonances in antiproton-proton annihilation at rest into $\omega\pi^0\pi^0$ and $\omega\eta\pi^0$ in liquid hydrogen with high statistics data from the Crystal Barrel Experiment at LEAR (CERN). Samples of 136'023 $\omega\pi^0\pi^0$ and 34'064 $\omega\eta\pi^0$ events are reconstructed from 7γ data (via $\omega \to \pi^0\gamma$, $\pi^0 \to 2\gamma$ and $\eta \to 2\gamma$) leading to the annihilation rates $B(\overline{p}p \to \omega\pi^0\pi^0) = 2.71 \pm 0.36\,\%$ and $B(\overline{p}p \to \omega\eta\pi^0) = 1.06 \pm 0.18\,\%$.

The two data samples are then analyzed by Monte Carlo simulation using the K-matrix and helicity formalism and by a maximum likelihood fit to the data which is optimized for the high statistics data samples and takes into account the ω decay. The conventional helicity amplitudes have to be phase corrected for the spin of the ω in order to describe the interference between partial waves correctly.

The analysis of $\omega\pi^0\pi^0$ shows that the signal consists mainly of $\bar{p}p \to b_1(1235)\pi^0$ ($38\pm3\,\%$), $\bar{p}p \to \omega f_2(1270)$ ($17\pm4\,\%$) and $\bar{p}p \to \omega(\pi\pi)_S$ ($43\pm 2\%$) where $(\pi\pi)_S$ is the dipion S-wave. There is evidence for a state with the quantum numbers $J^{PC} = 1^{--}$ at a mass of 1738 ± 1 MeV and a width of 327 ± 63 MeV, decaying into $\omega\pi^0$, which agrees well the $\rho(1700)$.

The result of the analysis of $\omega\eta\pi^0$ is the first observation of an isospin zero axial vector ($J^{PC} = 1^{+-}$) state with a mass of 1382 ± 2 MeV and a width of 65 ± 14 MeV decaying into $\omega\eta$. Furthermore evidence for a vector ($J^{PC} = 1^{--}$) meson at 1698 ± 6 MeV and a width of 111 ± 4 MeV is found. Both, the axial vector $h_1'(1380)$ and the vector meson $\omega(1600)$, are necessary to describe the data which contains contributions from $\bar{p}p \to \omega(\pi\eta)_S$ ($81.5\pm4.1\,\%$), $\bar{p}p \to \omega a_2(1320)$ ($7.3\pm0.3\,\%$), $\bar{p}p \to b_1(1235)\eta$ ($3.9\pm0.6\,\%$), $\bar{p}p \to h_1'(1380)\pi^0$ ($0.80\pm0.25\,\%$) and $\bar{p}p \to \omega(1600)\pi^0$ ($5.0\pm1.0\,\%$).

The $h_1'(1380)$ is compatible with the state reported by LASS and Crystal Barrel in the $K\overline{K}^*$ decay mode. The axial vector state is described by a Flatté amplitude which couples to the $\omega\eta$ and the $K\overline{K}^*$ systems. The mass and the measured ratio of couplings $R = g^2_{\omega\eta}/g^2_{K\overline{K}^*} = 1.6 \pm 0.6$ are compatible with the missing isoscalar of the axial vector nonet whose $SU(3)$ singlet-octet mixing angle is determined to be $\theta_A = -5.8^{+2.7}_{-1.6}\,{}^\circ$.

Zusammenfassung

Die Zielsetzung dieser Doktorarbeit ist die Suche nach neuen mesonischen Resonanzen in den Endzuständen $\omega\pi^0\pi^0$ und $\omega\eta\pi^0$ aus der Antiproton-Proton-Vernichtung in Ruhe in flüssigem Wasserstoff mit Hochstatistik-Daten des Crystal Barrel Experimentes am LEAR (CERN). Datensätze bestehend aus 136'023 $\omega\pi^0\pi^0$ und 34'064 $\omega\eta\pi^0$ Ereignissen werden aus 7γ Daten (via $\omega\to\pi^0\gamma$, $\pi^0\to 2\gamma$ und $\eta\to 2\gamma$) rekonstruiert, wobei die Annihilationsraten $B(\overline{p}p\to\omega\pi^0\pi^0) = 2.71 \pm 0.36\,\%$ und $B(\overline{p}p\to\omega\eta\pi^0) = 1.06 \pm 0.18\,\%$ gemessen werden.

Die zwei Datensätze werden durch Monte Carlo Simulation mittels K-Matrix und Helizitätsformalismus und einer Maximum Likelihood Anpassung der Daten, die für Hochstatistik-Daten optimiert ist und den ω-Zerfall einbezieht, untersucht. Die konventionellen Helizitätsamplituden müssen, um die Interferenz zwischen Partialwellen korrekt zu beschreiben, aufgrund des ω-Spins Phasen korrigiert werden.

Die Analyse von $\omega\pi^0\pi^0$ zeigt, dass das Signal hauptsächlich aus $\bar{p}p\to b_1(1235)\pi^0$ ($38\pm3\,\%$), $\bar{p}p\to\omega f_2(1270)$ ($17\pm4\,\%$) und $\bar{p}p\to\omega(\pi\pi)_S$ ($43\pm 2\%$) besteht, wobei $(\pi\pi)_S$ die Dipion S-Welle ist. Es gibt Evidenz für einen Zustand mit den Quantenzahlen $J^{PC} = 1^{--}$ bei einer Masse von 1738±1 MeV und einer Breite von 327±63 MeV, welcher in $\omega\pi^0$ zerfällt und gut mit dem $\rho(1700)$ übereinstimmt.

Ergebnis der Untersuchung von $\omega\eta\pi^0$ ist die Erstbeobachtung eines Isospin null Axialvektor Zustandes mit der Masse von 1382 ± 2 MeV und der Breite von 65 ± 14 MeV, welcher in $\omega\eta$ zerfällt. Im weiteren finden wir Evidenz für ein Vektormeson bei 1698±6 MeV und einer Breite von 111±4 MeV. Beide, das Axialvektormeson $h_1'(1380)$ und das Vektormeson $\omega(1600)$, sind notwendig zur Beschreibung der Daten, welche Beiträge von $\bar{p}p\to\omega(\pi\eta)_S$ ($81.5\pm4.1\,\%$), $\bar{p}p\to\omega a_2(1320)$ ($7.3\pm0.3\,\%$), $\bar{p}p\to b_1(1235)\eta$ ($3.9\pm0.6\,\%$), $\bar{p}p\to h_1'(1380)\pi^0$ ($0.80\pm0.25\,\%$) und $\bar{p}p\to\omega(1600)\pi^0$ ($5.0\pm1.0\,\%$) enthalten. Das $h_1'(1380)$ stimmt mit dem Zustand überein, der von LASS und Crystal Barrel im $K\overline{K}^*$-Zerfallsmodus beobachtet wurde. Der Axialvektor Zustand wird mit einer Flatté Amplitude, die zu den Systemen $\omega\eta$ und $K\overline{K}^*$ koppelt, beschrieben. Die Masse und das gemessene Verhältnis der Kopplungen $g^2_{\omega\eta}/g^2_{K\overline{K}^*}=1.6\pm0.6$ sind verträglich mit dem fehlenden Isoskalar des Axialvektor-Nonetts, dessen $SU(3)$ Singulett-Oktett Mischungswinkel mit $\theta_A = -5.8^{+2.7}_{-1.6}\,^\circ$ bestimmt ist.

I don't know anything, but I do know that everything is interesting if you go into it deeply enough.

Richard P. Feynman [1]

Contents

1 Introduction

Meson spectroscopy has the aim to find and to classify the strongly interacting particles (hadrons) with integer spin. These particles are explained as bound states of a quark and an antiquark. Nevertheless, according to *Quantum Chromodynamics* (QCD), the existence of non $\overline{q}q$ mesons (exotic states) is allowed by this theory and many models based on QCD predict such states. In particular one expects states with gluonic degrees of freedom, mesons composed only of gluons (glueballs) or mixtures of quarks and gluons (hybrids), to populate the low mass region of the hadronic spectrum. Gluons, the vector bosons mediating the strong interaction, play a key rule in the understanding of the hadronic world. Nowadays, it is one of the most challenging tasks in light-meson spectroscopy to search for this new form of hadronic matter.

The mass predictions for exotic states are quite model dependent and experimentally it is very difficult to identify such states directly. Establishing and classifying mesons into the conventional $SU(3)$ $q\overline{q}$ multiplet scheme is therefore an important issue which helps to identify surplus states with exotic character.

One of the purposes of the Crystal Barrel Experiment is to search for exotic states in antiproton-proton annihilation. Recent results from Crystal Barrel and other experiments support the $f_0(1500)$ to be the ground state scalar glueball [2][3] and confirm the existence of the $\hat{\rho}(1405)$ with exotic (non-$q\overline{q}$) quantum numbers 1^{-+} [4]. While many resonances decay to $\pi\pi$, $K\overline{K}$ or $\eta\pi$, only very few resonances have been reported to decay into $\omega\pi$ [8] and only recently evidence for resonances decaying into $\omega\eta$ was found [5]. Various predictions support further states in these channels, which need experimental confirmation (see section 1.2).

It is the aim of this work to investigate new resonances decaying into $\omega\pi$ and $\omega\eta$ by analyzing the reaction $\overline{p}p \to \omega\pi^0\pi^0$ and $\overline{p}p \to \omega\eta\pi^0$ with the Crystal Barrel Experiment (section 2). These reactions are selected and reconstructed in the 7γ final state (section 4). Selection efficiencies and the detector acceptance are studied using Monte Carlo simulations (section 5), and different methods are used to determine the background in the selected samples (section 6).

The spin-parity analysis (section 8) is based on maximum likelihood fits and includes (i) the full ω decay information, (ii) corrected helicity amplitudes for final state particles with spin (section 8.2), (iii) free mass and width fitting, (iv) K-matrix parameterization for the $(\pi\eta)_S$ and $(\pi\pi)_S$ wave and (v) ${}^1P_1$ and ${}^3S_1$ $\bar{p}p$ initial states. As far as we know, the helicity amplitude correction developed in this work is introduced for the first time in the analysis of three body annihilation.

1.1 $q\bar{q}$ Mesons

In 1964, Gell-Mann, Ne'eman and Zweig introduced quarks into particle physics to classify the large number of observed hadrons [6] [7]. Mesons made of the light quarks u(up), d(down), s(strange) group in $q\bar{q}$ nonets of $SU(3)_f$ with quantum numbers J^{PC}. $SU(3)_f$, the underlying flavor (u,d,s) symmetry of the strong interaction, connects isospin (I,I_3) and strangeness S.

The $q\bar{q}$ nonet splits into an octet and a singlet ($3 \otimes \bar{3} = 8 \oplus 1$). The octet consists of an isotriplet ($I = 1$), two isodoublets ($I = \frac{1}{2}$) with strangeness $S = \pm 1$ and an isosinglet ($I = 0$) (see table 1).

I	I_3	S	Q	$q\bar{q}$ representation		
1	+1	0	-1	$d\bar{u}$		octet
1	0	0	0	$(d\bar{d} - u\bar{u})/\sqrt{2}$		
1	-1	0	+1	$u\bar{d}$		
$\frac{1}{2}$	$+\frac{1}{2}$	+1	+1	$u\bar{s}$		
$\frac{1}{2}$	$-\frac{1}{2}$	+1	0	$d\bar{s}$		
$\frac{1}{2}$	$+\frac{1}{2}$	-1	-1	$\bar{u}s$		
$\frac{1}{2}$	$-\frac{1}{2}$	-1	0	$\bar{d}s$		
0	0	0	0	$(u\bar{u} + d\bar{d} - 2s\bar{s})/\sqrt{6}$	$= \psi_8$	
0	0	0	0	$(u\bar{u} + d\bar{d} + s\bar{s})/\sqrt{3}$	$= \psi_1$	singlet

Table 1: *The $q\bar{q}$ $SU(3)_f$ nonet*

Due to the mass hierarchy of the quarks $m_u \approx m_d < m_s$ the $SU(3)$ symmetry is broken. The isoscalar octet and singlet can mix. The observed isosinglets ψ, ψ' are mixture of the octet state ψ_8 and the singlet state ψ_1:

$$\psi = \psi_8 \sin\theta + \psi_1 \cos\theta \quad (1)$$

$$\psi' = \psi_8 \cos\theta - \psi_1 \sin\theta \quad (2)$$

Octet-singlet mixing affects masses and partial decay widths of mesons and plays therefore an important role for the assignment of the observed states into the nonet scheme [8] [9]. At the ideal mixing angle $\theta_i = 35.3°$, ψ becomes $\frac{1}{\sqrt{2}}(u\bar{u} + d\bar{d})$ and ψ' a pure $-s\bar{s}$ state. The latter is not allowed to decay into pure u,d states. due to the Okubo-Zweig-Iizuka rule.

In addition to the octet-singlet mixing other mixing schemes can be introduced to explain the observed masses and widths of $\overline{q}q$ states, for instance the ground state glueball 0^{++} could mix with the isoscalars of the scalar nonet [2].

Parity and C-parity of the $q\bar{q}$ nonet are those of a fermion-antifermion system and are given by

$$P = (-1)^{L+1} \tag{3}$$

$$C = (-1)^{L+S} \tag{4}$$

where L denotes the orbital angular momentum of the $q\bar{q}$ with spin $S = 0, 1$. The allowed numbers J^{PC} for $L = 0, 1, 2$ are listed in table 2 below. The states occur as ground state (N=1) as well as radial excitations (N>1). Figure 1 shows the nonets with $L = 0, 1, 2$ of the known light mesons spectrum up to the first radial excitations for $L = 0$ and $L = 1$.

The 0^{++} and 1^{+-} ground state nonets are still not fully established. There is controversy in the assignment of the 0^{++} nonet, which is important for establishing the scalar ground state glueball. The $f_0(1700)$, still an open issue, might be the missing $s\bar{s}$ state and the $f_0(1500)$ – due to its coupling to $K\bar{K}$ and $\pi^0\pi^0$ – is most likely the ground state 0^{++} glueball [2].

A candidate for the $s\bar{s}$ member of the 1^{+-} nonet (see figure 2) is the $h_1'(1380)$, reported by LASS [10] and Crystal Barrel [11] in the $K^*\overline{K}$ decay mode, but whose isospin has not been measured unambiguously.

1.2 Resonances in $\omega\pi$ and $\omega\eta$

The channels $\omega\eta$ and $\omega\pi^0$ have negative C-parity and are interesting to access mesons with quantum numbers $J^{PC} = 1^{--}$, 1^{+-}, 2^{--}, 3^{--} or the exotic states 0^{--} and 2^{+-}.[1] In contrast to kaonic channels the isospin is well defined, namely $I = 0$ respectively $I = 1$. The vector nonet is nearly ideally mixed and therefore ω is almost u,d, which makes both channels insensitive to $s\bar{s}$ components.

The $\omega\pi$ system is interesting for the study of vector mesons with isospin $I = 1$. $\rho(1440)$ was observed in $e^+e^- \to \omega\pi$ [12] and might be the first radial excitation of $\rho(770)$. The $\rho(1700)$ also seen in this reaction [13] might belong to the $L = 2$ orbital excitation of the vector nonet (see figure 1). In contrast to these resonances, $\rho(1270)$[14] and the narrow $C(1480)$[15] are controversial. The latter is suggested to be an exotic vector meson [16].

The structure of the ρ states is not completely clear and further experimental information is needed (see mini-review in [8]). The $\rho(1450)$ and the $\rho(1700)$ have been observed by Crystal Barrel in $\bar{p}p$ annihilation via their $\pi\pi$ and $K\overline{K}$ decay modes [17][18].

---

[1] The exotic 0^{+-} state cannot decay into a vector (ω) and a pseudo vector (π^0) because of angular momentum conservation.

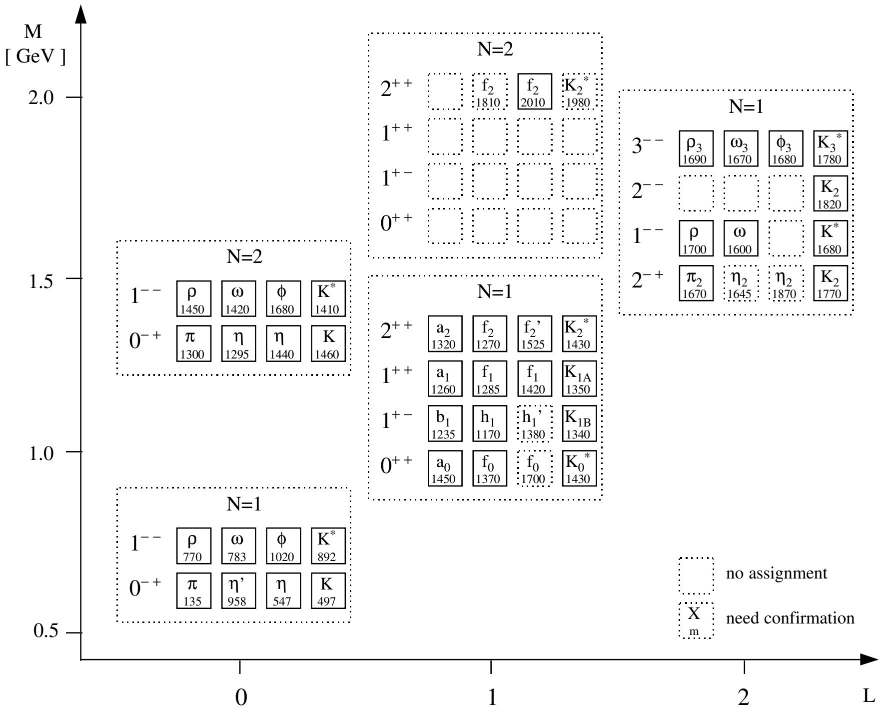

Figure 1: *The light meson spectrum according the $SU(3)_f$ quark model. L is the orbital angular momentum of the $q\bar{q}$ system, N the radial excitation and M denotes the approximative mass scale. States of the same nonet are horizontally aligned: The first square represents the isovectors (3 states), the second and third squares the two isosinglets and the fourth the two isodoublets (4 states).*

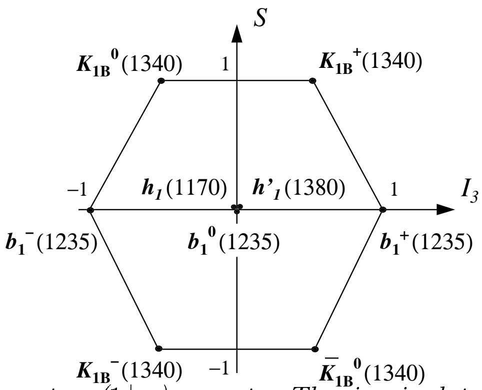

Figure 2: *The axial vector (1^{+-}) nonet. The isosinglet states are occupied by $h_1(1170)$ and presumably by $h'_1(1380)$. $K_{1B}(1340)$ is a nearly equal (45°) mixing of $K_1(1270)$ and $K_1(1400)$ [8, 19].*

The $b_1(1235)$ decays dominantly to $\omega\pi$. The ratio of the decay amplitudes of $L = 2$ and $L = 0$ (D/S) is a sensitive test for the two competing models for strong hadronic decays: the $^3P_0$ and the $^3S_1$ models [20].

The channel $\omega\eta$ is very appealing in a search for axial vector mesons. Ref. [21] predicts $h'(1380)$ to decay to this channel. And, like $\rho(1450)$, one expects the first radial excitation of the $\omega(782)$ around 1420 MeV to decay into $\omega\eta$ [22].

Recently a BNL experiment [5] found evidence for a $h'_1(1540)$ and observed $\omega(1600) \to \omega\eta$ in the reaction $\pi^-p \to \pi^+\pi^-4\gamma n$ at 18 GeV/c. Both states need confirmation. One of them could be the state at mass of 1610 MeV/c^2 with width of 230 MeV/c^2 reported in $\gamma p \to \omega\eta p$ from diffractive photoproduction by photons of 25-50 GeV [23]. $X(1650)$ is the only particle which is reported by PDG [8] to decay into $\omega\eta$. It was observed by GAMS [24] in the reaction $\pi^-p \to \omega\eta n$ at a mass of 1652 MeV/c^2 and a width of less than 50 MeV/c^2; spin and parity of this surprisingly narrow state are unknown.

1.3 Resonances in $\pi^0\pi^0$ and $\eta\pi^0$

The low mass 0^{++} mesons decaying into $\pi\pi$ are relatively wide and couple to channels ($\bar{K}K$ and $\eta\eta$) which open near the resonance masses. Similarly, in the $\eta\pi$ S-wave, the $a_0(980)$ decaying also to $\bar{K}K$ is shaped by the $\bar{K}K$ threshold. Therefore both, the $(\pi\pi)_S$ and $(\pi\eta)_S$ waves, cannot be described satisfactorily by superposing Breit-Wigner amplitudes.

The coupled channel parameterization achieved in the analyses [18] and [25] lead to a better understanding of the $(\pi\pi)_S$ and $(\pi\eta)_S$ waves produced in antiproton-proton annihilation with a recoiling scalar meson (π^0 or η). The $(\pi\pi)_S$ wave is described in terms of a 3×3 K-matrix including the channels $\pi\pi$, $\eta\eta$ and $\bar{K}K$ and poles for σ, $f_0(980)$, $f_0(1370)$ and $f_0(1500)$. The $(\pi\eta)_S$ wave is described in terms of a 2×2 K-matrix with the channels $\eta\pi$ and $\bar{K}K$ and poles for $a_0(980)$ and $a_0(1450)$ (see section 8.3).

1.4 Antiproton-Proton Annihilation at Rest

In annihilation at rest, the $\bar{p}$ is captured by the p and forms a $\bar{p}p$ atom (protonium). The capture occurs typically at principal quantum number $n \approx 30$. The de-excitation takes place (i) by cascade to lower levels by x-ray or external Auger electron emission and (ii) by Stark mixing of angular momenta due to collisions with neighboring molecules (H_2) in the target. At angular momenta l=0 and 1 the atomic wave functions have enough overlap for annihilation.

In liquid hydrogen, Stark mixing dominates and annihilation can already occur at higher n with $l = 0$ (S-state annihilation). The overall fraction of P-state annihilation was determined to be $(13 \pm 4)\%$[26]. The conservation of J, P- and C-parity restricts the number of initial states considerably (see table 2). Due to the negative C-parity of $\omega\pi^0\pi^0$ and $\omega\eta\pi^0$ only contribution from $^3S_1$ and $^1P_1$ are possible.

The $\bar{p}p$ annihilation mechanism into mesons is not well understood [27]. Explanations have to be found in the framework of nonperturbative QCD and are therefore model dependent. Experimentally, the naive quark model assuming only quark line rule and dominance of two-meson annihilation (isobar model) seems to be a fairly good approximation for the measured two-body branching ratios [27]. In particular, the quark line rule forbids annihilation into $s\bar{s}$ mesons (Okubo-Zweig-Iizuka, OZI rule). Nevertheless states with $s\bar{s}$ contents are produced via octet-singlet mixing. The enhancement of the ϕ production in $\bar{p}p$ annihilation, however, cannot be explained by mixing and may be a hint for a strangeness component in the proton [27, 28].

		J^{PC} $(^{[2S+1]}L_J)$			
L	S	J=0	J=1	J=2	J=3
0	0	0^{-+} $(^1S_0)$			
0	1		1^{--} $(^3S_1)$		
1	0		1^{+-} $(^1P_1)$		
1	1	0^{++} $(^3P_0)$	1^{++} $(^3P_1)$	2^{++} $(^3P_2)$	
2	0			2^{-+} $(^1D_2)$	
2	1		1^{--} $(^3D_1)$	2^{--} $(^3D_1)$	3^{--} $(^3D_3)$

Table 2: *Quantum numbers of a antifermion-fermion system with angular momenta L=0,1,2, in* J^{PC} *and in atomic physics notation (brackets)*

1.5 Previous Investigation of $\bar{p}p \rightarrow \omega\pi^0\pi^0$ and $\bar{p}p \rightarrow \omega\eta\pi^0$

Due to the excellent efficiency for neutral particle detection, both annihilation channels had been investigated for the first time in the Crystal Barrel Experiment. The analyses [29][30] had revealed the dominant contributions: $\omega\pi^0\pi^0$ contains $b_1(1235)$, $(\pi\pi)_S$ wave and $f_2(1270)$ while $\omega\eta\pi^0$ contains $a_0(980)$, $a_2(1320)$ and $b_1(1235)$. However, the data could not be described satisfactorily for the $\pi\pi$ invariant mass around 1000 MeV/c^2 and in $\omega\eta$ around 1400 MeV/c^2. This may indicate that contributions from further resonances are needed. The results presented in this work exploit a much larger data sample and an improved analysis procedure including information from the ω decay.

The annihilation into $\omega\pi^0\pi^0$ can be compared with the reaction $\bar{p}p \to \omega\pi^+\pi^-$ which was investigated in bubble chamber measurements at the end of the 60's [31]. In contrast to the neutral mode, this channel has a strong contribution from $\rho(770) \to \pi^+\pi^-$. Several attempts have been made to clarify the structure of the $\omega\pi$ spectrum, finding some evidence for a radial excitation of the ρ meson around 1250 MeV/c^2 [32] [33]. These analyses showed (i) that the shape of the $(\pi\pi)_S$ wave plays a crucial role in the analysis of the data and (ii) that the angular decay distribution of the ω is sensitive to the assumed contributions.

The reaction $\bar{p}p \to \omega\pi^+\pi^-$ had also been investigated by the ASTERIX collaboration in gaseous hydrogen where P-state annihilation contributes strongly, but no evidence for higher ρ meson states was found [34].

2 The Crystal Barrel Experiment at LEAR

The Crystal Barrel Experiment at LEAR (CERN) was designed to study low-energy antiproton-proton annihilation in liquid and gaseous hydrogen and liquid deuterium with very high statistics. In contrast to previous experiments, the Crystal Barrel spectrometer allows to detect at the same time charged as well as neutral decay products. This capability enables the study of final states involving neutral particles which could not be investigated until then, namely those involving more than one π^0 or η which each have strong branching ratios to pure γ final states.

The detector covers almost the full 4π solid angle, has a good energy and angular resolution and a trigger system to access annihilation channels with low branching ratios. The aim of the experiment consists mainly of

- spectroscopy of conventional meson resonances in the framework of $SU(3)$ nonet classification,
- search for non-$q\bar{q}$ mesons like glueballs or hybrids, which are predicted by several nonperturbative QCD models,
- measurements of branching ratios of primary $\bar{p}p$ decay products in order to test annihilation models in the low-energy regime of QCD.

Data taking started in 1989 and ended at the end of 1996. The following description of the apparatus focuses on the experimental setup the data presented in this thesis were taken with.

The overall layout of the Crystal Barrel detector [35] is show in figure 3. Antiprotons coming from LEAR annihilate in the liquid hydrogen target which is surrounded by two cylindric proportional wire chambers (PWC_1 and PWC_2) and a jet drift chamber (JDC), for tracking of charged particles, and a barrel-shaped calorimeter consisting of 1380 CsI(Tl) crystals. A solenoidal magnet provides a field of 1.5 T in the inner part of the apparatus, optimized for the momentum determination of charged tracks in the JDC.

2.1 Antiproton Beam

The antiprotons were extracted from the Low Energy Antiproton Ring (LEAR) which was in operation till 1996 and a part of the PS Complex at CERN [36] (fig. 4).

The beam momenta of the antiprotons ranged from 100 MeV/c to 2 GeV/c and typical beam intensities were about 10^4 to $10^6\,\bar{p}$/s, both depending on whether measurements for stopping antiprotons (annihilation at rest) or interaction in flight were being made.

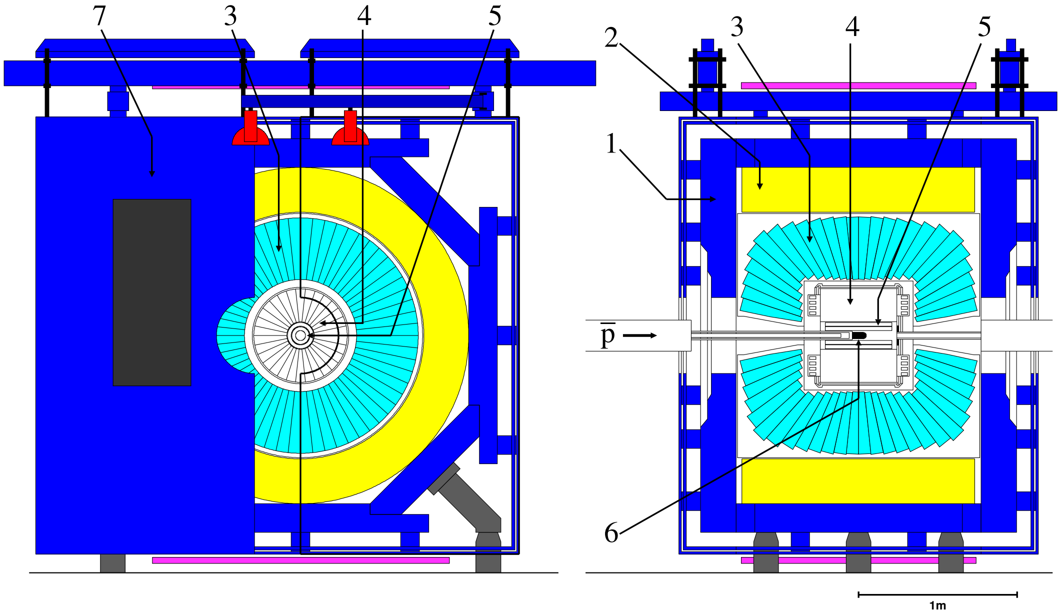

Figure 3: *Overall layout of the Crystal Barrel detector consisting of following main components: (1) magnet yoke, (2) magnet coils, (3) CsI barrel, (4) jet drift chamber, (5) proportional chamber (begin 1996 replaced with the silicon vertex detector) (6) the liquid hydrogen target and (7) half of the magnetic endplate.*

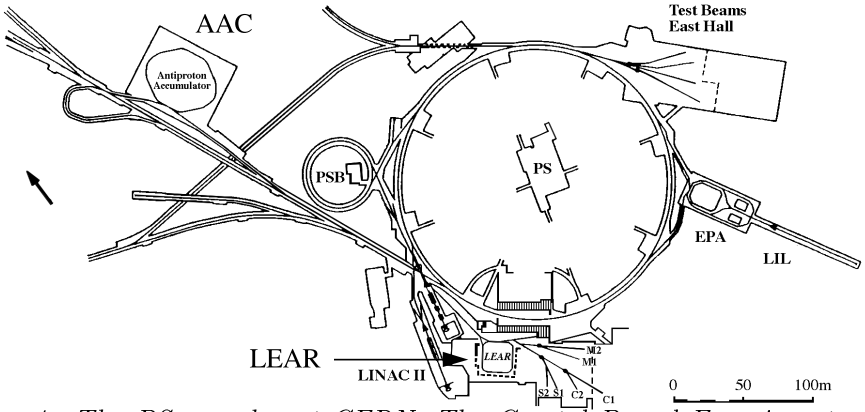

Figure 4: *The PS complex at CERN. The Crystal Barrel Experiment was located at C2, in the experimental area of LEAR.*

The antiprotons were produced in the Antiproton Accumulation Complex (AAC) by bombardment of a $\bar{p}$ conversion target with 26 GeV/c protons, which were fast extracted from the Proton Synchrotron (PS). The antiprotons with a typical momentum of 3.5 GeV/c were directed to the Antiproton Collector (AC), where they were stochastically cooled for 4.8 s, and subsequently transfered and stocked in the Antiproton Accumulator (AA). This procedure allowed to stock clean samples of antiprotons with a narrow spread in phase space. Up to 10^{12} antiproton were stored in the AA.

From the AAC, a few times per hour, a single bunch of 2×10^9 to $5 \times 10^{10}\,\bar{p}$ was returned to the PS, decelerated down to 600 MeV and sent to LEAR, where the beam was accelerated or slowed down to the choosen extraction momentum (100 MeV/c to 2 GeV/c) and permanently cooled by stochastic- (momentum above 350 MeV/c) or electron-cooling (momentum below 350 MeV/c) with a momentum spread of $\Delta p/p \approx 10^{-4}$. The antiproton beam from LEAR lasted for up to about 3 hours, after which refilling from the antiproton accumulator (AA) was necessary.

2.2 Liquid Hydrogen Target

The liquid hydrogen target is 17 mm in diameter and 44 mm long. Antiprotons with a beam momentum of 200 MeV/c stop in the target center with a longitudinal spread of about 0.6 mm.

2.3 The Proportional Wire Chambers (PWC)

The two cylindrical proportional wire chambers (PWC_1, PWC_2) are used to trigger on the final-state charged multiplicity and provide additional tracking information (r, ϕ) for charged particles coming from the target. Both chambers have a wire length of 35 cm. The anode wires (15 μm diameter goldplated tungsten) are at a radius of 25.5 mm and 43 mm respectively and run parallel to the magnetic field. The coverage reaches 99 % of 4π for the inner and 97 % for the outer chamber. The detection effiency for minimum ionizing particles was determined to be better than 99 %.

2.4 The Jet Drift Chamber

Tracks of charged particles are detected by the cylindrical jet drift chamber (JDC). The chamber consists of 30 azimuthal sectors and 23 radial layers of sense wires which are each read out one both ends. The chamber has a diameter of 51 cm and length of 40 cm. The innermost (outermost) sense wire is at a radius of 63 mm (239 mm), with a sensitive length of 399 mm giving a solid angle coverage of 95%

of 4π. A $\pm 200\,\mu$m azimuthal staggering of the sense wires allows to resolve the left-right ambiguity in track reconstruction. The segmentation of the drift chamber keeps the drift times relatively short, but allows a sufficiently large ionization signal to provide a dE/dx separation for $K^{\pm}$ and $\pi^{\pm}$. The z coordinate (along the wire) of a charge deposit (hit) is determined by evaluating the two measured amplitudes A_- and A_+.

$$z = z_0 + z_L \frac{A_+ - \alpha A_-}{A_+ + \alpha A_-} \tag{5}$$

where z_0 is the location of the center of the wire, z_L the electrical length and α the relative gain. Each of the 690 sense wires have their own z_0, z_L and α which have to be adjusted for each run period. This is done by a calibration based on data taken without magnetic field. Accordingly, a $r - \phi$ calibration is need for the conversion of drift times into r and ϕ positions of hits in the chamber.

Track reconstruction starts with a pattern recognition algorithm which associates hits into track segments. After resolving the left-right ambiguity of the tracks and the matching of broken track segments, a helix fitting algorithm gives the particle's charge, its momentum and the position of closest approach to z-axis.

2.5 The Electromagnetic Calorimeter

The reconstruction of neutral decays of π^0, η or ω needs a photon detection with high efficiency and good energy and spatial resolution over an energy range of 4 MeV to 2 GeV. The shower calorimeter built for this purpose is a modular barrel shaped detector system covering 97% of the 4π solid angle.

1380 CsI(Tl) crystals are arranged in 26 rings around the JDC, covering the polar angles from 12° to 168°. Each crystal has a length of 300 mm, corresponding to 16.1 radiation lengths, and an angular coverage of 6° in polar and azimuthal angles, respectively, 12° at small and large polar angles ($\theta < 30^\circ$ and $\theta > 150^\circ$), corresponding to the three rows closest to the beam axis on each side. The distance of the crystals to the annihilation vertex varies from about 270 mm to 380 mm. Figure 5 sketches the barrel like structure of the calorimeter.

Because the calorimeter is placed inside a 1.5 T magnetic field, the scintillator light is read out by photodiodes, instead of conventional photomultiplier tubes. The light emitted by the crystals peaks at about 550 nm and is absorbed and re-emitted at a longer wavelength by a wavelength-shifter (3 mm Plexiglas tile doped with an optically active pigment) and subsequently collected by a silicon photodiode glued to one lateral face of the Plexiglas tile (see figure 6). Besides of re-emitting the light in a spectral range where the quantum efficiency of the diode is higher, the wavelength-shifter has the advantage of concentrating the light onto the active area of the photodiode. Table 3 summarizes the properties of the CsI calorimeter.

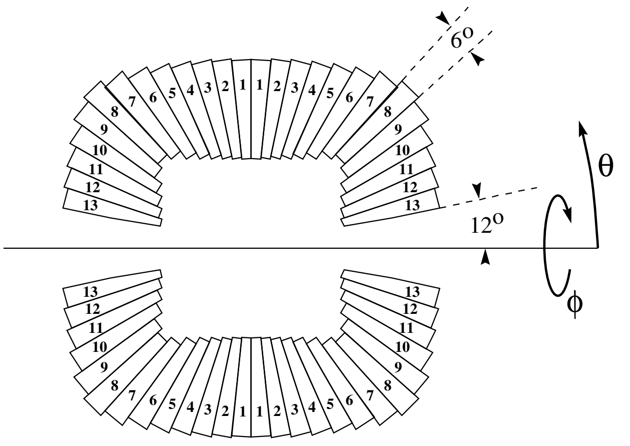

Figure 5: *Segmentation of the Crystal Barrel calorimeter*

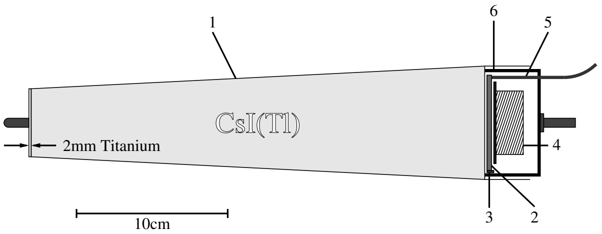

Figure 6: *Cross-section of a CsI(Tl) module: (1) 0.1* mm *titanium can, (2) wavelength-shifter, (3) photodiode, (4) preamplifier, (5) light fiber (6) brass cover*

The signals from the photodiodes are individually amplified by charge sensitive preamplifiers with a differential driver stage, driving a 20 m long twisted-pair line. The shaping amplifier then generates a Gaussian like pulse with a width of about 4 μs. Two ADC systems, operating in parallel but in different ranges, digitize the analog signals. The LeCroy 2282 system with 4096 channels and a range of 0-400 MeVgives high sensitivity (0.1 MeV/channel). The LeCroy 4300-B FERA system with 2048 channels covers the full range (0-2000 MeV) and provides a fast readout for the software trigger.

In addition, a leading edge discriminator is connected to the shaping amplifier

Calorimeter	
General layout	barrel configuration
Solid angle	97 % of 4π
Polar angle range [deg]	12 - 168
Cavity length [mm]	540
Cavity radius [mm]	270
Number of crystals	1380
Azimuthal segmentation	26 crystals
Polar segmentation	60 (30) crystals
Active length [mm]	300 (16,1 L_R)
Readout	WLS and photodiode
Properties of CsI(Tl) scintillator	
Density [g/ cm^3]	4.53
Radiation length L_R [cm]	1.86
Molière Radius [cm]	3.8
Maximum emission	at 550 nm
Decay times [μs]	0.9 and 7
Photon yield/ MeV	4.5 $\times 10^4$

Table 3: *Specification of the Crystal Barrel calorimeter*

and is used for the Fast Cluster Encoder (FACE).

A light pulser system allows to monitor the gain stability of the calorimeter. The light from a Xenon flashlamp is distributed via glass fibers to the wavelength-shifter of the CsI crystals and subsequently read out by the calorimeter electronics.

2.6 The Trigger System

The trigger system consists of three levels. The level 0 trigger gives the start signal for the electronics and is defined by an incoming antiproton with entrance counters providing the timing.

Level 1 combines the start signal with the information of charged multiplicity of the two PWC's and the JDC and/or the total multiplicity of the calorimeter determined by the Fast Cluster Encoder. For fast multiplicity decision in the JDC, only six layer (2,3,4,5,20 and 21) are used.

Level 2 is a software trigger using the calorimeter readout microprocessor to determine photon clusters and invariant masses of $\gamma\gamma$ combinations in order to select particular final states decaying to photons.

The "zero-prong“ trigger with which the data used in this thesis was taken, requires zero charged multiplicity in the PWC's and the JDC. Around 4 % of the annihilation are pure neutral decays. The trigger is very selective due to the excellent detection efficiency of the charged tracking devices. The fast decision time of the level 1 trigger (around 6 μs) allows data taking rates up to 80 Hz. In total, 24.7×10^6 zero-prong triggered events have been collected at rest in liquid hydrogen.

2.7 Photon Reconstruction

Photons with a typical energy range of few to several hundred MeV deposit their total energy in the calorimeter mainly via electromagnetic showers. A shower spreads out over several crystals and photons interacting in proximity tend to have overlapping energy deposits. The task of the reconstruction is to associate crystals to clusters and to separate the clusters into single PEDs (Particle Energy Deposits)[2]. Figure 7 shows the energy deposits in the calorimeter of a 7γ event.

Crystals within the same cluster are required to have an energy entry exceeding 1.0 MeV and to share at least one edge or corner with another crystal of the same cluster. The total energy of the cluster has to be at least 20 MeV (the minimum cluster energy).

The cluster is then investigated for subclusters. The energy in the central crystal of a subcluster has to be greater than in each of the eight neighboring crystals and and for secondary subclusters, it has to exceed 20 MeV (the minimum central crystal energy) in addition. Each subcluster is assumed to correspond to a single PED. The energy of crystals belonging to several subclusters are split according to the energy contents of each subclusters central crystal.

In the case where only one subcluster is found, the total cluster energy is associated to one PED with the center of gravity giving the interaction point (ϕ, θ) inside of the cluster. If several PEDs contribute to a cluster, the PED position is determined by the center of gravity of the central crystal and the eight (split) neighbors. The energy of the PED (E_i) is proportional to the sum of the central crystal and the eight surrounding crystals (E_i^9) and to the total cluster energy (E_{clu}):

$$E_i = \frac{E_i^9}{\sum_{PEDS} E_i^9} \, E_{\mathrm{clu}} \tag{6}$$

The energy resolution for photons is $\sigma(E)/E \approx 2.5\% \, (E[\mathrm{GeV}])^{-1/4}$ and the angular resolution is typically 25 mrad, depending on the energy.

---

[2] Apart from photons, also charged particles and neutral kaons can interact with the calorimeter.

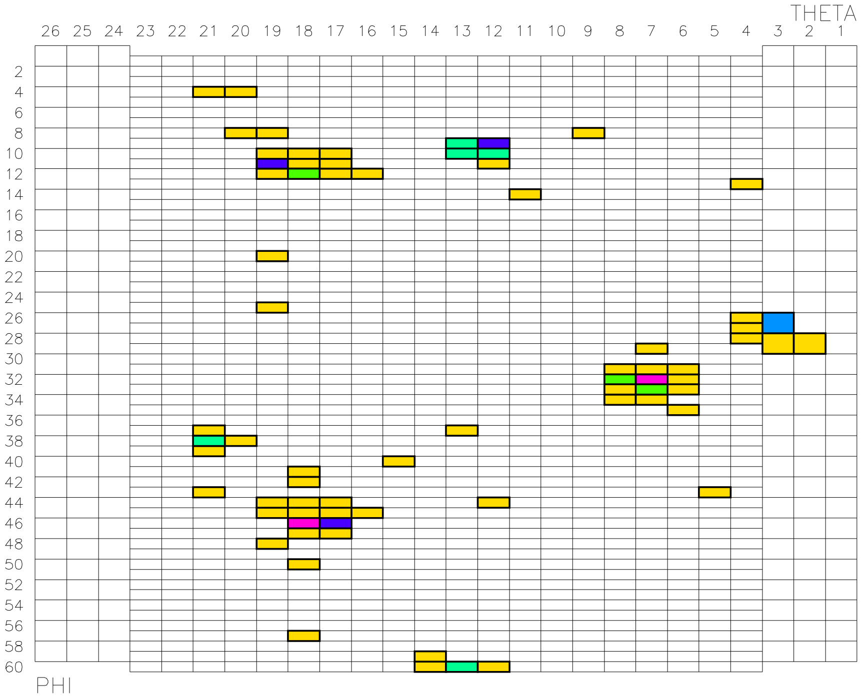

Figure 7: *Energy deposits of a 7γ raw event in the 1380 crystals of the CsI calorimeter. The energy of a γ spreads out over several crytals. The grey scale corresponds to the energy range of 1 to 500* MeV*. The single low energy entries are due to noisy crystals and are below the 20* MeV *threshold.*

3 The Reactions $\overline{p}p \to \omega\pi^0\pi^0$ and $\overline{p}p \to \omega\eta\pi^0$

In order to study resonances in $\bar{p}p$ annihilation at rest, one has to investigate annihilations into multi-body final states, where the intermediate resonances are produced recoiling against one or more final state particles. The strongest three-body channels including an ω are the reactions

$$\begin{aligned} \bar{p}p &\to \omega\pi^+\pi^- \quad (6.6 \pm 0.6\,\%) & (7)\\ \bar{p}p &\to \omega\pi^0\pi^0 \quad (2.7 \pm 0.4\,\%) & (8)\\ \bar{p}p &\to \omega\eta\pi^0 \quad (1.1 \pm 0.2\,\%) & (9) \end{aligned}$$

The branching ratio (7) is taken from [31], while (8),(9) are determined in this work (see section 7). Other combinations with ω and with two light mesons are suppressed by phase space or excluded by the available center of mass energy which is limited to $E_0 = 2m_p = 1876.6$ MeV/c^2.

The ω cannot be detected directly, but has to be reconstructed through its decay. The main decay modes of the ω are, according to PDG [8],

$$\begin{aligned} B(\omega \to \pi^+\pi^-\pi^0) &= (88.8 \pm 0.7)\,\% & (10)\\ B(\omega \to \pi^0\gamma) &= (8.5 \pm 0.5)\,\% & (11)\\ B(\omega \to \pi^+\pi^-) &= (2.21 \pm 0.09)\,\% & (12)\\ B(\omega \to \eta\gamma) &= (6.5 \pm 1.0) \times 10^{-4} & (13) \end{aligned}$$

The branching ratio (12) is small because of isospin violation. The decay (13) is, compared to (11), suppressed by $SU(3)$ symmetry and phase space. The latter was measured in Crystal Barrel [37] in agreement with the PDG value [8]. Despite the huge branching ratio, the yield of the event selection via the charged decay mode is relatively modest with the Crystal Barrel Experiment (see for example ref. [38]) owing to the lack of an efficient trigger on eg. $\omega(\to \pi^+\pi^-\pi^0)\pi^0\pi^0$. However, the excellent photon detection and the availability of high statistic "all-neutral" data samples predestinate the detector for an investigation with the ω reconstructed from its electromagnetic decay (reaction 11) and allow to study the $\omega\pi^0\pi^0$ and $\omega\eta\pi^0$ final states in the 7γ mode.

Due to C-parity conservation and neglecting D wave contributions, the annihilation of $\bar{p}p$ into the two channels occurs only from the atomic states

$$^3S_1\,(1^{--}) \quad \text{and} \quad {}^1P_1\,(1^{+-})\,. \qquad (14)$$

It also limits the quantum numbers J^{PC} of the accessible resonant systems (see table 4).

system	mass range		C	I	allowed J^{PC}
{recoil partner}	[MeV/c^2]	[MeV/c^2]	parity		{including non $q\bar{q}$ resonances}
$\omega\eta$	1329.2	1741.6	-1	0	$\{0^{+-}\}$, 1^{--}, 1^{+-}, $\{2^{+-}\}$, 3^{--}
$\omega\pi^0$ $\{\pi^0\}$	916.9	1741.6		1	
$\omega\pi^0$ $\{\eta\}$	916.9	1329.3		1	
$\pi^0\pi^0$	270.0	1094.7	$+1$	0	0^{++}, 2^{++}
$\eta\pi^0$	682.3	1094.7		1	0^{++}, $\{1^{-+}\}$, 2^{++}
$\bar{p}p$	1876.6		-1		1^{--}, 1^{+-} (atomic states)

Table 4: *The conservation law restrictions on* $\overline{p}p \to \omega\pi^0\pi^0$ *and* $\overline{p}p \to \omega\eta\pi^0$. *States with quantum numbers in parenthesis would be exotic (non* $q\bar{q}$*).*

Kinematically, the three-body final state is described by 3×3 variables from which 4 degrees of freedom from energy and momentum conservation and 3 Euler angles of the arbitrary orientation of the system can be subtracted, leaving 2 independent variables. It is convenient to characterize the three-body system in terms of the two-body invariant masses $s_{12} = m_{12}^2$ and $s_{23} = m_{23}^2$. Phase space events, plotted in coordinates of s_{12} and s_{23} (Dalitz plot), are then uniformly distributed.

The decay angles of the ω (θ,ϕ, defined with respect to the flight direction) depend on the spin alignment and carry additional information about the annihilation channel. Accordingly, the reaction including $\omega \to \pi^0\gamma$ has four degrees of freedom. The transition probability is then given by

$$d\Gamma_{if} \sim \frac{1}{E_0^3} |\mathcal{A}_{if}|^2 \, ds_{12} \, ds_{23} \, d\phi \, d\cos\theta \tag{15}$$

where $\mathcal{A}$ denotes the transition amplitude of the annihilation. A resonance appears as a deviation from the uniform distribution of the observables s_{12}, s_{23}, ϕ and $\cos\theta$. For instance, an intermediate state decaying into particle 1 and 2 is visible as a band in the Dalitz plot. The density distribution along the band corresponds to the angular distribution of the resonance decay. The polar decay angle θ_{12}^* in the center of mass system of particle 1 and 2 is a linear function of s_{23} [39]:

$$\cos\theta_{12}^* = \frac{2s_{23} - s_{23}^{\max}(s_{12}) - s_{23}^{\min}(s_{12})}{s_{23}^{\max}(s_{12}) - s_{23}^{\min}(s_{12})} \tag{16}$$

The absolute limits on the invariant mass combinations of the two three-body final states are given in table 4. It will be the aim of the partial wave analysis to investigate the composition of the transition amplitude (section 8).

4 Data Selection and Event Reconstruction

The aim of the data selection is to retrieve events of the type $\overline{p}p \to \omega\pi^0\pi^0$ and $\overline{p}p \to \omega\eta\pi^0$ from the “all-neutral” data of the Crystal Barrel Experiment and to reconstruct these events via the decays

$$\begin{array}{llll} \bar{p}p \longrightarrow & \omega & \eta & \pi^0 \;/\; \omega\pi^0\pi^0 \\ & & & \hookrightarrow \gamma\gamma \\ & & \hookrightarrow & \gamma\gamma \\ & \hookrightarrow & \pi^0 \;\; \gamma & \\ & & \hookrightarrow \gamma\gamma & \end{array} \tag{17}$$

In the first step of the data selection, a sample of 7γ events is extracted from the triggered “0-prong” data. The second step is based on kinematic fits, where the two final states are reconstructed, using the fit results, and selected by means of confidence level cuts. The data selection and reconstruction are performed using the standard Crystal Barrel software package whose main components and versions are listed in table 5 below.

4.1 7γ Preselection

The data selection starts from 19.2×10^6 triggered ”0-prong“ events collected between June 1990 and July 1994. The trigger required the PWC and the JDC was to veto charged tracks (see section 2.6).

In spite of this requirement, some residual tracks due to inefficiencies of the 0-prong trigger and gamma conversions remain. After rejecting these events, 17.3×10^6 events are kept.

The PEDs (Particle Energy Deposits) in the crystals are reconstructed with the requirement of an energy greater than 20 MeV in the cluster and also in the central crystal of secondary PEDs in the cluster (see section 2.7). The minimum energy of a crystal in the cluster is 1.0 MeV. Figure 8 shows the PED multiplicity distribution in the calorimeter of the analyzed all-neutral data. $1'827'578$ events have exactly seven PEDs. In order to improve the quality of the 7 PED sample, the following cuts are applied:

- No crystal type 13. We reject events with PEDs in crystals next to the beam entrance end exit (crystal *type 13*, see fig. 5) which are not completely surrounded by other crystals. This prevents insufficient cluster reconstruction due to energy leakage.

- Split-off suppression. In order to reduce the feedthrough of 6γ events, where one of the photons produces a PED together with a small split-off shower

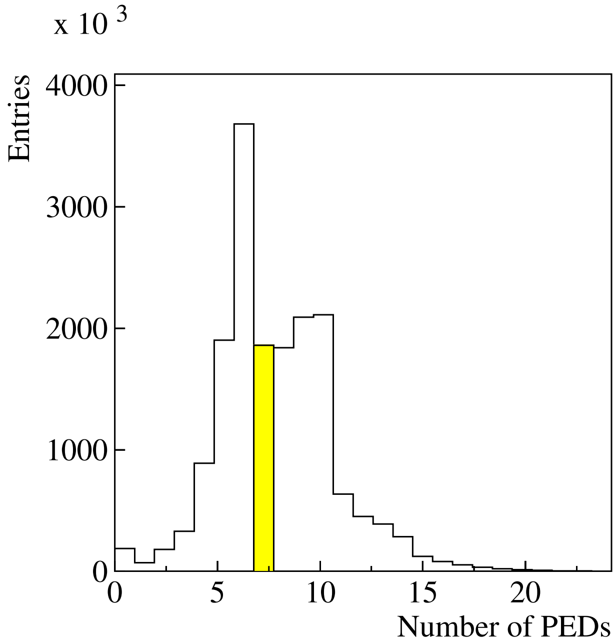

Figure 8: *Distribution of PED (particle energy deposit) multiplicity in the calorimeter. The grey area shows the 7 PED events.*

Name	Version	Task
BCTRAK	2.04/03	crystal reconstruction
GTRAK	1.37/01	global tracking
CBOFF	1.30/13	general offline
CBGEANT	5.04/04	Monte Carlo simulation based on GEANT 3.2130
DOLBY-C	1.5	split-off suppression
CCDBCB	2.05/01	calibration data base
CBKFIT	3.09/00	kinematic fitting package

Table 5: *The Crystal Barrel Reconstruction Software [40] used in the present analysis.*

which is wrongly reconstructed as a separate PED, split-off cuts are applied, using the Dolby-C software [40] with the default settings. Around 10 % of the events are rejected this way.

- Energy and momentum conservation. The measured total energy E_{tot} is required to lie in the range between 1700 and 2050 MeV and the absolute value of the total momentum p_{tot} between 0 and 200 MeV/c (see figure 9). Events not satisfying these conditions are events with missing photons, a non interacting K_L^0, an antiproton scattered into the barrel or are pile up events.

939'361 events (51%) survive these additional cuts, referred to in the following as 7γ events. Table 6 lists the steps of data reduction separately for each run period analyzed in this work. The data from December 89, the first data taken at the experiment, are discarded because their quality is significant lower compared to the succeeding run periods.

Fig. 10 shows the 2γ invariant mass spectra of the 7γ sample. The peaks at π^0 and η masses, fitted with a Gaussian on a second order polynomial background, correspond to $134.87 \pm 0.01\,\mathrm{MeV/c^2}$ and $549.17 \pm 0.28\,\mathrm{MeV/c^2}$, respectively, and are in good agreement with the PDG values [8]. The fitted widths ($\sigma = 7.46 \pm 0.01\,\mathrm{MeV/c^2}$, $14.44 \pm 0.31\,\mathrm{MeV/c^2}$) are dominated by the detector resolution, which is in the order of few percents depending on the energy of the photons (see section 2.7).

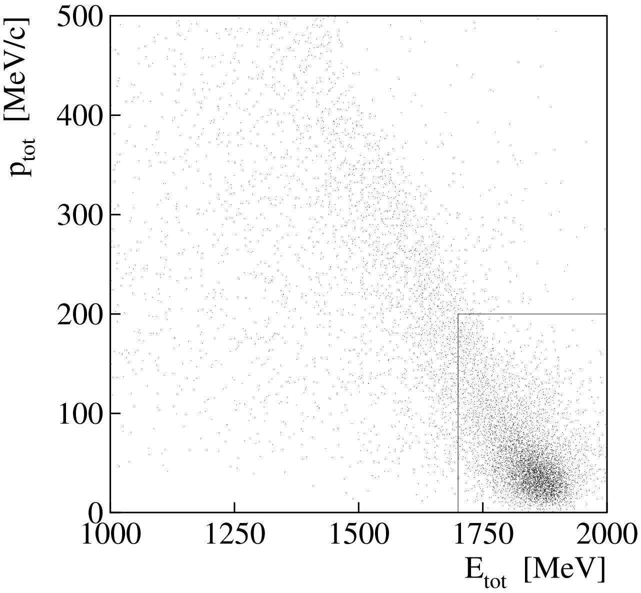

Figure 9: *Total energy and momentum distribution. The box shows the selected events.*

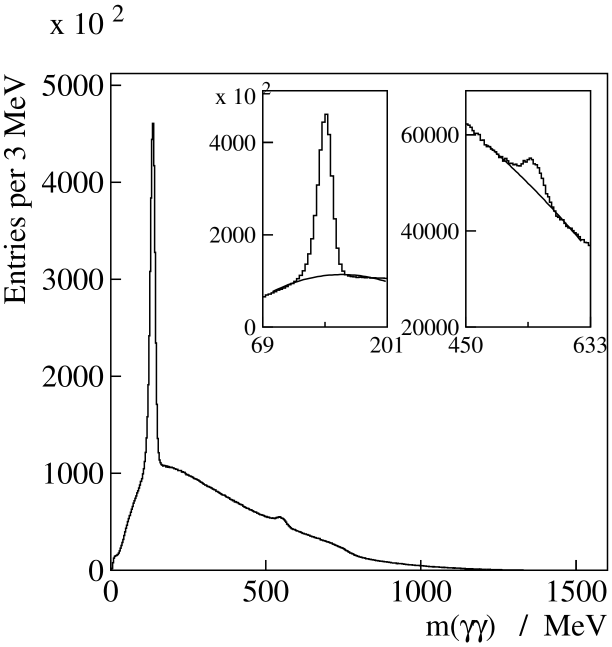

Figure 10: *Spectrum of* 2γ *invariant mass of* 7γ *events (21 combinatorial entries per event). The insets show the at* π^0 *and* η *mass peaks. The smooth curves correspond to the polynomial background.*

run period		all neutral trigger	no charged tracks	7 PEDs in the crystals
June	1990	1,251,520	1,119,419	127,049
July	1990	4,000,811	3,591,823	407,113
September	1990	1,495,090	1,329,428	144’994
November	1990	4,602,315	4,193,543	435’150
May	1991	1,564,095	1,359,218	139,346
June	1991	1,447,962	1,280,307	135,208
August	1991	1,651,384	1,466,726	155,577
October	1993	1,963,845	1,703,148	168,708
July	1994	1,222,229	1,074,641	114,433
sum		19,199,251	17,118,253	1,827,578

run period		no crystal type 13	split off suppression	energy and momentum
June	1990	96,871	86,569	58,366
July	1990	331,701	299,664	195,192
September	1990	111,811	101,495	68,750
November	1990	359,331	325,058	236,306
May	1991	115,709	104,623	78,485
June	1991	110,835	100,545	72,379
August	1991	125,518	113,701	79,731
October	1993	135,964	123,217	86,996
July	1994	95,825	85,930	63,156
sum		1,483,565	1,340,802	939,361

Table 6: *Data reduction of the 7γ preselection (see text).*

4.2 Reconstruction of $\omega\pi^0\pi^0$ and $\omega\eta\pi^0$ Events

Due to statistical fluctuation of the measured quantities, the total energy and momentum differ from the nominal values. The measurement can be improved by imposing these as constraints in a kinematic fit. Energy and momentum conservation define four constraints,

$$\vec{p}_{tot} - \sum_{i=1}^{n} \vec{p}_i = 0 \tag{18}$$

$$E_{tot} - \sum_{i=1}^{n} E_i = 0 \tag{19}$$

while the π^0 and ω mass requirements for the two and three γ combinations define the conditions

$$(E_i + E_j)^2 - (\vec{p}_i + \vec{p}_j)^2 - m_{\pi^0}^2 = 0 \tag{20}$$

$$(E_i + E_j + E_k)^2 - (\vec{p}_i + \vec{p}_j + \vec{p}_k)^2 - m_{\omega}^2 = 0 \tag{21}$$

The kinematic fit gives as a result the optimal correction of the n measured values $\tilde{x}_i = x_i + \delta x_i$ which fulfill all m conditions $f_j(\tilde{\mathbf{x}}) = 0$. This is done by performing a constrained (mC) χ^2 fit of the measured photon momenta, using Lagrangian multipliers. The fitted parameters $\tilde{\mathbf{x}}$ have smaller errors $\tilde{\sigma}_i$ than the experimental uncertainties σ_i, and the distribution of the pulls defined by

$$\Delta x_i = \frac{\delta x_i}{\sqrt{\sigma_i^2 - \tilde{\sigma}_i^2}} \tag{22}$$

is expected to be a Gaussian centered on zero with a standard deviation of 1.

The reliability of the fit is estimated by the confidence level (CL) of the χ^2 value referred to $(n - m)$ degrees of freedom. The confidence level distribution of an ideal data sample is expected to be uniform. It rises towards higher CL if the measured errors are too large, and drops if the errors are too small. Feedthrough events, having bad CL, accumulate mainly in the low and very low CL region.

The kinematic fit is used to find the accurate 7γ combination for the reconstruction, to improve the measurements and to reduce the background feedthrough. Following hypothesis are therefore fitted:

$$\pi^0\pi^0\pi^0\gamma \quad (6\mathrm{C}) \tag{23}$$

$$\eta\pi^0\pi^0\gamma \quad (6\mathrm{C}) \tag{24}$$

$$\omega\pi^0\pi^0 \quad (7\mathrm{C}) \tag{25}$$

$$\omega\eta\pi^0 \quad (7\mathrm{C}) \tag{26}$$

The events are selected by demanding the cuts and anticuts on the confidence level of the best 7γ combinations for each hypothesis. Accordingly, the selected $\omega\pi^0\pi^0$ events have to fulfill the conditions

$$\begin{aligned} CL(\pi^0\pi^0\pi^0\gamma) &> 5\% && (27)\\ CL(\pi^0\pi^0\pi^0\gamma) &> 10\,CL(\eta\pi^0\pi^0\gamma) && (28)\\ CL(\omega\pi^0\pi^0) &> 5\% && (29)\\ CL(\omega\pi^0\pi^0) &> 10\,CL(\omega\eta\pi^0) && (30) \end{aligned}$$

and the $\omega\eta\pi^0$ events

$$\begin{aligned} CL(\eta\pi^0\pi^0\gamma) &> 5\% && (31)\\ CL(\eta\pi^0\pi^0\gamma) &> 10\,CL(\pi^0\pi^0\pi^0\gamma) && (32)\\ CL(\omega\eta\pi^0) &> 5\% && (33)\\ CL(\omega\eta\pi^0) &> 10\,CL(\omega\pi^0\pi^0) && (34) \end{aligned}$$

The anticuts prevent feedthrough from the competing channel. The cuts and anticuts are optimized by means of Monte Carlo simulations. The data reduction listed in table 7 and 8 leads to the following number of events

$$\begin{aligned} N(\omega\pi^0\pi^0) &= 136'023 && (35)\\ N(\omega\eta\pi^0) &= 34'064 && (36) \end{aligned}$$

The pulls (eq. (22)) of the fitted photons of the selected $\omega\pi^0\pi^0$ events are shown in figure 11. Since the confidence level cuts reduce the widths of the pulls, a scan is performed and extrapolated to zero confidence level. The mean and the extrapolated width are given in table 9. They agree well with the Monte Carlo simulation. Pulls for slightly different errors are listed in the third row and lead to similar results. The Monte Carlo study shows that variation of the experimental errors within 5% hardly affect the selection efficiency. The CL distribution of both selections are show in figure 12 and 13. The inset in figure 12 illustrates the simulated $4\pi^0$ feedthrough background. Due to the presence of background it is difficult to tune the errors according to the CL distribution. Nevertheless, a fairly good agreement between Monte Carlo simulation and measurement is found at higher CL. One has also to consider that the errors are slightly underestimated due to the fact that the ω mass is fitted to the nominal value neglecting its decay width (8.41 MeV/c). However, the corresponding standard deviation $\sigma = \Gamma/\sqrt{8\ln 2} = 3.6$ MeV is small compared with the detector resolution (13 MeV, 11 MeV, see sec. 4.3, eq. (38), (40)).

The efficiency of the anticuts (28), (30) and (32), (34), respectively, is illustrated in figures 14 and 15. In contrast to the background events, the ω peak of the $\pi^0\gamma$ invariant mass spectrum is hardly affected by these cuts for the $\omega\eta\pi^0$ selection and only slightly reduced for the $\omega\pi^0\pi^0$ sample.

run period		CL($\pi^0\pi^0\pi^0\gamma$)		CL($\omega\pi^0\pi^0$)	
		> 0.05	$> 10\times$ CL($\eta\pi^0\pi^0\gamma$)	> 0.05	$> 10\times$ CL($\omega\eta\pi^0$)
June	1990	24,153	13,081	8,134	8,107
July	1990	77,613	42,075	26,952	26,855
September	1990	28,694	15,452	9,827	9,793
November	1990	103,068	55,620	35,708	35,589
May	1991	34,319	18,626	11,740	11,704
June	1991	38,760	18,082	11,837	11,776
August	1991	30,603	16,481	10,284	10,251
October	1993	37,451	20,281	13,010	12,961
July	1994	26,373	14,352	9,017	8,987
sum		401,034	214,050	136,509	136,023

Table 7: *Data reduction by kinematic fitting cuts (27-30) for* $\omega\pi^0\pi^0$.

run period		CL($\eta\pi^0\pi^0\gamma$)		CL($\omega\eta\pi^0$)	
		> 0.05	$> 10\times$ CL($\pi^0\pi^0\pi^0\gamma$)	> 0.05	$> 10\times$ CL($\omega\pi^0\pi^0$)
June	1990	14,237	3,829	2,041	2,033
July	1990	45,619	11,735	6,598	6,576
September	1990	17,106	4,366	2,458	2,448
November	1990	61,115	15,544	8,818	8,783
May	1991	20,063	5,060	2,823	2,807
June	1991	26,069	5,799	3,437	3,422
August	1991	18,102	4,732	2,601	2,586
October	1993	22,132	5,696	3,201	3,186
July	1994	15,496	4,067	2,230	2,223
sum		239,939	60,728	34,207	34064

Table 8: *Data reduction by kinematic fitting cuts (31-34) for* $\omega\eta\pi^0$.

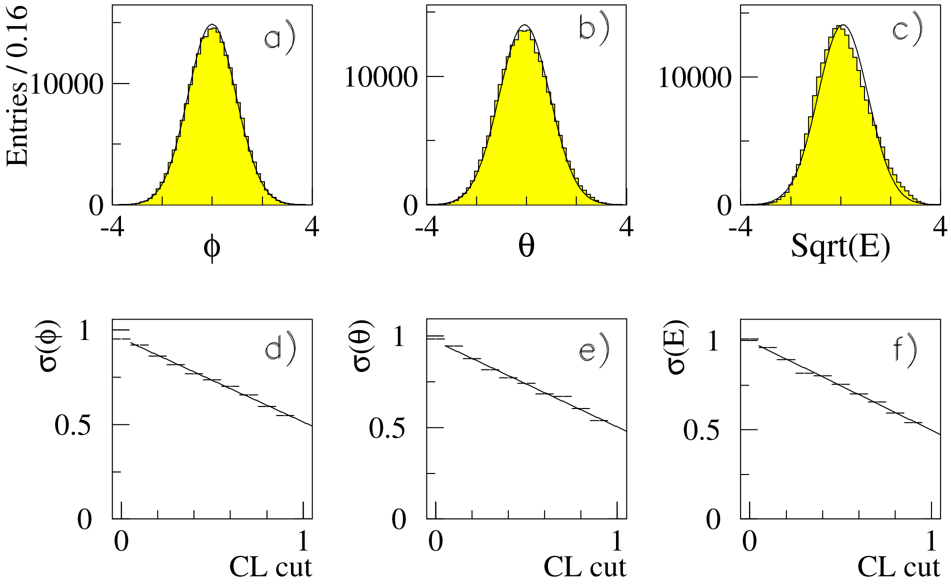

Figure 11: *Pulls of ϕ, θ and $\sqrt{E}$ of fitted photons (a-c). The linear dependence of the pull width (σ) and the cut on CL($\omega\pi^0\pi^0$) is shown in (d-f).*

		$\sigma_{\Delta\phi}$	$\sigma_{\Delta\theta}$	$\sigma_{\Delta\sqrt{E}}$	ϵ
$\omega\pi^0\pi^0$		0.955(1)	0.972(1)	0.997(1)	-
$\omega\pi^0\pi^0$	MC	0.953(1)	0.975(1)	0.985(1)	12.37(3)%
$\omega\pi^0\pi^0$	MC[a]	0.951(1)	0.983(1)	1.003(1)	12.21(6)%
$\omega\eta\pi^0$		0.950(1)	0.972(1)	0.984(1)	-
$\omega\eta\pi^0$	MC	0.937(1)	0.961(1)	0.966(1)	20.59(4)%
$\omega\eta\pi^0$	MC[b]	0.945(1)	0.963(1)	0.981(1)	20.00(8)%

Table 9: *The pull width of measured and simulated data extrapolated for zero CL cut (see fig. 11). The second row shows the width of Monte Carlo data. The third row shows the pull width including an error scaling, (a) of 0.95 in $\sqrt{E}$ for $\omega\pi^0\pi^0$ and (b) of 0.97 in ϕ and $\sqrt{E}$ for $\omega\eta\pi^0$. The errors in brackets are statistical. ϵ is the selection efficiency (see sec. 5.1)*

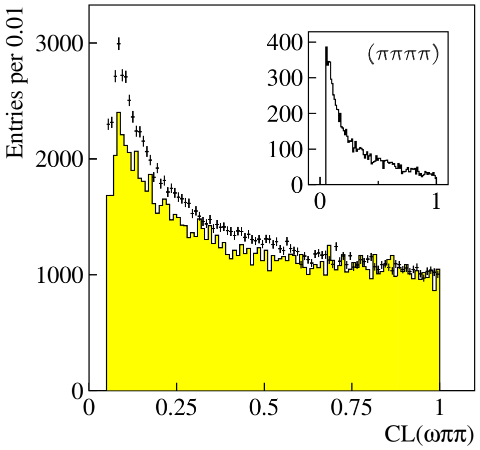

Figure 12: *Confidence level distribution of the kinematic fit to* $\omega\pi^0\pi^0$ *of the selected events (observed data with error bars, the Monte Carlo data shaded). The inset plot shows the confidence level distribution for the simulated* $4\pi^0$ *feedthrough events (see sec. 5).*

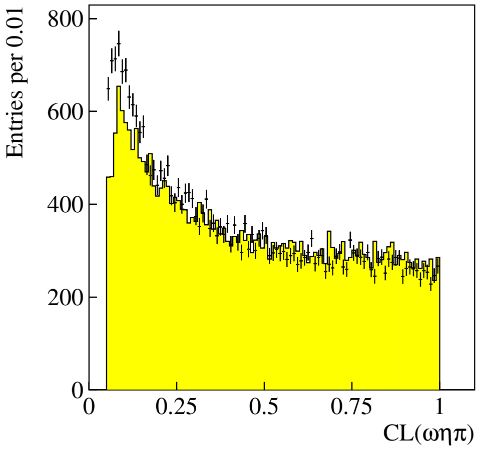

Figure 13: *Confidence level distribution of the kinematic fit to* $\omega\eta\pi^0$ *of the selected events (observed data with error bars, the Monte Carlo data shaded).*

4.3 The ω Mass Fit

The ω peak is investigated in the $\pi^0\gamma$ mass spectra of the kinematically fitted $\pi^0\pi^0\pi^0\gamma$ and $\eta\pi^0\pi^0\gamma$ events. In order not to bias the data with respect to the ω mass, we demand only the confidence level cuts $\mathrm{CL}(\pi^0\pi^0\pi^0\gamma) > 5\%$ and $\mathrm{CL}(\eta\pi^0\pi^0\gamma) > 5\%$, respectively, which lead to data samples containing 401'034 and 239'939 events.

The dynamics of the ω decay are described by the Breit-Wigner function (see section 8, eq. 55). The mass dependent transition probability is then proportional to the square of the Breit-Wigner function times the phase space factor $\rho(m) = 2q/m$, where q denotes the breakup momentum given in eq. (54). To reproduce the line shape in the invariant mass spectrum, one has to take into account the detector response and the background, mainly stemming from combinatorics. The dynamical function is therefore folded with a resolution function, approximated by a Gaussian. The resulting function is known as Voigtian. The background is expected to be smooth over the mass region of the ω peak and is therefore described by a quadratic polynomial.

The width of the ω peak depends on the decay width Γ and the standard deviation of the Gaussian σ which are both a priori not known. Fitting simultaneously the two parameters does not lead to stable results since their correlation is too strong. Therefore we chose to fix Γ to the PDG value $\Gamma = 8.41 \pm 0.09$ MeV [8], leaving six parameter to be fitted (three parameters for the polynomial, the mass, the resolution and the number of events integrated over the Voigtian).

The mass spectra are fitted in bins of 1.5 MeV and over the range from 680 MeV to 880 MeV, using PAW [41] and MINUIT [42], while the convolution of the Voigtian is done numerically. The resulting mass and resolution for the $\pi^0\pi^0\pi^0\gamma$ sample is

$$m_\omega = (781.86 \pm 0.05_{\mathrm{stat}} \pm 0.1_{\mathrm{sys}})\ \mathrm{MeV}/c^2 \tag{37}$$

$$\sigma_\omega = (12.8 \pm 0.05_{\mathrm{stat}} \pm 0.5_{\mathrm{sys}})\ \mathrm{MeV}/c^2 \tag{38}$$

and for the $\eta\pi^0\pi^0\gamma$ sample

$$m_\omega = (782.58 \pm 0.11_{\mathrm{stat}} \pm 0.2_{\mathrm{sys}})\ \mathrm{MeV}/c^2 \tag{39}$$

$$\sigma_\omega = (11.3 \pm 0.13_{\mathrm{stat}} \pm 0.5_{\mathrm{sys}})\ \mathrm{MeV}/c^2 \tag{40}$$

containing 257'480 and 37'760 events respectively in the Voigtian. The fitted mass spectra are shown in figure 14 and 15. The first value agrees very well with the PDG mass 781.94±0.12 MeV [8]. The second number is somewhat higher, five standard deviations for the statistical error and three for the systematic error, as obtained by comparing the fit results for different CL and ω momentum cuts. The same mass fits performed on Monte Carlo data depend less on the CL cuts and agree within the systematics with the nominal PDG value, used also in the simulation.

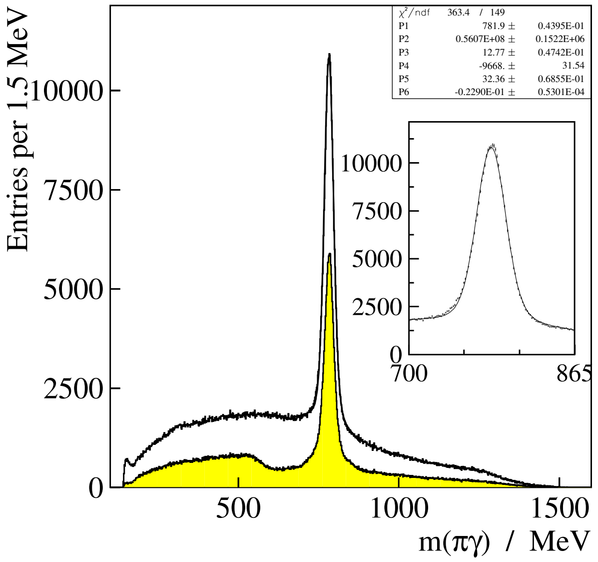

Figure 14: *$\pi^0\gamma$ mass spectrum for $\pi^0\pi^0\pi^0\gamma$ events (3 entries per event) which are selected by demanding only the CL cut (27). The inset shows the ω mass region together with the fit (solid line). The shaded curve corresponds to the spectrum after applying all CL cuts used for the $\omega\pi^0\pi^0$ selection.*

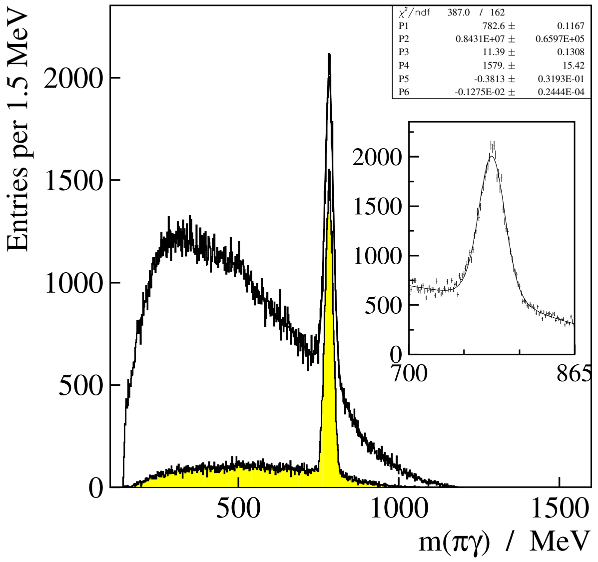

Figure 15: *$\pi^0\gamma$ mass spectrum for $\eta\pi^0\pi^0\gamma$ events (2 entries per event) which are selected by demanding only the CL cut (31). The inset shows the ω mass region together with the fit (solid line). The shaded curve corresponds to the spectrum after applying all CL cuts used for the $\omega\eta\pi^0$ selection.*

Thus the deviation of the second measurement may be explained by the presence of background, which is coming from $\omega\pi^0\pi^0$ events. The Monte Carlo simulation shows that the feedthrough somewhat deforms the shape of the background in the ω mass region. Also, a slight difference in the reconstruction of real and simulated $\eta\pi^0\pi^0\gamma$ events might be not excluded. However, the mass resolutions σ found by the fit agree well with the results from the Monte Carlo studies, presented in section 5. In a further investigation, it would be interesting to study also the influence of ω production in the annihilation. For instance, the damping of low momenta in the decay of the $\bar{p}p$ system described in section 8 may affect the line shape of the ω.

4.4 Dalitz Plots of $\omega\pi^0\pi^0$ and $\omega\eta\pi^0$

The Dalitz plots of $\bar{p}p \to \omega\pi^0\pi^0$ shown in figure 16 and 18 and the mass projection plotted in figure 19 display clear signs of resonances. The two bands of $b_1(1230)$ cross at the lower border of the Dalitz plot enclosing a region with low intensity. The associated peak in the $\omega\pi$ mass projection is clearly visible. In addition, a narrow dip appears on the diagonal, in the $\pi^0\pi^0$ mass spectrum around 1000 MeV, in the $f_0(980)$ region and a broad band below. The enhancement above the $f_0(980)$ is very pronounced and is an indication for the presence of a further resonance above or at the border of phase space.

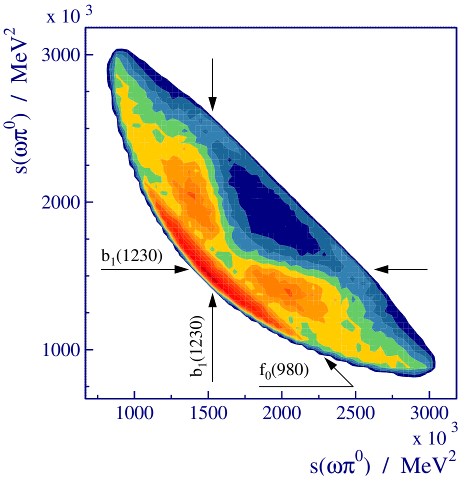

Figure 16: *Dalitz plot for* $\bar{p}p \to \omega\pi^0\pi^0$.

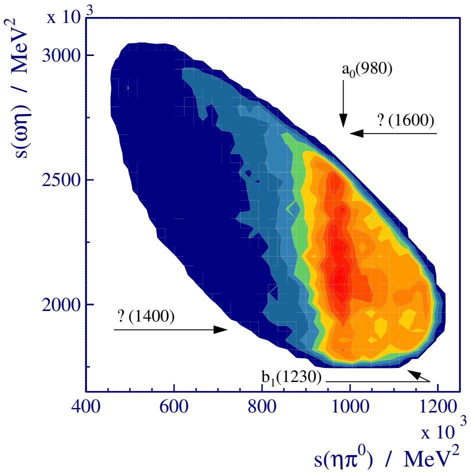

Figure 17: *Dalitz plot for* $\bar{p}p \to \omega\eta\pi^0$. *The evidence for two states at 1400 and 1600* MeV *is discussed below.*

The Dalitz plot of $\bar{p}p \to \omega\eta\pi^0$ is strongly dominated by $a_0(980)$, visible as a vertical band, respectively, as a diagonal band (see figure 17 and 20). Its narrow peak dominates the $\eta\pi^0$ projection (fig. 21a). However, the intensity distribution along the band indicates further resonances. The $b_1(1230)$ is not visible, neither in the Dalitz plot nor in the $\omega\pi^0$ spectrum (fig. 21b) which mainly represents the reflexion of the a_0. In contrast, the $\omega\eta$ mass spectrum (fig. 21c) shows an interesting feature in the low mass region (around 1400 MeV) and also a slight enhancement around 1600 MeV.

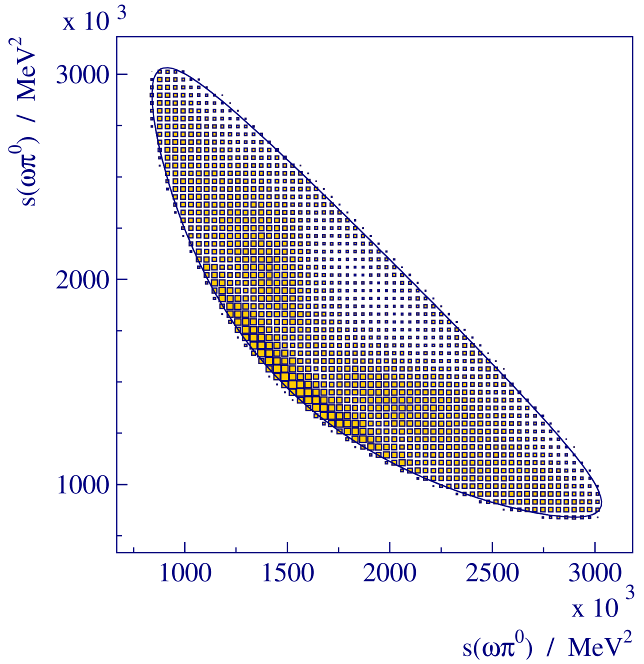

Figure 18: *Symmetrized Dalitz plot of $\omega\pi^0\pi^0$ (2 × 136023 events).*

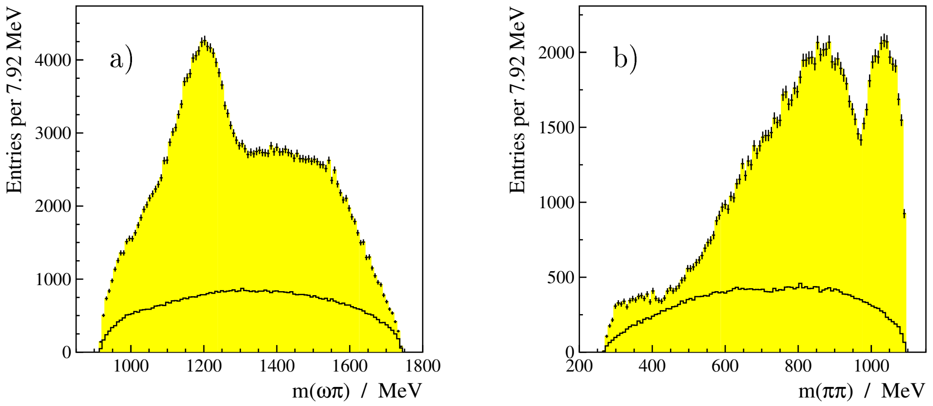

Figure 19: *(a) $\omega\pi^0$ (2 entries per event) and (b) $\pi^0\pi^0$ mass distributions in $\overline{p}p \to \omega\pi^0\pi^0$. The solid line corresponds to the acceptance of phase space distributed events determined by the Monte Carlo method.*

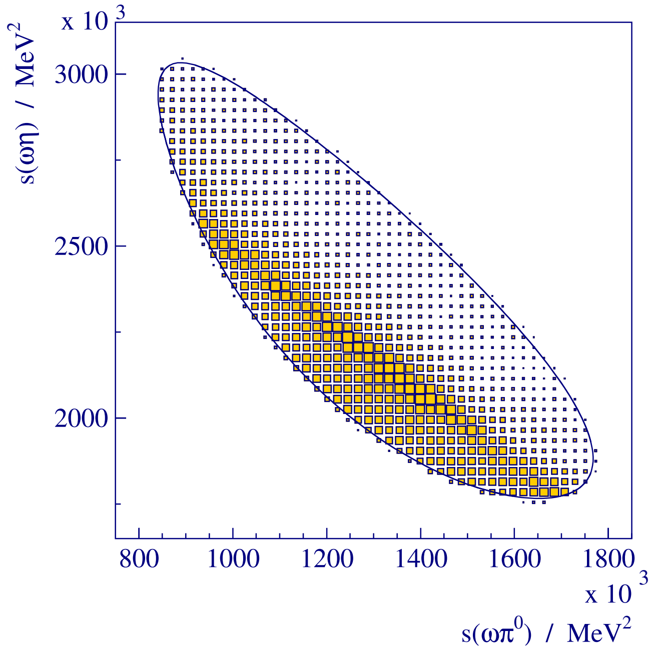

Figure 20: *Dalitz plot of $\overline{p}p \to \omega\eta\pi^0$ (34'064 events).*

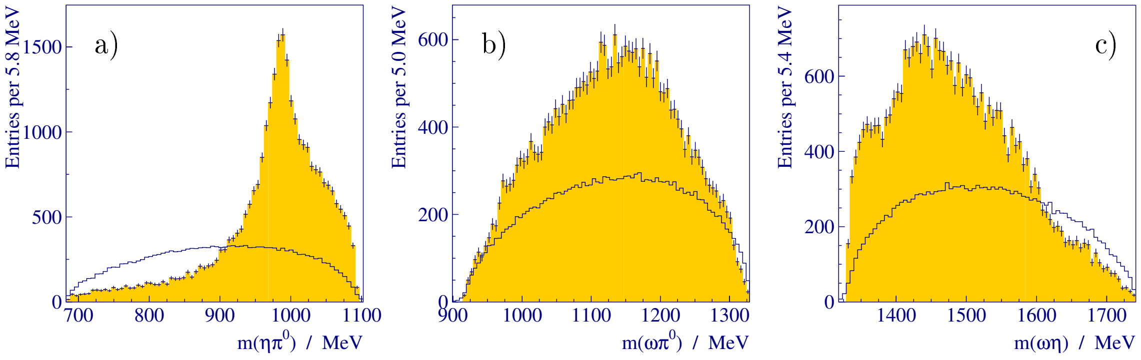

Figure 21: *(a) $\eta\pi^0$, (b) $\omega\pi^0$ and (c) $\omega\eta$ mass distributions of $\overline{p}p \to \omega\eta\pi^0$. The solid line corresponds to the acceptance of phase space distributed events determined by the Monte Carlo method.*

4.5 Angular Distributions of the ω Decay

The decay angles (θ,ϕ) of $\omega \rightarrow \pi^0\gamma$ are calculated in the center of mass system of the ω. $\cos\theta$ refers to the angle between the flight direction in the lab system and the direction of the γ. The azimuthal angle ϕ is the angle between the three-body plane of the annihilation and the ω decay plane.

The $\cos\theta$ distribution in $\omega\pi^0\pi^0$ (fig. 22a) shows a significant dependence on $\cos\theta$ which indicates that the ω is polarized along the flight direction. The degree of polarization varies depending on the Dalitz plot region (see fig. 24) and carries additional information on the composition of the signal which is also exploited in the partial analysis (see sec. 8). In contrast, the polar angle distributions in $\omega\eta\pi^0$ are much less pronounced (fig. 23a and 25) while in both data samples the coplanar decays ($\phi = -\pi, 0, \pi$) are enhanced (fig. 22b, 23b).

The peaks appearing in the $\cos\theta$ histograms 8,9,12 of figure 24 and 6,9 of figure 25 are owing to the combinatorial background which is discussed in section 5.4.

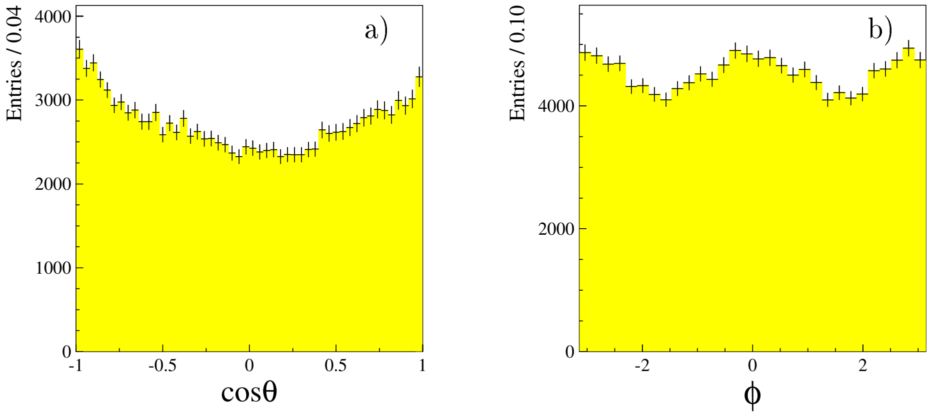

Figure 22: *Angular distribution of* $\omega \to \pi^0\gamma$ *for* $\omega\pi^0\pi^0$*; (a) the* $\cos\theta$ *distribution and (b) the* ϕ *distribution. The data is already corrected for the detector acceptance (see sec. 5.2).*

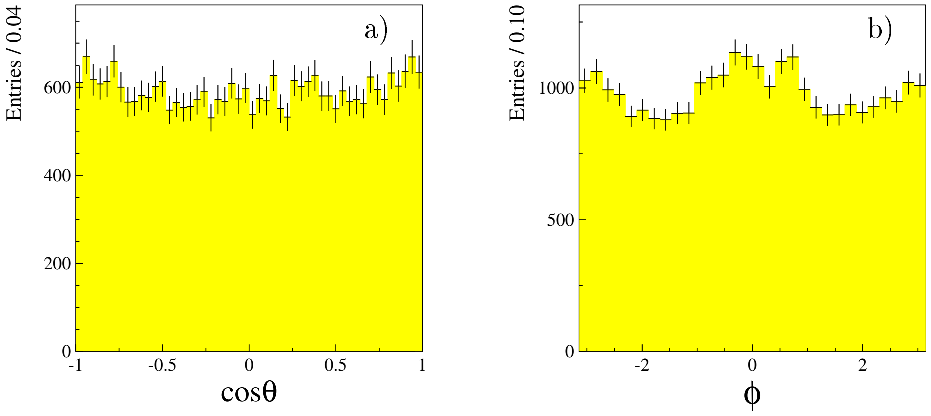

Figure 23: *Angular distribution of* $\omega \to \pi^0\gamma$ *for* $\omega\eta\pi^0$*; (a) the* $\cos\theta$ *distribution and (b) the* ϕ *distribution. The data is already corrected for the detector acceptance (see sec. 5.2).*

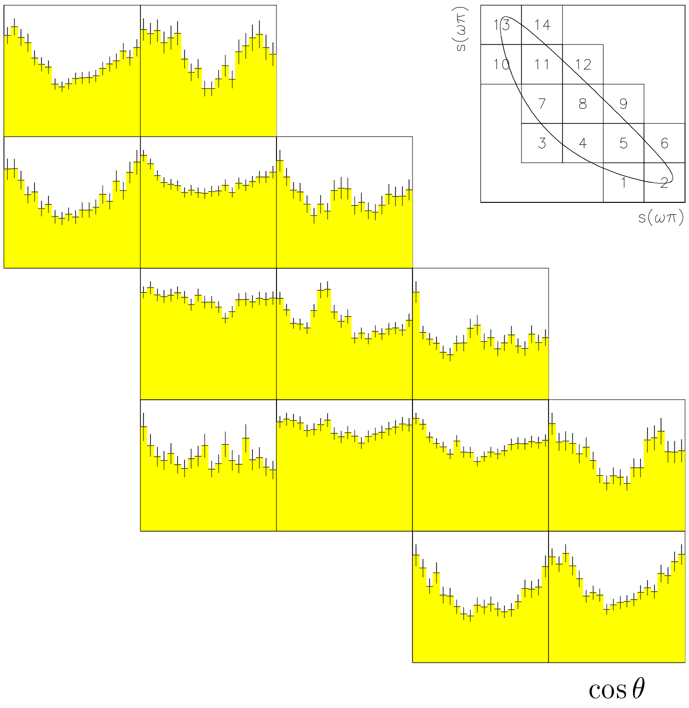

Figure 24: *Selected* $\cos\theta$ *distributions of* $\omega\to\pi^0\gamma$ *in* $\omega\pi^0\pi^0$*. The histograms, showing the* $\cos\theta$ *distribution in the range from -1 to 1, are grouped according to the Dalitz plot region they refer to (see inset). The boundaries of the regions are given by* $m_{\omega\pi^0} = 804, 1074, 1288, 1472, 1632, 1783\,\mathrm{MeV}$*. The data is corrected for the detector acceptance (see sec. 5.2). (The numbers of entries in the histograms are* $n_1 = 5'630$*,* $n_2 = 7'482$*,* $n_3 = 4'585$*,* $n_4 = 22'161$*,* $n_5 = 18'981$*,* $n_6 = 3'498$*,* $n_7 = 22'410$*,* $n_8 = 9'144$*,* $n_9 = 3'147$*,* $n_{10} = 5'536$*,* $n_{11} = 18'986$*,* $n_{12} = 3'203$*,* $n_{13} = 7'410$ *and* $n_{14} = 3'420$*.)*

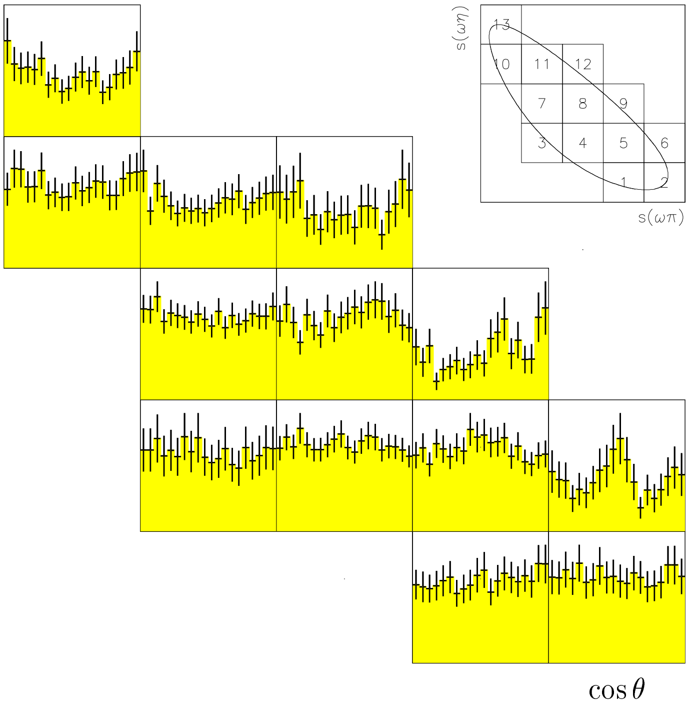

Figure 25: *Selected* $\cos\theta$ *distributions of* $\omega \to \pi^0\gamma$ *in* $\omega\eta\pi^0$*. The histograms, showing the* $\cos\theta$ *distribution in the range from -1 to 1, are grouped according to the Dalitz plot region they refer to (see inset). The boundaries of the regions are given by* $m_{\omega\pi^0} = 927, 1020, 1185, 1100, 1259, 1329\,\mathrm{MeV}$ *and* $m_{\omega\eta} = 1305, 1403, 1495, 1581, 1663, 1742\,\mathrm{MeV}$*. The data is corrected for the detector acceptance (see sec. 5.2). (The numbers of entries in the histograms are* $n_1 = 3'080$*,* $n_2 = 2'190$*,* $n_3 = 1'691$*,* $n_4 = 6'080$*,* $n_5 = 2'819$*,* $n_6 = 336$*,* $n_7 = 4'639$*,* $n_8 = 1'732$*,* $n_9 = 377$*,* $n_{10} = 2'226$*,* $n_{11} = 955$*,* $n_{12} = 329$ *and* $n_{13} = 898$*.)*

5 Monte Carlo Studies

The detection properties are studied with the Crystal Barrel Monte Carlo simulation program based on GEANT [40]. Events of a specific annihilation channel are generated and tracked through the detector including the interaction with the apparatus and the particle decays. The signal of each detector element is simulated and written out in a data format identical to that of real data. Thus real and simulated events can be reconstructed and analyzed with the same software.

5.1 Selection Efficiency

From 1.5×10^6 $\omega\pi^0\pi^0(\rightarrow 7\gamma)$ and 1.278×10^6 $\omega\eta\pi^0(\rightarrow 7\gamma)$ phase space generated Monte Carlo events, the data selection retrieves 185'612 and 263'078 events, leading to the efficiencies

$$\epsilon(\omega\pi^0\pi^0) = (12.37 \pm 0.03_{\text{stat}} \pm 0.20_{\text{sys}})\,\% \tag{41}$$

$$\epsilon(\omega\eta\pi^0) = (20.59 \pm 0.04_{\text{stat}} \pm 0.40_{\text{sys}})\,\% \tag{42}$$

The first error is statistical, the second uncertainty is systematic and determined by varying the errors of the kinematic fit (see sec. 4.2). The difference in efficiency is due to the fact that the anticut on $\pi^0\pi^0\pi^0\gamma$ in the $\eta\pi^0\pi^0\gamma$ selection is less selective than vice versa.

In addition, the following channels are generated and investigated for their feedthrough and detection probability: $4\pi^0(8\gamma)$, $\eta\pi^0(8\gamma)$, $2\pi^0\eta(8\gamma)$, $\pi^0\pi^0\pi^0(6\gamma)$, $\pi^0\pi^0\eta(6\gamma)$, $\pi^0\eta\eta(6\gamma)$ and $\omega\eta(9\gamma)$. The data reduction of the individual channels are listed in table 10 and 11. The strongest feedthrough stems from 8γ events, where one of the low energy photons is missing, whereas the contribution from 6γ events producing an additional split-off PED is efficiently suppressed.

5.2 Detector Acceptance

The detector acceptance is visible in the distribution of the reconstructed Monte Carlo events. Figures 26 and 27 shows the Dalitz plots of the $\omega\pi^0\pi^0$ and $\omega\eta\pi^0$ Monte Carlo events which are flat (the intensitiy fluctuations are of the order of 10-20%).

The angular distributions (fig. 28 and 29) are more sensitive to the detector response. For instance, the $\cos\theta$ distributions of the ω decay for $\omega\pi^0\pi^0$ (fig. 28a) is enhanced for backward emitted γ's. As a further test of the Monte Carlo, the acceptance corrected decay angles of π^0 and η are checked. They are flat, as expected for spin zero particles, and illustrate the reliability of the Monte Carlo with regard to the decay angles of the final state particles.

Monte Carlo		$\omega\pi^0\pi^0$ selection cuts					
	gen.	7 PED	$\pi^0\pi^0\pi^0\gamma$	cl_1 >10 cl	$\omega\pi^0\pi^0$	cl_2 >10 cl	detect.
channel	events	pre-sel.	$\mathrm{cl}_1 > 5\%$	$(\eta\pi^0\pi^0\gamma)$	$\mathrm{cl}_2 > 5\%$	$(\omega\eta\pi^0)$	probab.
$\omega\pi^0\pi^0$	1'500 k	589'488	398'825	210'141	186'137	185'612	12.37 %
$4\pi^0$	1'176 k	199'950	82'020	45'088	9'052	9'008	0.77 %
$\eta\pi^0(\eta\to 3\pi^0)$	300 k	70'270	23'896	16'697	1'975	1'955	0.65 %
$\omega\eta\pi^0$	300 k	121'103	6'054	184	51	45	$1.5\cdot10^{-4}$
$\pi^0\pi^0\pi^0\eta$	300 k	46'705	1'662	312	63	63	$2.1\cdot10^{-4}$
$\pi^0\pi^0\pi^0$	100 k	1'832	645	529	20	20	$2.0\cdot10^{-4}$
$\pi^0\pi^0\eta$	100 k	2'554	147	24	3	2	$0.2\cdot10^{-4}$

Table 10: *Monte Carlo study of detection probability for $\omega\pi^0\pi^0$. The Monte Carlo events are generated phase space distributed, including the decays $\pi^0\to\gamma\gamma$, $\eta\to\gamma\gamma$ and $\omega\to\pi^0\gamma$. The generated samples are reduced through the five selection steps of $\omega\pi^0\pi^0$. The last column contains the probability to identify an event as $\omega\pi^0\pi^0$.*

Monte Carlo		$\omega\eta\pi^0$ selection cuts					
	gen.	7 PED	$\eta\pi^0\pi^0\gamma$	cl_1 >10 cl	$\omega\eta\pi^0$	cl_2 >10 cl	detect.
channel	events	pre-sel.	$\mathrm{cl}_1 > 5\%$	$(\pi^0\pi^0\pi^0\gamma)$	$\mathrm{cl}_2 > 5\%$	$(\omega\pi^0\pi^0)$	probab.
$\omega\eta\pi^0$	1'278 k	515'750	337'395	310'793	263'482	263'078	20.59 %
$\pi^0\pi^0\pi^0\eta$	200 k	31'311	10'505	9'522	1'303	1'301	0.651 %
$\omega\pi^0\pi^0$	300 k	117'800	38'214	1'097	100	84	$2.8\cdot10^{-4}$
$4\pi^0$	300 k	50'662	9'378	599	45	44	$1.5\cdot10^{-4}$
$\pi^0\pi^0\pi^0$	100 k	1'832	138	29	1	1	$<0.3\cdot10^{-4}$
$\pi^0\pi^0\eta$	100 k	2'554	663	521	16	16	$1.6\cdot10^{-4}$
$\pi^0\eta\eta$	100 k	2'928	234	220	16	16	$1.6\cdot10^{-4}$
$\omega\eta(\eta\to 3\pi^0)$	100 k	4,863	266	201	17	16	$1.6\cdot10^{-4}$

Table 11: *Monte Carlo study of detection probability for $\omega\eta\pi^0$. See caption of table 10.*

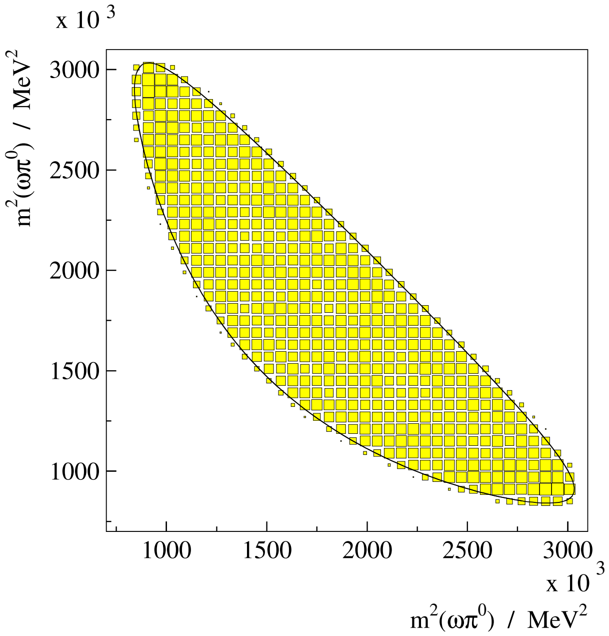

Figure 26: *Acceptance Dalitz plot for $\omega\pi^0\pi^0$ phase space events determined by Monte Carlo simulation.*

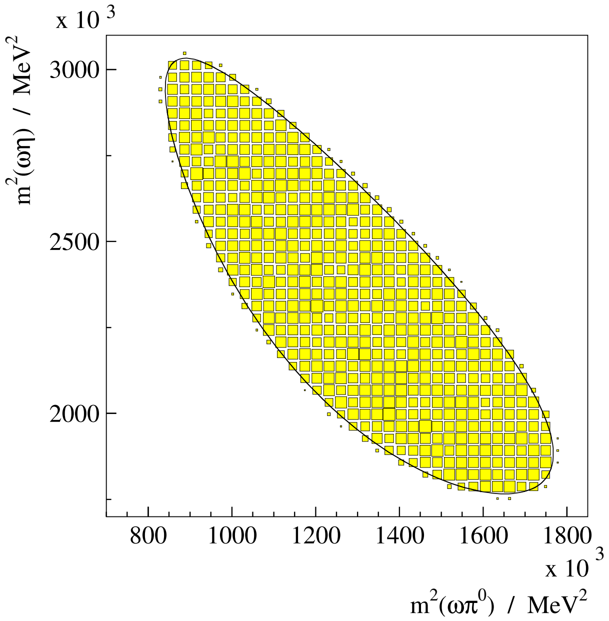

Figure 27: *Acceptance Dalitz plot for $\omega\eta\pi^0$ phase space events determined by Monte Carlo simulation.*

5.3 Detector Resolution

The detector resolution is studied by comparing generated events with reconstructed events on an event-by-event basis. Table 12 lists the standard deviations of the invariant masses and of the ω decay angles. The simulated resolution of $m(\pi^0\gamma)$ agrees well with the measurement described in section 4.3, eq. (38) and (40).

measured quantities		σ(MC)	
		$\omega\pi^0\pi^0$	$\omega\eta\pi^0$
$m(\pi^0\gamma)$	[MeV/c^2]	11.9(2)	9.6(2)
$m(\omega\pi^0)$	[MeV/c^2]	8.9(1)	6.3(2)
$m(\pi^0\pi^0)$	[MeV/c^2]	8.3(1)	-
$m(\eta\pi^0)$	[MeV/c^2]	-	6.6(2)
$m(\omega\eta)$	[MeV/c^2]	-	7.0(2)
$s(\omega\pi^0)$	[MeV^2]	23'450	19'650
$s(\pi^0\pi^0)$	[MeV^2]	10'540	-
$s(\eta\pi^0)$	[MeV^2]	-	11'820
$s(\omega\eta)$	[MeV^2]	-	14'700
$\phi(\omega \to \pi^0\gamma)$	[rad]	0.037	0.044
$\theta(\omega \to \pi^0\gamma)$	[rad]	0.027	0.032
$\cos\theta(\omega \to \pi^0\gamma)$		0.017	0.022

Table 12: *Monte Carlo study of detection resolution. The error is of the order of* 1%. *$m(\pi^0\gamma)$ refers to the $\pi^0\pi^0\pi^0\gamma$ and $\eta\pi^0\pi^0\gamma$ selection (see section 4.3)*

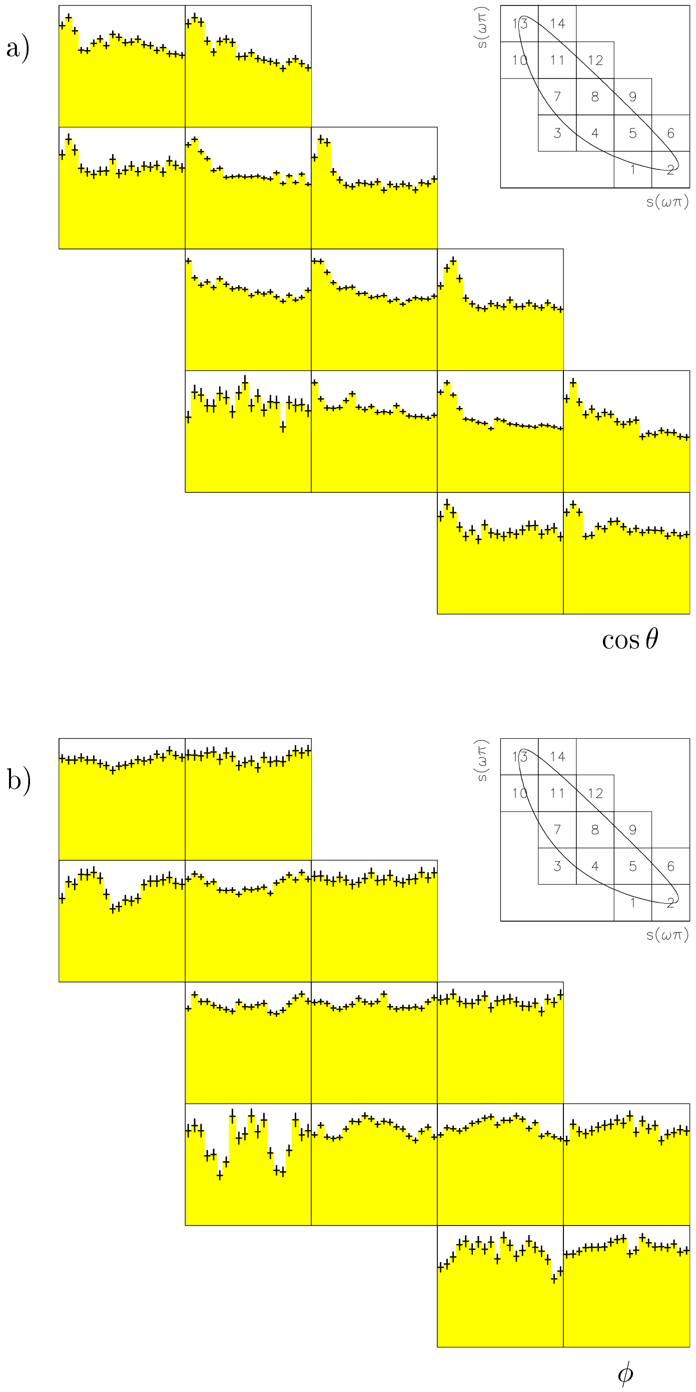

Figure 28: *Acceptance in* $\cos\theta$ *(a) and in* ϕ *(b) for* $\omega\pi^0\pi^0$ *phase space events, determined by Monte Carlo simulation (see also caption of fig. 24).*

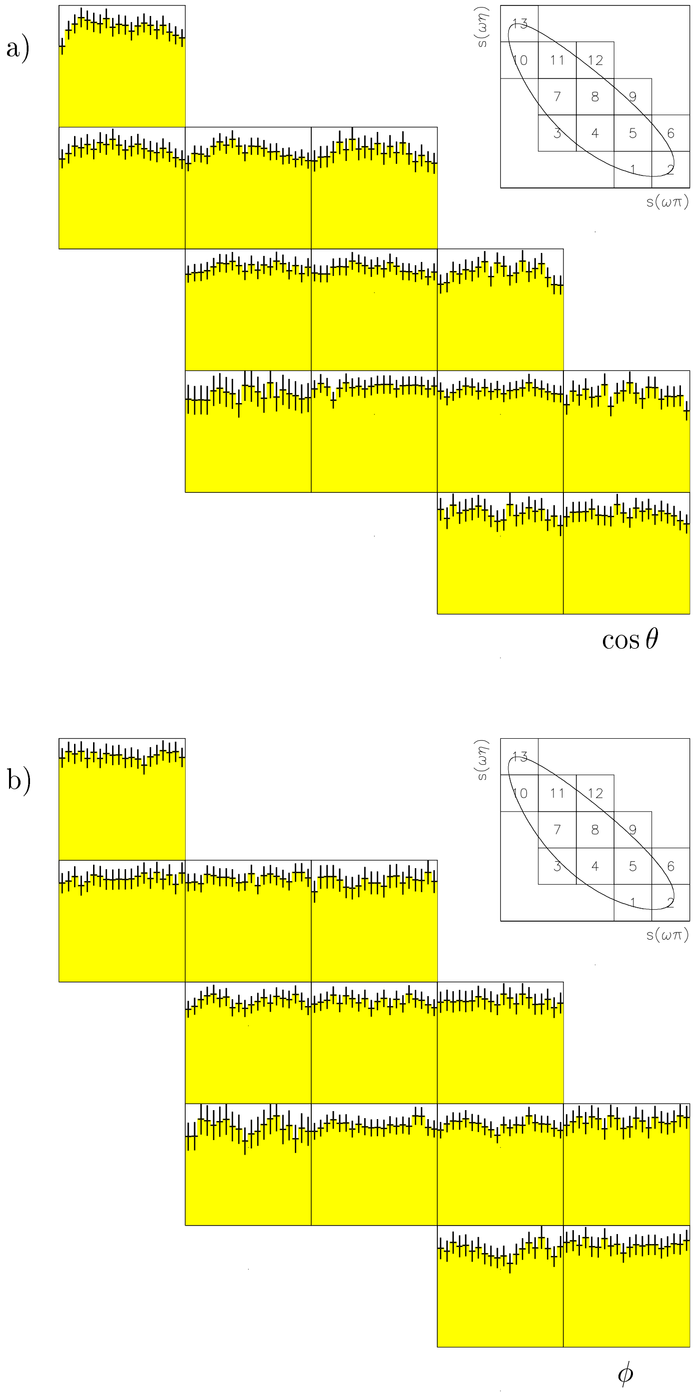

Figure 29: *Acceptance in* $\cos\theta$ *(a) and in* ϕ *(b) for* $\omega\eta\pi^0$ *phase space events, determined by Monte Carlo simulation (see also caption of fig. 25).*

5.4 Combinatorial Reconstruction

Besides improving the measurements, the kinematic fit aims to find the correct photon combination for the event kinematics. Nevertheless, a certain amount of the data is combinatorially wrongly reconstructed.

These events are studied by comparing closely the generated and the reconstructed Monte Carlo events. In figure 30, the x-component of the generated ω momentum $p_x^{gen}(\omega)$ is plotted versus the reconstructed momentum $p_x^{rec}(\omega)$. The finite width of the diagonal band is due to the detector resolution. The events scattered almost uniformly over the whole kinematic region are combinatorially mismatched events. The inset contains the distribution of $\Delta p = p_x^{gen}(\omega) - p_x^{rec}(\omega)$, where the 2σ region around zero ($\pm 25\,\mathrm{MeV}$) is cut out, in order to show the remaining combinatorial events. The detailed study of the phase space Monte Carlo shows that around $8\,\%$ of the simulated $\omega\pi^0\pi^0$ data and $6\,\%$ of $\omega\eta\pi^0$ are combinatorially mismatched.

Figure 31 shows the relative density alteration of the $\omega\pi^0\pi^0$ Dalitz plot due to combinatorial effects in the reconstruction. The generated phase space Monte Carlo events are weighted with the theoretical transition probability retrieved from the partial wave analysis (see sec. 8.5). The dark spots show the relative enhancement of the reconstructed data with respect to the generated data. The enhancement in the region between the b_1 bands reflects the fact that this zone is depleted and that the combinatorial events are relatively abundant. This is also the region, where peaks in the $\cos\theta$ distribution (fig. 24, 25) are observed, stemming from kinematic arrangements which are favored for combinatorial mismatching.

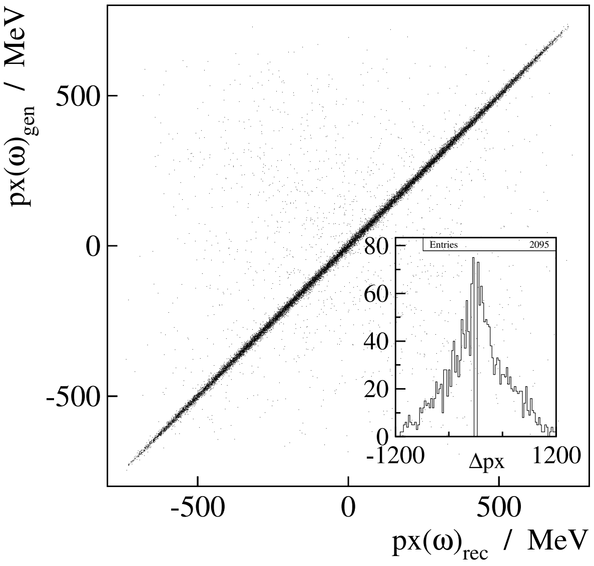

Figure 30: *Reconstruction of ω momenta for simulated $\omega\pi^0\pi^0$ events (25'000 entries). The x-component of the generated ω momentum $p_x^{gen}(\omega)$ is plotted versus the reconstructed momentum $p_x^{rec}(\omega)$. The inset contains the distribution of $\Delta p = p_x^{gen}(\omega) - p_x^{rec}(\omega)$ (2095 entries), where the 2σ region around zero (± 25 MeV) is cut out.*

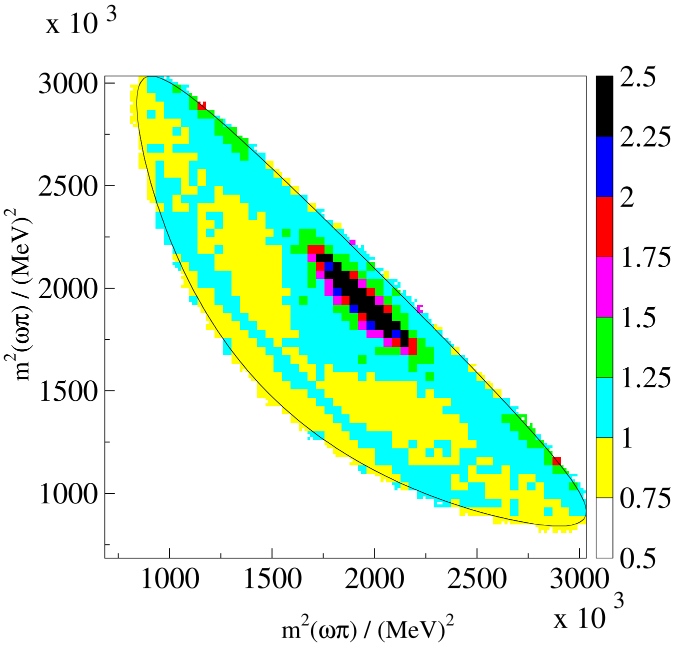

Figure 31: *The relative contribution of combinatorial events on the $\omega\pi^0\pi^0$ Dalitz plot (see text).*

6 Background

6.1 Background Channels

Monte Carlo simulations show that background stems mainly from channels decaying into 8γ (see table 10 and 11), where two π^0 are reconstructed as an ω when one of the γ's has very low energy and therefore escapes detection. The two channels contributing the most are $4\pi^0$ and $3\pi^0\eta$ (see table 13).

				feedthrough [%]	
channel	PED	BR($\bar{p}p \to$channel)		$\omega\pi^0\pi^0$	$\omega\eta\pi^0$
$\omega\eta\pi^0$	7γ	0.68(5) %	[30]	0.0	
$\omega\pi^0\pi^0$	7γ	2.57(17) %	[38]		1.2(2)
$\pi^0\pi^0\pi^0\eta$	8γ	$5.1(5) \cdot 10^{-4}$	[43], [48]	0.0	2.6(3)
$\pi^0\pi^0\pi^0\pi^0$	8γ	0.45(3)	[47]	11.2(8)	1.3(2)
$\pi^0\pi^0\pi^0$	6γ	0.61(10) %	[44]	0.4(1)	0.4(1)
$\pi^0\pi^0\eta$	6γ	0.67(12) %	[45]	0.0	0.8(3)
$\pi^0\eta\eta$	6γ	0.20(4) %	[46]	-	0.10(3)
$\omega\eta$	9γ	1.51(12) %	[48]	-	0.16(4)
total feedthrough				11.6(8)	6.6(5)

Table 13: *Feedthrough channels. The contributions in the signal region are calculated based on Monte Carlo studies of their detection probability (see table 10 and 11) and on the known branching ratios for $\bar{p}p$ annihilation.*

6.2 Background Contribution

The contribution of the simulated background channels listed in table 13 depends on the branching ratios of the involved reactions. In the following, two different methods are used to determine the absolute background.

- Method 1: scaling to the ω mass peak.

  This method is based on the ω mass fit (see section 4.3). The contents of the Voigtian, fitted to the $\pi^0\gamma$ mass spectrum before applying the kinematic fit for $\omega\pi^0\pi^0$ and $\omega\eta\pi^0$, is proportional to the number of true events in the final selection. The ratio of events in the Voigtian and of true events surviving all cuts is determined by means of Monte Carlo data and allows to calculate the number of true events in the selected sample. The remaining events are assigned to the background. Each sample of $\pi^0\pi^0\pi^0\gamma$ and $\eta\pi^0\pi^0\gamma$ events is selected with both 7C cuts (eq. (27),(28) and eq. (31),(32)). The anticut prevents the feedthrough from the competing channel also containing an ω. The results are listed in table 14.

- Fit of the $\pi^0\gamma$ spectrum

  Another method is to fit the $\pi^0\gamma$ mass line shape of the real data with a linear superposition of the simulated background and the signal channel. The fit is restricted to the ω mass region from 700 to 860 MeV. With the fraction of feedthrough, known from the selection of Monte Carlo data, and with the fitted contribution to the spectrum, one can calculate the amount of background in the final selection. The fits together with the measured channel and the background hypothesis are shown in figure 32 for $\omega\pi^0\pi^0$ and $4\pi^0$ background and in figure 33 for $\omega\eta\pi^0$ and $\eta\pi^0\pi^0\pi^0$ background. The results are given in table 14 for the background hypothesis $4\pi^0$ ($\eta\pi^0\pi^0\pi^0$) and, in order to investigate for further background, also for $\pi^0\pi^0\pi^0\gamma$ ($\eta\pi^0\pi^0\gamma$).

For both methods, one has to ensure that the ω peak in the $\pi^0\gamma$ spectrum contains only signal events. The Monte Carlo simulation shows that the feedthrough into the peak from the competing channel ($\omega\pi^0\pi^0$, $\omega\eta\pi^0$) can be neglected.

The methods are not completely independent since both are based on Monte Carlo data. However, the two methods are complementary in the sense that the first method depends on the selection efficiency of the signal and the second on the feedthrough probability of the background channels. The good agreement of both methods strengths the reliability of the Monte Carlo for background simulations.

	$\omega\pi^0\pi^0$	$\omega\eta\pi^0$
Method 1: ω peak	9.6±0.6%	6.4±0.6%
Method 2a: $\pi^0\gamma(8\gamma)$	8.9±0.4% ($4\pi^0$)	6.9±0.3% ($\eta\pi^0\pi^0\pi^0$)
Method 2b: $\pi^0\gamma(7\gamma)$	9.9±0.3% ($\pi^0\pi^0\pi^0\gamma$)	7.1±0.2% ($\eta\pi^0\pi^0\gamma$)
Weighted mean:	9.7±0.2%	6.9±0.2%

Table 14: *Background contribution (see text).*

The weighted average of the background fractions from methods 1 and 2 leads to the following numbers of true events in the sample

$$N(\omega\pi^0\pi^0) = 122'830 \pm 430 \quad (43)$$

$$N(\omega\eta\pi^0\ ) = 31'710 \pm 190 \quad (44)$$

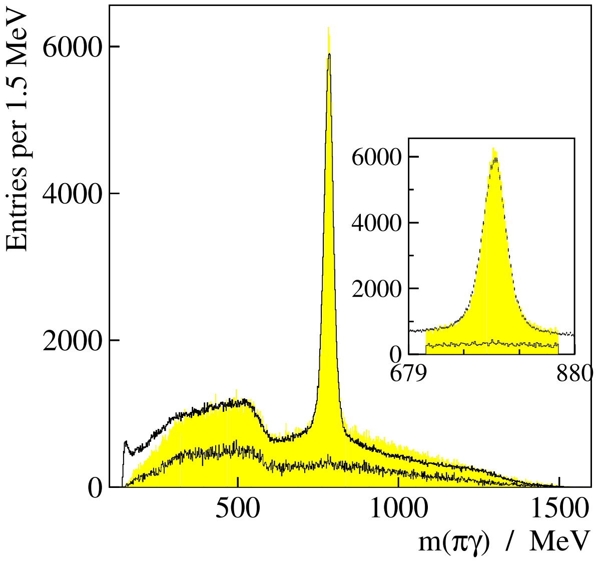

Figure 32: *Background fit of the* $\pi^0\gamma$ *mass spectrum of* $\pi^0\pi^0\pi^0\gamma$*. The data (upper line, 3×214'050 entries) are fitted with a linear superposition (shaded) of the simulated* $4\pi^0$ *feedthrough events (lower line without peak) and simulated* $\omega\pi^0\pi^0$ *events. The inset shows details of the fitted mass region (shaded). The* $3\pi^0\gamma$ *sample is selected by applying only the CL cut eq. (27) and (28).*

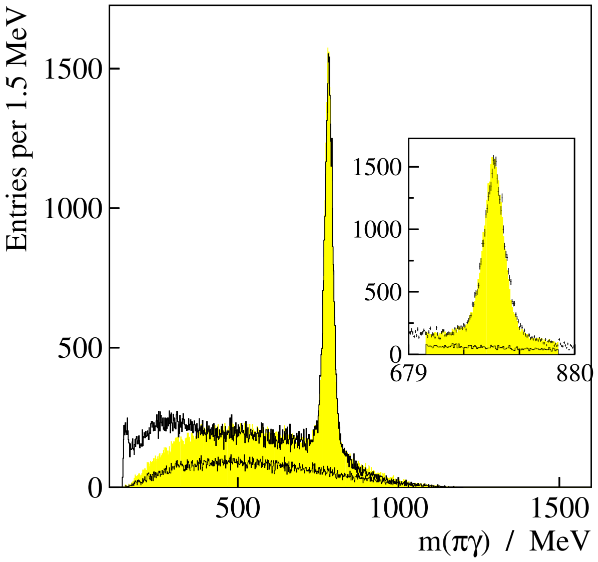

Figure 33: *Background fit of the* $\pi^0\gamma$ *mass spectrum of* $\eta\pi^0\pi^0\gamma$*. The data (upper line, 2×60'728 entries) are fitted with a linear superposition (shaded) of the simulated* $\eta3\pi^0$ *feedthrough events (lower line without peak) and simulated* $\omega\eta\pi^0$ *events. The inset shows details of the fitted mass region (shaded). The* $\eta\pi^0\pi^0\gamma$ *sample is selected by applying only the CL cut eq. (31) and (32).*

One can estimate the strong feedthrough from $4\pi^0$ by studying also the channel $\eta\pi^0(\eta \to 3\pi^0)$. The $3\pi^0$ invariant mass spectrum of the selected $\pi^0\pi^0\pi^0\gamma$ events including all cuts has a little peak in the η mass region (see fig. 34) The fit with a Gaussian on top of a second order polynomial peaks at $m = (547.3 \pm 1.3)\,\mathrm{MeV/c^2}$ ($\sigma = 5.2 \pm 1.2$) with $N_P = 51.5 \pm 17.0$ events in the Gaussian, while 288 ± 29 of 300'000 Monte Carlo simulated $\eta\pi^0(\eta{\to}3\pi^0)$ events contribute to the signal with an efficiency of $\epsilon_P = 0.096 \pm 0.010\%$. Taking into account the efficiency for detecting $4\pi^0$ feedthrough ($\epsilon_F = 0.77 \pm 0.08\%$) and the known branching ratios ($B(4\pi^0) = 0.45(3)\%$[47], $B(\eta\pi^0) = 2.12(12){\cdot}10^{-4}$[48] and $B(\eta{\to}3\pi^0)$ [8]) one gets for the number of $4\pi^0$ feedthrough events

$$N_F = \frac{B(\pi^0\pi^0\pi^0\pi^0)}{B(\eta\pi^0, \eta{\to}3\pi^0)}\frac{\epsilon_F}{\epsilon_P}N_P = 27'500 \pm 9'900 \tag{45}$$

corresponding to the fraction of $20{\pm}9\,\%$ which is compatible (within the errors) with method 1 and 2. The distribution of the simulated $\eta\pi^0(\eta{\to}3\pi^0)$ events, however, reproduces the peak at η mass less accurately than the real data, indicating that the efficiency ϵ_P may be somewhat underestimated.

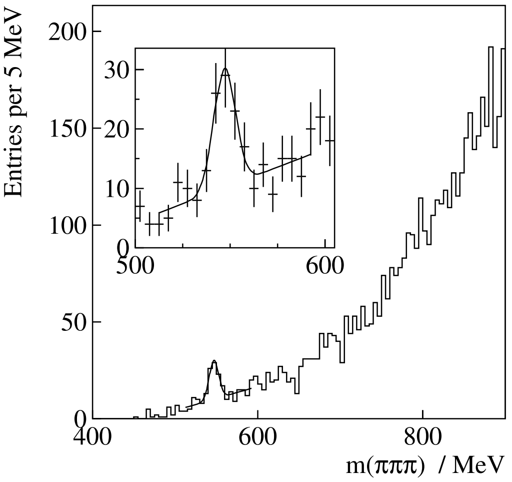

Figure 34: $3\pi^0$ *mass spectrum of* $\pi^0\pi^0\pi^0\gamma$ *events. The peak at the* η *mass is due to the* $\eta\pi^0(\eta{\to}3\pi^0)$ *feedthrough*

The results summarized in table 14 show that the background contributions are fairly well described by $4\pi^0$ and $\eta3\pi^0$ feedthrough events and, alternatively, also by phase space distributed $\pi^0\pi^0\pi^0\gamma$ and $\eta\pi^0\pi^0\gamma$ events. Figure 35 displays the simulated $4\pi^0$ and $\eta3\pi^0$ background Dalitz plots.

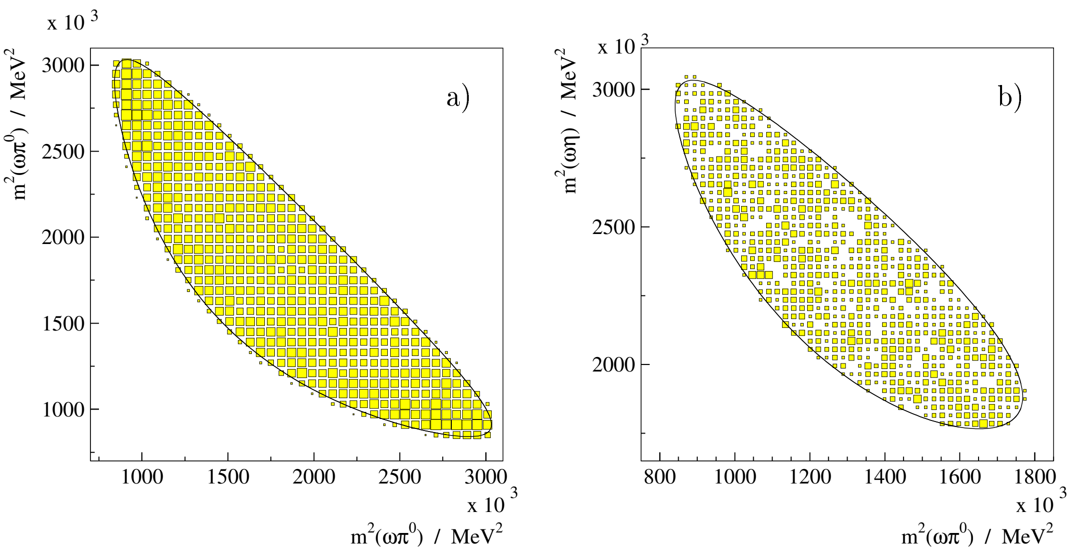

Figure 35: *(a)* $4\pi^0$ *background Dalitz plot of* $\omega\pi^0\pi^0$ *and (b)* $\eta 3\pi^0$ *background Dalitz plot of* $\omega\eta\pi^0$*.*

7 Branching Ratios $\overline{p}p \rightarrow \omega\pi^0\pi^0$ and $\overline{p}p \rightarrow \omega\eta\pi^0$

The branching ratios of the reactions $\bar{p}p\rightarrow X$ $(X = \omega\pi^0\pi^0, \omega\eta\pi^0)$ are determined by

$$B(\bar{p}p\rightarrow X) = \frac{N(X)}{N_0}\,\frac{B_0}{\epsilon(X)\;B(X\rightarrow 7\gamma)} \tag{46}$$

N denotes the number of background free events ($122'830 \pm 430$ and $31'710 \pm 190$) which are reconstructed with an efficiency of ϵ (12.37% and 20.56%) from $N_0 = 17.4 \pm 0.2 \times 10^6$ all-neutral events. This number is obtained from the number of 0-prong triggered events (19.2×10^6) by correcting for annihilation outside the target ($3.9\pm0.7\,\%$) and for annihilation occurring in-flight ($5.7\pm1.1\,\%$)[48]. The all-neutral events correspond to the fraction $B_0 = (3.9 \pm 0.3)\%$ [29] of all $\bar{p}p$ annihilations occurring in the target. With the ratios $B(\omega\pi^0\pi^0\rightarrow 7\gamma) = 8.20 \pm 0.48\,\%$ and $B(\omega\eta\pi^0\rightarrow 7\gamma) = 3.25 \pm 0.19\,\%$, derived from the PDG values for the radiative decays of ω, η and π^0 [8], one finds finally the following branching ratios

$$B(\overline{p}p \rightarrow \omega\pi^0\pi^0) = (2.71 \pm 0.03_{\text{stat}} \pm 0.25_{\text{sys}} \pm 0.26_{\text{BR}})\ \% \tag{47}$$

$$B(\overline{p}p \rightarrow \omega\eta\pi^0) = (1.06 \pm 0.01_{\text{stat}} \pm 0.15_{\text{sys}} \pm 0.10_{\text{BR}})\ \% \tag{48}$$

The first error is statistical and refers to the number of selected events N, while the second corresponds to the systematic uncertainty in the determination of the reconstruction and detection efficiency. The errors of the branching ratios B_0 and $B(X\rightarrow 7\gamma)$ are summarized in the third error. For the estimation of the systematic error of the detection efficiencies, we consider the variability of the yield for different run periods. The relative yield of individual run periods has a standard deviation of 11.2% and 15.3%, respectively, which exceeds significantly the statistical error (0.9%, 1.8%). Hence, we assume that the fluctuations are due to an unknown systematic error and translate it into an uncertainty of the determined detection efficiencies.

The value for $B(\omega\pi^0\pi^0)$ in liquid hydrogen is somewhat higher than the value of $2.00 \pm 0.21\,\%$ (from the analysis based on 15'153 events [29]), but agrees very well with $2.57 \pm 0.06_{\text{stat}} \pm 0.16_{\text{sys}}\,\%$ from an analysis of $\overline{p}p \rightarrow \omega\pi^0\pi^0$, $\omega \rightarrow \pi^+\pi^-\pi^0$ [38] (9'180 events). From the bubble chamber result $B(\bar{p}p \rightarrow \omega\pi^-\pi^+) = 6.6 \pm 0.6\,\%$ [31] (3778 events), after subtracting the contribution of $\omega\rho^0$ ($2.26\pm0.23\%$), which comes only from ${}^1S_0$ initial state, and taking into account the isospin symmetry factor 2, one gets a $\omega\pi^0\pi^0$ ratio of $2.17 \pm 0.32\,\%$ which is in good agreement with all three measurements. However, the contribution from ${}^1S_0$ in the bubble chamber data may be overestimated. A re-analysis of the data suggests rather a ${}^1S_0$ contribution of about 10 % [32] compared to 34 % in ref. [31].

Our value for $B(\omega\eta\pi^0)$ is significantly higher than the previous measurement $0.68 \pm 0.01_{\text{stat}} \pm 0.05_{\text{sys}}\,\%$ [30] based on 10'662 selected events, but in excellent agreement with the measurements of ref. [49], where $B(\bar{p}p \rightarrow \pi^+\pi^-\pi^0\pi^0\eta)$ is determined independently from three different branching ratios, from $B(\bar{p}p \rightarrow \omega\eta\pi^0, \omega \rightarrow \pi^+\pi^-\pi^0)$, $B(\bar{p}p \rightarrow \eta\eta\pi^0, \eta \rightarrow \pi^+\pi^-\pi^0)$ and $B(\bar{p}p \rightarrow \pi^-\pi^+3\pi^0)$. The branching ratios derived from the new (old) measurement of $B(\omega\eta\pi^0)$ is $2.77 \pm 0.33\,\%$ ($1.78 \pm 0.21\,\%$) and agrees with $3.24 \pm 0.65\,\%$ from $B(\eta\eta\pi^0)$ and with $2.78 \pm 0.40\,\%$ from $B(\pi^-\pi^+3\pi^0)$ and the measured relative ratio $B(\pi^-\pi^+3\pi^0)/B(\pi^-\pi^+\pi^0\pi^0\eta)$. Averaging one gets $B(\bar{p}p \rightarrow \pi^+\pi^-\pi^0\pi^0\eta) = 2.81 \pm 0.18\,\%$ ($2.09 \pm 0.36\,\%$).

8 Partial Wave Analysis

8.1 Transition Amplitude in Helicity Formalism

According to the isobar model [50], $\bar{p}p$ annihilates through subsequent two-body decays. The transition amplitude of a decaying isobar contains an angular part, conserving angular momentum, and a dynamical part which describes the energy dependence of the decay.

In the helicity formalism [51] the decay of a isobar with spin J into two particles with spin s_1 and s_2 is expressed in terms of helicity states

$$|\,JM\rangle \longrightarrow |\,s_1\lambda_1\rangle \otimes |\,s_2\lambda_2\rangle \tag{49}$$

The angular dependence of the decay into a final state with orbital angular momentum L and the total spin S is given by the matrix

$$H^{JLS}_{s_1 s_2}(\phi,\theta,\psi) \quad = \quad \langle s_1 s_2 \lambda_1 \lambda_2;\, LS;\, \phi\theta\psi\,|\,JM\rangle$$

respectively

$$H^{JLS}_{s_1 s_2}(\phi,\theta,\psi) = \sqrt{\frac{2J+1}{4\pi}}\, D^{J*}_{M\lambda}(\phi,\theta,\psi)\, \langle s_1 s_2\ \lambda_1\ {-\lambda_2} \mid S\lambda\rangle\, \langle LS0\lambda \mid J\lambda\rangle \tag{50}$$

The row index $\lambda = \lambda_1 - \lambda_2$ runs over $(2s_1+1)(2s_2+1)$ final state helicities, the column index M over $2J+1$ magnetic states. $D^{J*}_{M\lambda}$ represents the rotation of the spin state $|\,JM\rangle$ into the decay direction, $|\,\phi\theta\psi; J\lambda\rangle$, while ϕ, θ and ψ are the three Euler angles of the rotation. The D-matrix is expressed in the usual form as

$$D^{J*}_{M\lambda}(\phi,\theta,\psi) = e^{i\phi M}\, d^{J}_{M\lambda}(\theta)\, e^{i\psi\lambda} \tag{51}$$

where $d^{J}_{M\lambda}(\theta)$ represents the rotation around the y-axis. Since angles ϕ and θ already define the decay direction, the third angle (ψ) is usually set by convention to zero [3].

The transition amplitude including the dynamical function $F^L_R(m)$ which describes the dependence on the invariant mass m of the final state is given by the product

$$A^{JLS}_R = H^{JLS}_{s_1\,s_2}\, F^L_R(m) \tag{52}$$

---

[3] See e.g. ref. [52] [53] [55]. One can also find the convention $\psi = -\phi$, for instance in the pioneering work of Jacob and Wick[51] and in ref. [56] [57].

The dynamical part of the $\bar{p}p$ annihilation into two states is described by the Blatt-Weisskopf damping factors $B_L(q)$, which suppress decays with low break-up momenta q at high angular momenta [58]:

$$\begin{aligned} B_0(q) &= 1 \\ B_1(q) &= \sqrt{2z/(z+1)} \\ B_2(q) &= \sqrt{13z^2/((z-3)^2+9z)} \ , \end{aligned} \tag{53}$$

where $z = q^2/(197.3\,\mathrm{MeV}/c)^2$. The break-up momentum of the daughter particles at mass m is given by

$$q(m) = \frac{1}{2m}\sqrt{(m^2-(m_1+m_2)^2)(m^2-(m_1-m_2)^2)} \tag{54}$$

The dynamical function $F_R^L(m)$ of a resonant state R can be quite complicated, namely if a decay channel opens near the kinematic threshold or in the case of overlapping resonances with equal quantum numbers (J^{PC}, L, S) as it occurs in the $(\pi\pi)_S$ wave. For a general way of describing the dynamics of resonances, see section 8.3. Nevertheless, in most of the cases, the relativistic Breit-Wigner parametrization gives a satisfactory description:

$$F_R^L(m) = \frac{m_0\Gamma_0}{m_0^2 - m^2 - im_0\Gamma(m)} B_L(q, q_0) \tag{55}$$

where

$$\Gamma(m) = \Gamma_0 \frac{m_0}{m}\frac{q}{q_0} B_L^2(q, q_0) \quad \text{and} \quad B_L(q, q_0) = \frac{B_L(q)}{B_L(q_0)} \tag{56}$$

The nominal mass and width of the resonance are m_0 and Γ_0, q and q_0 are the break-up momenta at the masses m and m_0, respectively.

In the reactions $\overline{p}p \to \omega\pi^0\pi^0$ and $\overline{p}p \to \omega\eta\pi^0$, there are three kinematic types of decay chains, depending on whether the ω is produced directly from $\bar{p}p$ recoiling to a resonance in the $\pi\pi(\eta\pi)$ system or indirectly via a resonance in the $\omega\pi_1$ or in the $\omega\pi_2(\omega\eta)$ system. The three chains including $\omega \to \pi^0\gamma$ are described by matrix multiplication of the involved two-body decays [53]:

$$\begin{aligned} A^{(1)} &= [\,A^{111}(\,\omega \to \pi^0\gamma\,) \otimes A^{j\,l0}(\,R^{(1)} \to \eta\pi^0\,)\,]\ A^{JLS}(\,\bar{p}p \to \omega R^{(1)}\,) && (57) \\ A^{(2)} &= \ A^{111}(\,\omega \to \pi^0\gamma\,)\ A^{j\,l1}(\,R^{(2)} \to \omega\pi^0\,)\ \ A^{JLj}(\,\bar{p}p \to R^{(2)}\eta\,) && (58) \\ A^{(3)} &= \ A^{111}(\,\omega \to \pi^0\gamma\,)\ A^{j\,l1}(\,R^{(3)} \to \omega\eta\,)\ \ A^{JLj}(\,\bar{p}p \to R^{(3)}\pi^0\,) && (59) \end{aligned}$$

The decay angles (ϕ, θ) of the intermediate states (R, ω) are obtained by following the decay chain through a series of Lorentz boosts and frame rotations which connect the initial frame to the helicity frames of the final state particles. There are only two helicity states in the final state system, since π^0 and η are spinless, and γ appears only in helicities ±1. The transition matrix of the decay chain is therefore a complex $(2J+1)\times 2$ matrix.

The total transition amplitude for a given atomic $\bar{p}p$ state J^{PC} is a superposition of all allowed decay chains i:

$$A(J^{PC}) = \sum_{i}^{\text{chains}} \alpha_i A_i(J^{PC}) \tag{60}$$

The complex parameters α_i are unknown and have to be determined by fitting the data. The total transition probability w_A is then given by the sum over all atomic initial states

$$w_A = \sum_{J^{PC}}^{\text{initial}} \text{Tr}\; A(J^{PC})\, \rho_i(J^{PC})\, A(J^{PC})^\dagger \tag{61}$$

where ρ_i denotes the $(2J+1)\times(2J+1)$ spin density matrix of the initial state J^{PC}. In annihilation at rest, where no polarization occurs, it is $\rho_i = \mathbf{1}/(2J+1)$.

The (helicity-)coupling α^{JLS} can be related to the LS-coupling G^J_{LS} by using the formulas given for instance in ref. [54]:

$$G^J_{LS} = \frac{1}{\sqrt{4\pi}} \frac{2J+1}{\sqrt{2L+1}}\, \alpha^{JLS} \tag{62}$$

Thus, for example, the ratio of the orbital angular momenta of the b_1 decay is

$$D/S = \frac{|\,G^J_2\,|}{|\,G^J_0\,|} = \frac{1}{\sqrt{5}} \frac{|\,\alpha(l=2)\,|}{|\,\alpha(l=0)\,|}\ . \tag{63}$$

8.2 Phase Correction of the Helicity Amplitudes

With the requirement of coherence between the decay chains, the corresponding partial wave amplitudes have to refer to the same final state (helicity) frames. For spinless particles, the orientations of the helicity frames are arbitrary and, hence, coherence is always ensured. The situation is different if particles with spin (ω,γ) are involved in the final state. In the following, we derive the correction needed to fulfill this requirement for the studied annihilation channels.

According to the different types of decay chains (eq. (57),(58),(59)), there are three distinct ways to produce the ω. Hence, following a decay chain, one has to consider one of the three possible production directions ($\vec{z}_1^{\,\omega}$, $\vec{z}_2^{\,\omega}$ and $\vec{z}_3^{\,\omega}$) from where one goes into the decay system of the ω. After the rotation into $\omega \to \pi^0\gamma$, the z-axis corresponds to the γ flight direction ($\vec{z}^{\,\gamma}$) which is given unambiguously by the decay kinematics of the ω [4]. However, in contrast to the z-axis, x and y depend on the direction $\vec{z}_i^{\,\omega}$. The resulting relative twist of the three helicity frames is illustrated in figure 36. This is a consequence of the conventional rotation (a rotation around z followed by a rotation around y) which implies that the y-axis is parallel to the product $\vec{z}_i^{\,\omega} \times \vec{z}^{\,\gamma}$.

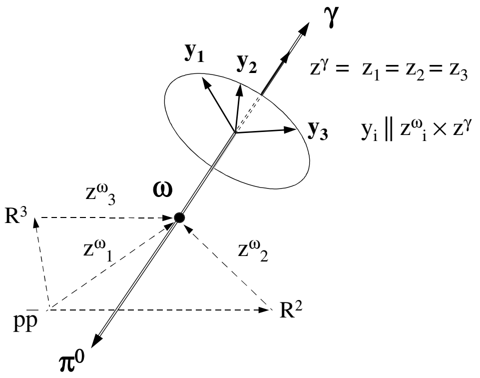

Figure 36: *Alignment of the conventional helicity frame of $\omega \to \gamma\pi^0$. Depending on the decay chain and, hence, on the ω production direction (z^i_ω), the x- and y-axis (y_i) are twisted.*

Coherence requires that the frames are aligned and, hence, a further rotation (ψ_i) around z to correct the amplitudes

$$A_i \;\to\; D^{S*}(\psi_i, 0, 0)\, A_i = e^{-i\lambda\psi_i} A_i \tag{64}$$

where λ denotes the photon helicity. For calculating the angles ψ_i, one of the three frames or an arbitrary frame may be chosen as reference system. The correction depends on the kinematics and has to be therefore determined for each individual event. The angle ψ_i can be interpreted as the third degree of freedom of the D-function neglected in the conventional definition.

To illustrate the effect of the misalignment, we consider the total amplitude containing only the two combinatorial possibilities of the intermediate state $b_1 \to \omega\pi^0$ in $\overline{p}p \to \omega\pi^0\pi^0$. The Monte Carlo simulated Dalitz plots for corrected and uncorrected amplitudes calculated with an adapted versions of SPIN [59] are shown in figure 37. In the given examples b_1 and ω are produced with orbital angular momenta $L = 0$

---

[4] We assume that interference between the decay products π^0 and γ and other final state particles are negligible, due to the long life time of the ω

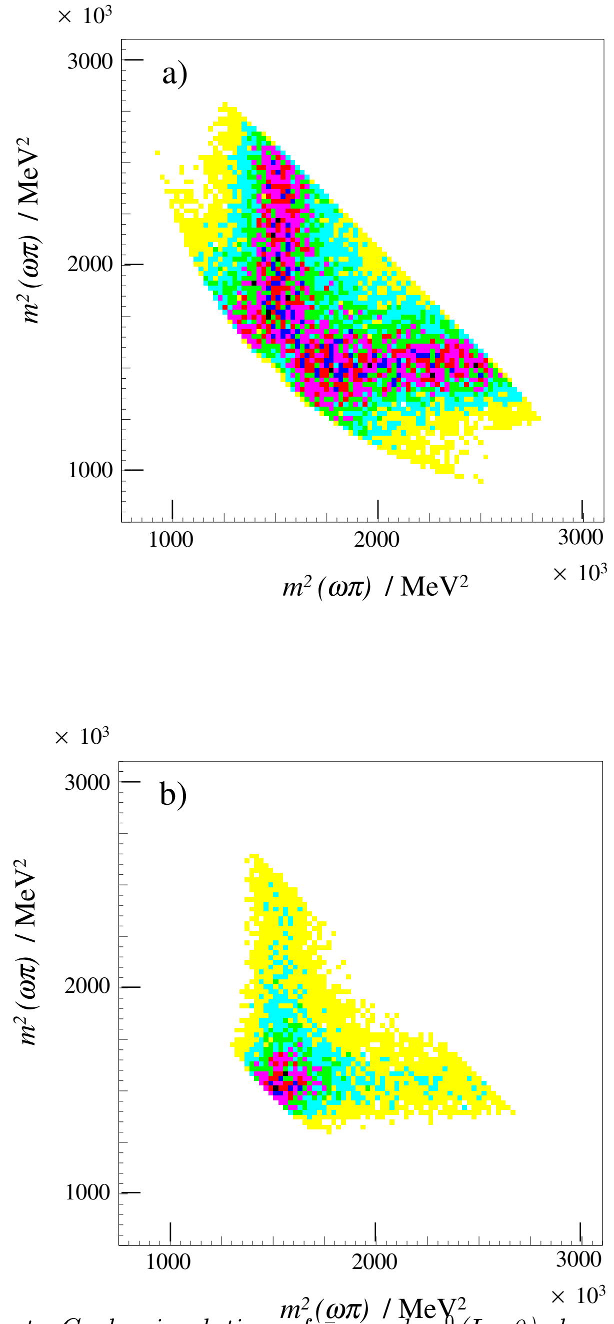

Figure 37: *Monte Carlo simulation of* $p\bar{p} \to b_1\pi^0$ *(L=0),* $b_1 \to \omega\pi^0$ *(l=0) for (a) uncorrected and (b) phase corrected transition amplitude (see text).*

and $l=0$ respectively. The destructive behavior at the crossing of the b_1 bands near the border of the Dalitz plot is due to the misalignment (fig. 37a). In contrast, the corrected amplitude corresponds to a constructive interference pattern (fig. 37b), in agreement with the expected behavior for $L=l=0$.

Since the orientation of the annihilation at rest is arbitrary, it is convenient to reduce the number of rotations by setting the y-axis of the initial frame perpendicular to the three-body decay plane and the z-axis parallel to the ω flight direction (see fig. 38). The rotation (θ_0^k) into the decay direction of the $\bar{p}p$ is then only required for type 2 and 3, whereas the decay direction of the intermediate state $R^{(k)}$ is given by the polar angle θ_R^k. The decay of the ω leaves the three-body plane and is described by the pair of angles (θ^k, ϕ^k). The phase correction factors $e^{-\lambda\psi^k}$ are only needed for chain type 2 and 3, since the reference system is given by chain type 1. The three types of decay chains can then be written in terms of four independent decay angles $(\theta_0, \theta_R, \theta, \phi)$ as

$$A^{(1)} = [\, H^{111}_{10}(\theta^1,\phi^1) \otimes H^{jls}_{00}(\theta^1_R,0)\,]\; H^{JLS}_{1j}(0,0)\; B_L(q^1_R)\, F^l_{R^1}(s^1) \tag{65}$$

$$A^{(2)} = e^{-i\lambda\psi^2}\; H^{111}_{10}(\theta^2,\phi^2)\; H^{jls}_{10}(\theta^2_R,0)\, H^{JLS}_{j0}(\theta^2_0,0)\; B_L(q^2_R)\, F^l_{R^2}(s^2) \tag{66}$$

$$A^{(3)} = e^{-i\lambda\psi^3}\; H^{111}_{10}(\theta^3,\phi^3)\; H^{jls}_{10}(\theta^3_R,0)\, H^{JLS}_{j0}(\theta^3_0,0)\; B_L(q^3_R)\, F^l_{R^3}(s^3) \tag{67}$$

Neglecting the decay dynamics of the ω the dynamical part of the transition (B_L and F^l_R) depends only on the invariant mass $\sqrt{s^k}$ of the resonant system and its momentum q^k_R in the annihilation system.

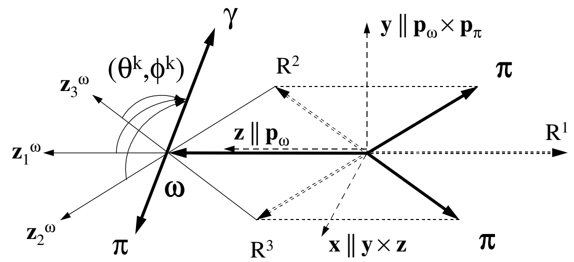

Figure 38: *The conventional rotation into the $\omega \to \pi^0\gamma$ decay system and the special choice of initial frame. (θ^k, ϕ^k) denotes the ω decay angle corresponding to chain k.*

One can absorb the phase correction into an additional rotation $D^{1*}(\theta_{k1}, 0)$ in the three-body plane:

$$e^{-i\lambda\psi^k} H^{111}_{10}(\theta^k, \phi^k) = D^{1*}(\theta_{k1}, 0)\; H^{111}_{10}(\theta, \phi) \tag{68}$$

where θ_{k1} denotes the angle between the production directions $\vec{z}^{\,\omega}_k$ and $\vec{z}^{\,\omega}_1$ in the center of mass system of the ω. The new sequence of rotations is shown in fig. 39.

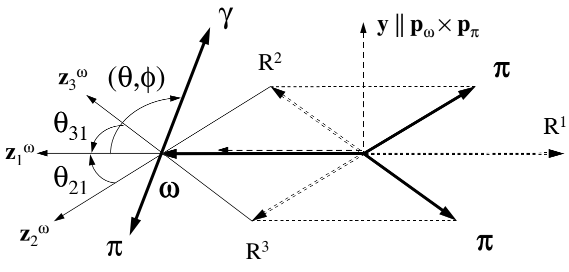

Figure 39: *The intermediate rotation into the $\omega \to \pi^0\gamma$ decay system for the special choice of initial frame. θ^{k1} denotes the intermediate angle of chain k. (θ, ϕ) is the rotation into $\omega \to \pi^0\gamma$.*

The substitution allows to separate the ω decay term $H^{111}_{10}(\theta, \phi)$ from the total transition amplitude:

$$A(j^{PC}) = H^{111}_{10}(\theta, \phi)\; \sum_i \alpha_i\, \tilde{A}_i(J^{PC}) \tag{69}$$

while

$$A_i = H^{111}_{10}(\theta, \phi)\; \tilde{A}_i\ . \tag{70}$$

$\tilde{A}_i$ is a $(2J{+}1){\times}3$ matrix depending only on the kinematics of the three-body system, $\overline{p}p \to \omega\pi^0\pi^0$ or $\overline{p}p \to \omega\eta\pi^0$. This is very convenient for computing, because the total amplitude A can be separated into two functions, each depending on only two of the four kinematic variables (see section 8.4.1). Some of the helicity amplitudes of $\tilde{A}_i$ are given in the appendix A.

8.3 Dynamics in K-matrix Formalism

According to the K-Matrix formalism, the Lorentz invariant transition amplitude $\hat{T}$ of a scattering process can be expressed in terms of a symmetric and real matrix $\hat{K}$:

$$\hat{T} = \hat{K}(\mathbf{1} - i\rho\hat{K})^{-1} = (\mathbf{1} - i\hat{K}\rho)^{-1}\hat{K} \tag{71}$$

ρ is the phase-space density matrix with the diagonal elements $\rho_i(m) = 2q_i(m)/m$ where q_i are the breakup momenta of the two-body channels i (eq. (54)). The resonant scattering is described by a sum of poles α in the K-matrix [60] [61]:

$$\hat{K}_{ij} = \sum_{\alpha} \frac{\hat{g}_{\alpha i}(m)\hat{g}_{\alpha j}(m)}{m_\alpha^2 - m^2} + c_{ij} \tag{72}$$

with the (real) couplings related to the partial width $\tilde{\Gamma}_{\alpha i}$ via

$$\hat{g}_{\alpha i}(m) = g_{\alpha i}\, B^L_{\alpha i}(m) = \sqrt{\frac{m_\alpha \tilde{\Gamma}_{\alpha i}}{\rho_i(m_\alpha)}}\, B^L_{\alpha i}(m) \tag{73}$$

including the suppression of low breakup momenta at high angular momenta L given by ratios of Blatt-Weisskopf damping factors

$$B^L_{\alpha i}(m) = \frac{B_L(q_i(m))}{B_L(q_i(m_\alpha))}\ . \tag{74}$$

The K-matrix poles α are given by the masses m_α and the partial widths $\tilde{\Gamma}_{\alpha i}$. And c_{ij} is a real and symmetric background constant. For the $(\pi\pi)_S$ wave, K is multiplied by a factor $f = (m^2 - 2m_\pi^2)/m^2$ to characterize the behavior near the $\pi\pi$ threshold.

Following the P-vector approach[60], the dynamical function of resonances, which couples directly to $\bar{p}p$, can be described by

$$\hat{F} = (\mathbf{1} - i\hat{K}\rho)^{-1}\hat{P} \tag{75}$$

while the production vector $\hat{P}$ is defined as

$$\hat{P}_i = \sum_{\alpha} \beta^0_\alpha \frac{\hat{g}_{\alpha i}(m)}{m_\alpha^2 - m^2} \tag{76}$$

The complex parameter β^0_α denotes the complex production strengths of the resonance α (expressed in units of energy). It is convenient to rescale the strength $\beta^0_\alpha = b\beta_\alpha$ with $b^2 = \sum g^2_{\alpha i}$.

If only one pole α couples to a single channel i, eq. (75) becomes the relativistic Breit-Wigner function with the resonance mass $m_0 = m_\alpha$ and the nominal width $\Gamma_0 = \tilde{\Gamma}_{\alpha i}$ (see eq. (55)).

Considering now a resonance coupling to two channels $i = 1, 2$, one obtains the Flatté formula [62]:

$$\hat{F}_i(m) = \frac{\beta^0 \, \hat{g}_i(m)}{m_\alpha^2 - m^2 - i\{\rho_1(m)\,\hat{g}_1^2(m) + \rho_2(m)\,\hat{g}_2^2(m)\}} \tag{77}$$

The ratio R of the squared couplings to the channels $i = 1, 2$ is given by

$$R = \frac{g_1^2}{g_2^2} = \frac{\hat{g}_1^2(m_\alpha)}{\hat{g}_2^2(m_\alpha)} = \frac{\tilde{\Gamma}_{\alpha 1}}{\tilde{\Gamma}_{\alpha 2}} \frac{\rho_2(m_\alpha)}{\rho_1(m_\alpha)} \tag{78}$$

Commonly, resonances are characterized in terms of poles of the analytic scattering matrix $S = \mathbf{1} + 2iT$, respectively of the T-matrix [63] [64] [65]. These poles lay in the complex energy plane and are parameterized by $m_P = m_R - i\Gamma_R/2$. In general the T-matrix and K-matrix poles do not coincide. An exception is the Breit-Wigner function, where the nominal mass and width correspond to the pole parameters m_R and Γ_R of the T-matrix pole.

8.4 Maximum Likelihood Fit

Depending on the number of intermediate states, up to 40 parameters have to be fitted to the selected channels. We refer them as the vector $\vec{\alpha}$. The χ^2 method based on binned data with estimated Poisson errors is not well suited for analyzing the data, since the binning of four independent kinematic variables leaves hardly any entries per bin when employing a reasonable resolution for the measured quantities. The resolution demands typically 50×50 subdivisions of the Dalitz plot and 20×20 of the ω decay angles which correspond to a total of 10^6 bins!

Therefore the extended log-likelihood method is chosen to determine the best values of the free parameters $\vec{\alpha}$ in the weight function w_A. The main part of the likelihood function is the product $\prod_i P_i$ where i runs over all selected events and P_i denotes the probability to observe the single event i. In our case P_i is proportional to w_A and to the detector acceptance ϵ. The extended likelihood function $\mathcal{L}$ is then defined as

$$\mathcal{L}(\vec{\alpha}) = n! \prod_i^n \frac{w(\tau_i, \vec{\alpha})}{\Phi(\vec{\alpha})} \, e^{-(n-\Phi(\vec{\alpha}))^2/2n} \tag{79}$$

with the phase space integral

$$\Phi(\vec{\alpha}) = N_0 \int_{\mathrm{PS}} w(\tau, \vec{\alpha}) \, \epsilon(\tau) \, d\tau \approx \sum_j^m w(\tau_j^{MC}, \vec{\alpha}) \tag{80}$$

which is approximated by the weighted sum over the selected phase space generated Monte Carlo events. The normalization term $e^{-(n-\Phi)^2/2n}$ guarantees that ϕ converges to the number of observed events n. $\epsilon(\tau)$ is the experimental acceptance which we neglect in the numerator as it does not depend on $\vec{\alpha}$.

Before implementing the likelihood function in the fit procedure, one has to consider following points

- High statistic data samples of the order of 100'000 observed and 100'000 Monte Carlo events demand extremely intensive computing (compare eg. [66]). Due to limited resources, the number of calculated weights per iteration has to be cut down to the order of 10'000.
- Combinatorial effects in the reconstruction of the data are visible in the acceptance corrected angular distribution (fig. 24 and 25). Around 8% and 6% of the selected events are wrongly reconstructed.
- Feedthrough background of 10% (7%) has to be taken into account.

8.4.1 High Resolution Binning

To calculate the likelihood function $\mathcal{L}$ for 136023 $\omega\pi^0\pi^0$ and 32059 $\omega\eta\pi^0$ events, respectively, is very expensive in terms of computing. In addition one needs samples of selected Monte Carlo data of the same order of magnitude to calculate Φ. In order to reduce the number of calculations, we choose to evaluate the amplitude function A only in a limited number of bins. Taking advantage of the separability of the transition amplitude (eq. 69), one can achieve a manageable high resolution binning: The number of calculated amplitudes $N_{DP}+N_\omega$ (N_{DP} for Dalitz plot amplitude $\tilde{A}$ and N_ω for the ω decay amplitude H^{111}) corresponds to an effective binning of $N_{bins} = N_{DP} \times N_\omega$. Eg., with $N_{DP} = 1620$ bins for the Dalitz plot amplitude $\tilde{A}$ and $N_\omega = 25 \times 25 = 625$ angular bins for the ω decay, one gets a binning of $N_{bins} = 1'012'500$!

The Dalitz plot variables (s_{13}, s_{23}) contain the information about the three-body kinematics and the ω decay angles (θ, ϕ) about the alignment of its spin. The binning is defined by

$$\text{Event} \longrightarrow \left\{ \begin{array}{lll} a = 1, ..., N_{DP} & \longrightarrow & \{s_{13}, s_{23}\}_a \\ b = 1, ..., N_\omega & \longrightarrow & \{\cos\theta, \phi\}_b \end{array} \right. \tag{81}$$

and ensures that the bins are equally populated by phase space distributed events. Each Dalitz plot bin $\{s_{13}, s_{23}\}_a$ can be transformed unequivocally into each of the three combinatorial sequence (i) of rotation angles $\{\theta_0^{(i)}, \theta_R^{(i)}, \theta_{(i)1}\}_a$ needed to calculate the angular part of $\tilde{A}$. The weight of the event laying in the bins a and b can then be expressed in the binned form as

$$w_A(a,b) = \sum_{J^{PC}}^{\text{initial}} \text{Tr}\left\{ \left(A^{J^{PC}}(a,b)\right) \frac{\mathbf{1}}{2J+1} \left(A^{J^{PC}}(a,b)\right)^{\dagger} \right\} \tag{82}$$

where

$$A^{J^{PC}}(a,b) = H_{10}^{111}(b) \sum_{i}^{\text{chains}} \alpha_i \tilde{A}_i^{J^{PC}}(a) \tag{83}$$

For each bin b, the 3×2 matrix $H_{10}^{111}(b)$ is calculated once at beginning of the fit procedure and stored in the RAM. During the iteration process, only the arrays containing $\tilde{A}_i^{J^{PC}}(a)$ $(a=1,...N_{DP})$ have to be updated, – compared to the event-by-event calculation an enormous reduction. The angular part of $\tilde{A}_i$ – a real 3×3 matrix – is also calculated and stored for each chain i and bin a in an array at the beginning of the fit.

In addition, the binning of the dynamical part of $\tilde{A}_i$ is subdivided into 3×3 bins, in order to enhance the resolution to about $\Delta s = 13'700$ MeV^2 which corresponds to an maximum energy binning $\Delta_{\sqrt{s}} = 7.5$ MeV at the threshold $s = (m_\pi + m_\omega)^2$. This is significant below the resolution[5] of the detector determined by Monte Carlo data (section 5.3). Furthermore, to save computing time, the dynamical part $F_R^L(s)$ is computed separately in equal steps of the variable s. Instead of calculating the dynamics for all $9\times N_{DP}$ Dalitz plot bins individually, it is sufficient to evaluate the function for a couple of hundred selected bins of the mass projection and to map them to the full Dalitz plot binning:

$$a \;\longrightarrow\; \{s_{13}, s_{23}\}_a \longrightarrow \{s^{(i)}\}_a\ , \quad i = 12, 13, 23 \tag{84}$$

where i denotes one of the three invariant mass systems.

This binning method for partial wave analysis allows to perform the fits in reasonable time and accuracy. For 300'000 events and 30 free fitted parameters including dynamical parameters and two initial states, the fitting program written in FORTRAN and based on the MINUIT package [42] needs about 80 MByte RAM and converges after 10'000 to 25'000 iteration steps, corresponding to about 24 hours computing time on a Digital Alpha Station 600 5/333 (300 MHz). It is the first time in the Crystal Barrel Collaboration that as many events (310'000) are processed in a maximum log-likelihood fit. Refining the presented technique, one could perform simultaneously fits of several high statistics final states containing the same resonances (coupled channel fits).

---

[5] A uniformly populated bin width of Δ corresponds to a standard deviation of $\sigma = \Delta/\sqrt{12}$

8.4.2 Combinatorial Reconstruction

Events can be reconstructed kinematically far away from their generation point owing to combinatorial effects described in section 5.4. Figure 31 and the angular distributions (fig. 24) show that this has to be taken into account. In order to reproduce the reconstruction correctly one has to adjust the weight function:

$$w(\tau) \to w'(\tau) = c(\tau)w(\tau) \tag{85}$$

where $c(\tau)$ describes the change of the observation probability for a event τ due to combinatorics. The weight function $w'(\tau)$ can be expressed by the phase space integration

$$w'(\tau) = \frac{\int_{\mathrm{PS}} \delta(\tau, x)\, w(x')\, \epsilon(x')\, dx'}{\int_{\mathrm{PS}} \delta(\tau, x)\, \epsilon(x')\, dx'} \tag{86}$$

where x denotes the reconstructed event associated to the true event x' and ϵ the detector acceptance.

In good approximation, $c(\tau)$ can be derived from Monte Carlo data substituting the integral be a sum and taking into account only the Dalitz plot coordinates:

$$c(a) \approx \frac{\sum_j^{MC} \chi_a(\tau_j)\, w(\tau_j^{gen})}{\sum_j^{MC} \chi_a(\tau_j)\, w(\tau_j)} \tag{87}$$

τ_j^{gen} is the generated and τ_j the reconstructed event. χ_a is given by

$$\chi_a(\tau) = \begin{cases} 1 & \text{if } \tau \text{ belongs to Dalitz plot bin } a \\ 0 & \text{otherwise.} \end{cases} \tag{88}$$

The results of the partial wave analysis described below show that the correction suffices to reproduce the angular distribution.

8.4.3 Feedthrough Background

A general problem for the Maximum Likelihood method is the treatment of the background. Usually, the knowledge on the background is based on Monte Carlo simulations or on samples of pure feedthrough events. If one succeeds to parameterize the background weight w_{BG}, one can modify the weight function $w \to w + w_{BG}$. Another method consists in taking into account the background by rescaling the likelihood function with the likelihood for feedthrough events [67]. A sample of n'_{BG} events are assumed to be representative for the distribution of the $n_{BG} = f\, n'_{BG}$ real background events in the selection. Then the modified likelihood function is defined as

$$\mathcal{L}(\vec{\alpha}) \longrightarrow \mathcal{L}'(\vec{\alpha}) = \frac{\mathcal{L}(\vec{\alpha})}{\mathcal{L}_{BG}(\vec{\alpha})} \tag{89}$$

while

$$\mathcal{L}_{BG}(\vec{\alpha}) = n'_{BG}! \prod_{i}^{n'_{BG}} \frac{w(\tau_i^{BG}, \vec{\alpha})^f}{\Phi(\vec{\alpha})^f} \; . \tag{90}$$

The dependence of the likelihood function on the fit parameters will be reduced for events in regions with high background contribution. The factor f has to be determined previously and cannot be fitted.

8.4.4 Fit Procedure

The parameter are fitted to the data by minimizing the negative log-likelihood function (NLL$=-\log\mathcal{L}$) with the MINUIT package [42]. Taking into account the correction discussed above, the NLL is given by

$$\begin{aligned} \log\mathcal{L} \;=\; C \;&+\; \sum_i^n \log w'(a_i, b_i) \;-\; f \sum_i^{n'_{BG}} \log w'(a_i^{BG}, b_i^{BG}) \\ &-\; (n - f n'_{BG}) \log\Phi \;-\; \frac{n}{2}\,(1 - \Phi/n)^2 \end{aligned} \tag{91}$$

while

$$\Phi = \sum_i^{\mathrm{MC}} w'(a_i^{MC}, b_i^{MC}) \tag{92}$$

and the corrected weight

$$w'(a,b) = c(a)\; w(a,b) \; . \tag{93}$$

The additional constant C absorbs any factor of the likelihood functions which does not depend on $\vec{\alpha}$.

The standard error on NLL is 0.5. A significant improvement in NLL should exceed at least 0.5 for each (additional) parameter. In reality, errors have to be increased somewhat. The weight function contains systematic deviation from the "real" weight due for example to the finite resolution of the measurement.

In order to have an estimate for the goodness of the fit, the theoretical and measured Dalitz plot are compared by

$$\chi^2 = \sum_a^{\text{bins}} \frac{(n_a - t_a)^2}{{\sigma_a}^2} \, . \tag{94}$$

where n_a is the measured number of entries in bin a and t_a the expected number of events determined by m_a weighted and reconstructed Monte Carlo events. The error is estimated by

$$\sigma_a^2 \approx n_a + \frac{t_a^2}{m_a} \tag{95}$$

The aim of the fit procedure is to find a hypothesis for the decay chains which provides a satisfactory description of the data within the experimental uncertainties. In the first attempt one tries to find a hypothesis with established resonances. If the hypothesis has to be extended with new states, we consider following criteria

- significant improvement in NLL and χ^2
- convergence of free fitted mass and width of the state
- relative stability of the fitted parameters with respect to further extension of the hypothesis.

8.5 Fit Results of $\overline{p}p \rightarrow \omega\pi^0\pi^0$

The data are fitted using the $4\pi^0$ Monte Carlo simulation for the background corrected likelihood function (see eq. 89). The phase space is divided into $N_{DP} = 9 \times 1145$ Dalitz plot bins with the size $\Delta m^2_{\omega\pi} = 12'600\,\mathrm{MeV}^2$ and $N_\omega = 25 \times 25$ angular bins for the ω decay with the size $\Delta\phi = 14.4\,^\circ$ and $\Delta\cos\theta = 0.08$. The resonances considered in the partial wave analysis are listed in table 15, fulfilling the conservation law restrictions given in table 4 (sec. 3).

Initial state	L	S	Resonance	l	s	F1	F2	F3	F3'	F4
${}^3S_1\rightarrow (\pi\pi)_S\omega$	0	1	$(\pi\pi)_S\rightarrow\pi^0\pi^0$	0	0	x	x	x	x	x
	2	1				x	x	x	x	x
${}^3S_1\rightarrow b_1(1235)\pi^0$	0	1	$b_1\rightarrow \omega\pi^0$	0,2	1	x	x	x	x	x
	2	1				x	x	x	x	x
${}^3S_1\rightarrow f_2(1270)\omega$	0	1	$f_2\rightarrow\pi^0\pi^0$	2	0	x	x	x	x	x
	2	1,2,3								x
${}^3S_1\rightarrow \rho(1450)\pi^0$	1	1	$\rho\rightarrow \omega\pi^0$	1	1		x		x	
${}^3S_1\rightarrow \rho(1700)\pi^0$	1	1	$\rho\rightarrow \omega\pi^0$	1	1					x
${}^1P_1\rightarrow (\pi\pi)_S\omega$	1	1	$(\pi\pi)_S\rightarrow\pi^0\pi^0$	0	0			x	x	x
${}^1P_1\rightarrow f_2(1270)\omega$	1	1,2	$f_2\rightarrow\pi^0\pi^0$	2	0			x	x	x
${}^1P_1\rightarrow b_1(1235)\pi^0$	1	1	$b_1\rightarrow \omega\pi^0$	0,2	1			x	x	x

Table 15: *Decay chains of* $\overline{p}p \rightarrow \omega\pi^0\pi^0$ *considered in this analysis.*

Three types of hypothesis are tested: (1) $\bar{p}p$ annihilation from the ${}^3S_1$ initial state including the b_1, the $(\pi\pi)_S$ wave and the f_2, in the following referred to as the basic fit; (2) further resonances (eg. $\rho(1450) \rightarrow \omega\pi^0$) contributing from ${}^3S_1$; and (3) contribution from ${}^1P_1$ initial state.

In order to give a representative selection of the fit hypotheses tested in this work we report following four fits: Fit $\mathcal{F}1$ – the basic fit – is performed with PDG mass and width for the $b_1(1235)$ and the $f_2(1270)$ including the $(\pi\pi)_S$ wave, the dipion S-wave, and a parameter for additional phase space distributed background in the signal. In fit $\mathcal{F}2$ a vector resonance $\rho(1450)$ decaying into $\omega\pi^0$ is added. The mass of the vector meson and of the $b_1(1235)$ are released in the fit as well as the width of the b_1. Fit $\mathcal{F}3$, instead of the vector meson, allows meson production from ${}^1P_1$ initial state. Finally, fit $\mathcal{F}4$ combines the hypothesis of $\mathcal{F}2$ and $\mathcal{F}3$.

In all four fits, the ratio D/S of D-wave to S-wave amplitude for $b_1 \rightarrow \omega\pi^0$ (see eq. (63)) is left free and the $(\pi\pi)_S$-wave is described by a 3×3 K-matrix including the coupling to $\pi\pi$, $\eta\eta$ and $K\overline{K}$, using the pole positions of the σ, $f_0(980)$ and

$f_0(1370)$ and a non-resonant background constant from the coupled channel analysis of ref. [25, 69]. Only the complex production strengths of the three resonances are left free in the fit. The K-matrix parameters are listed in table 16.

pole α	m_α [MeV/c^2]	$\tilde{\Gamma}_{\alpha,\pi\pi}$ [MeV/c^2]	$\tilde{\Gamma}_{\alpha,\eta\eta}$ [MeV/c^2]	$\tilde{\Gamma}_{\alpha,\overline{K}K}$ [MeV/c^2]
1	841.3	666.7		
2	1240.8	3.1	13.0	315.7
3	1169.4	691.4	21.5	
background	$c(\pi\pi,\overline{K}K) = 1.082$			

Table 16: *K-matrix poles of the $(\pi\pi)_S$ wave from ref. [70]*

The fitted complex couplings $\alpha_i = a_i e^{i\phi}$ for the various fits are given in table 17 and are normalized to the phase space integral of the intensity of the amplitude they refer to. The dynamical parameters (masses and widths) as well as the production strengths of the $(\pi\pi)_S$ wave are listed in table 18. We define the branching ratios relative to $\omega\pi^0\pi^0$, as the sum of contributing amplitudes squared $\mid \alpha_i A_i \mid^2$, integrated over phase spase and normalized to the integral of the total coherent intensity $\mid \sum_i \alpha_i A_i \mid^2$, neglecting interference. These contribution are listed separately for each resonance and each initial state in the upper part of table 19, while in the lower part the contribution are summed over the initial states and normalized to a total sum of 100%.

The basic hypothesis gives a satisfactoy description of data. The good agreement of the fit and the data are shown in figure 40 and for the angular distribution of the ω decay in figure 41. The $\mathcal{F}1$ leads to a $D/S = 0.203 \pm 0.014$ compatible with the PDG value D/S=0.29±0.04 [8] and to an additional background contribution of $0.32 \pm 0.02\%$ which is negligible and shows that most of the intensity in the signal is covered. Nevertheless the χ^2 distribution shows some enhancement at the crossing of the b_1 bands. The fit improves with a released mass and width of the b_1. The mass, however, converges to a low value around 1215 MeV, while the D/S drops to the proximity of zero – in disagreement to the PDG value.

In fit $\mathcal{F}2$, the included $\rho(1450)$ with free mass and fixed width (300 MeV) converges at a mass of 1275±4 MeVwhile the b_1 drops to 1216±1 MeV with a pure $D/S = 0.02 \pm 0.01$. The width diverges if released in the fit towards an unphysically large value. Despite of the agreement with the observed $\rho(1250)$ [8], the state is rather an effect of the incomplete description of the final state. The inclusion of the $^1P_1$ initial state makes the $\rho(1275)$ superfluous. Fit $\mathcal{F}3$ displays a large improvement

Fit		$\mathcal{F}1$	$\mathcal{F}2$	$\mathcal{F}3$	$\mathcal{F}4$
2 NLL-2.88 $\times 10^6$		9959.1	8968.4	8589.6	8216.9
N_{par}		17	23	30	40
χ^2/dof, $dof = 1145 - N_{par}$		1.320	1.185	1.158	1.081
${}^3S_1 \to b_1\pi^0$	$a_1(L=0)$	.427±.008	.376±.005	.326±.007	.421±.006
	$a_2(L=2)$	.384±.009	.380±.004	.301±.009	.238±.006
	$\phi_2(L=2)$	.469±.031	.376±.031	.653±.040	.269±.031
	D/S	.203±.014	.066±.010	.126±.018	.195±.020
	$\phi(D/S)$	-.389±.010	(0.0)	-.486±.180	-1.31±.056
${}^3S_1 \to (\pi\pi)_S\omega$	$a_1(L=0)$	.493±.008	.546±.005	.457±.010	.551±.014
	$a_2(L=2)$	.327±.007	.253±.008	.230±.018	.266±.007
	$\phi_1(L=0)$	-1.36±.021	-1.06±.024	-1.06±.030	-1.58±.030
	$\phi_2(L=2)$	-.413±.021	.095±.020	0.668±.061	.093±.014
${}^3S_1 \to f_2\omega$	$a_1(L=0)$	.437±.006	.425±.005	.315±.010	.259±.007
	$a_2(L=2,S=1)$				.071±.008
	$a_2(L=2,S=2)$				.074±.006
	$a_2(L=2,S=3)$				.154±.008
	$\phi_1(L=0)$	-.597±0.064	-.318±.031	-.446±.061	-.914±.046
	$\phi_2(L=2,S=1)$				-4.55±.100
	$\phi_2(L=2,S=2)$				-3.42±.125
	$\phi_2(L=2,S=3)$				-3.50±.050
${}^3S_1 \to \rho\pi^0$	$a_1(L=0)$		.109±.004		.202±.017
	$\phi_1(L=0)$		1.07±.029		1.63±.060
${}^1P_1 \to b_1\pi^0$	$a_1(L=1)$			.403±.073	.366±.006
${}^1P_1 \to (\pi\pi)_S\omega$	$a_1(L=1)$			.351±.009	.386±.008
	$\phi_1(L=0)$			-.990±.045	1.88±.040
${}^1P_1 \to f_2\omega$	$a_1(L=1)$			.141±.010	.167±.007
	$\phi_1(L=0)$			.380±.100	3.48±.070
Background	PS	.32±.02%			

Table 17: *Fitted couplings* $\alpha_i = a\,e^{i\phi}$ *of* $\omega\pi^0\pi^0$ *(see text).*

Fit		$\mathcal{F}1$	$\mathcal{F}2$	$\mathcal{F}3$	$\mathcal{F}4$
b_1	m	1229.5 (PDG)	1215.9±.7	1226.1±1.0	1237.6±.66
	Γ	142.0 (PDG)	140.6±1.4	143.6±1.8	148.1±2.2
ρ	m		1275.4±4.9		1737.5±.31
	Γ		300.		327.3±62.6
$(\pi\pi)_S$ $(L=0)$	b_2	60.7±.8	50.2±.5	68.3±1.25	60.7±1.05
$(b_1=15.108)$	b_3	24.4±.4	18.9±.1	30.7±.41	30.3±.637
	ϕ_2	.220±.011	.116±.007	.085±.020	.026±.014
	ϕ_3	.078±.013	.378±.009	.086±.021	.093±.013
$(\pi\pi)_S(L=1)$	b_2			40.2±1.63	41.4±1.33
$(b_1=15.108)$	b_3			11.3±0.42	12.7±.070
	ϕ_2			.236±.040	.115±.039
	ϕ_3			.108±.066	.059±.025
$(\pi\pi)_S(L=2)$	b_2	60.7±.8	90.7±1.37	88.0±4.3	44.4±3.69
$(b_1=15.108)$	b_3	24.4±.4	30.7±0.73	31.2±2.2	41.9±2.10
	ϕ_2	.220±.011	.142±.018	-.384±.031	-.233±.052
	ϕ_3	.078±.013	-.085±.019	5.19±.053	4.57±.114

Table 18: *Fitted dynamical parameters of* $\omega\pi^0\pi^0$ *(see text)*

Fit	$\mathcal{F}1$	$\mathcal{F}2$	$\mathcal{F}3$	$\mathcal{F}4$
${}^3S_1 \to b_1\pi^0$	35.9%	29.5%	20.5 %	24.7 %
${}^3S_1 \to (\pi\pi)_S\omega$	35.2%	36.3%	26.2 %	37.6 %
${}^3S_1 \to f_2\omega$	19.1%	18.1%	9.9 %	10.2 %
${}^3S_1 \to \rho\pi^0$		1.2%		4.1 %
$\sum {}^3S_1$	90.1%	90.3%	54.3 %	54.6 %
${}^1P_1 \to b_1\pi^0$			16.5 %	13.8 %
${}^1P_1 \to (\pi\pi)_S\omega$			12.3 %	14.9 %
${}^1P_1 \to f_2\omega$			2.0 %	2.8 %
$\sum {}^1P_1$			35.5 %	35.2 %
background	9.9%	9.6%	9.6 %	9.6%
Signal				
$b_1\pi^0$	39.7±2.0 %	34.7±1.7 %	42.3±2.1 %	38.0±1.9 %
$(\pi\pi)_S\omega$	39.1±2.0 %	42.7±2.1 %	44.0±2.2 %	45.0±2.3 %
$f_2\omega$	21.2±1.1 %	21.3±1.1 %	13.7±0.7 %	12.9±0.6 %
$\rho\pi^0$		1.4±0.12 %		4.0±0.6 %

Table 19: *Contributions of* $\omega\pi^0\pi^0$ *(see text).*

in NLL and χ^2 due to the inclusion of ${}^1P_1$ (39.5,%, see tab. 19), whereas the extension of the hypothesis with a low mass $\rho(1450)$ does not lead to stable solutions. Scans with fixed ρ mass and width exhibit some improvements in NLL and χ^2 but in so far as the resonances cannot be attributed to stable dynamical solutions we do not claim any evidence. Table 20 shows such a scan for $\rho(1450)$ as an extension of fit $\mathcal{F}3$. The best result is reached at row 5 for a contribution of 0.7 %, but with a large error of 0.3 % determined from the NLL increase of one standard error.

$\mathcal{F}3'.i$	$B(\rho)[\%]$	$2NLL$	χ^2	D/S	m_{b_1}	Γ_{b_1}
1	.00	8589.6	1.158	.126±.018	1226.1±1.0	143.6±1.8
2	.044	8533.2	1.148	.124±.015	1226.2±0.7	142.3±1.4
3	.175	8510.0	1.142	.130±.018	1226.1±0.7	141.5±1.4
4	.394	8498.0	1.137	.132±.017	1225.9±1.0	141.2±1.8
5	.701	8496.5	1.134	.132±.024	1225.4±1.1	141.3±2.1
6	1.09	8504.3	1.134	.131±.016	1224.8±0.7	141.8±1.3
7	1.58	8500.0	1.168	.191±.020	1223.9±0.6	147.0±1.2
8	2.15	8506.0	1.171	.187±.024	1223.5±0.9	146.8±1.5
9	2.81	8520.2	1.175	.181±.017	1223.1±0.5	146.5±1.1

Table 20: *Scan of* $\rho(1450)$ *contribution in* $\omega\pi^0\pi^0$. *Mass and width of* $\rho(1450)$ *are fixed to the values* $m = 1450$ MeV, $\Gamma = 300$ MeV.

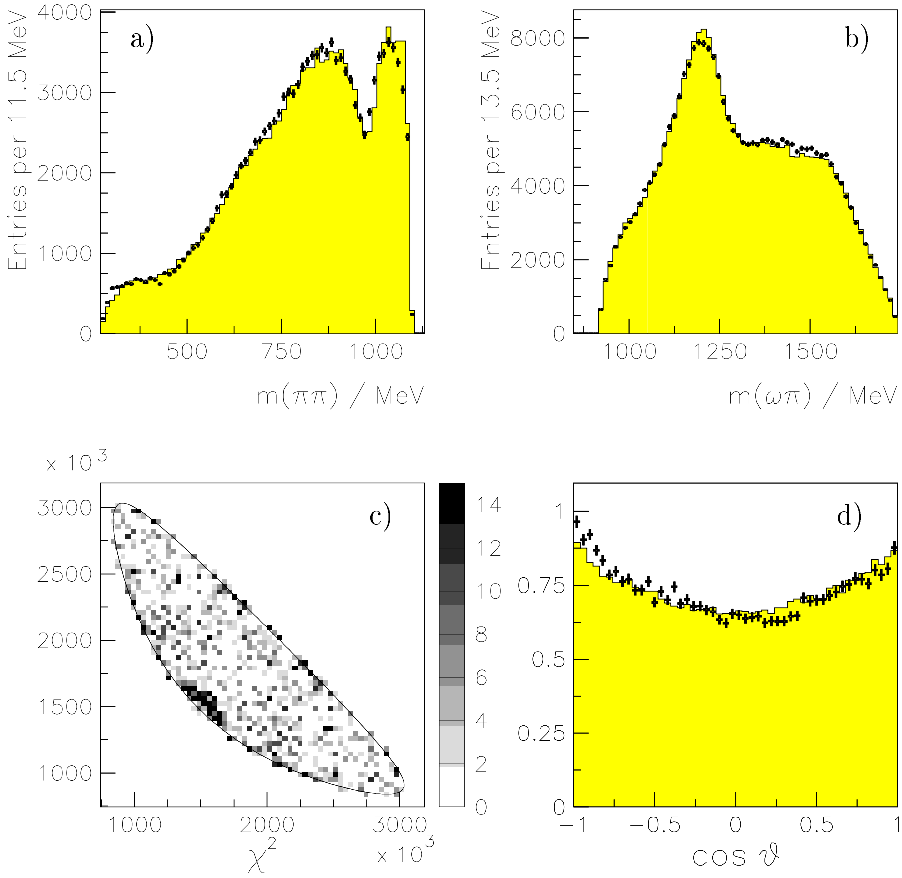

Figure 40: *Result of the fit $\mathcal{F}1$ for $\omega\pi^0\pi^0$: (a),(b) the $\pi^0\pi^0$ and $\omega\pi^0$ mass spectra; (c) the χ^2 distribution and (d) the $\cos\theta$ distribution*

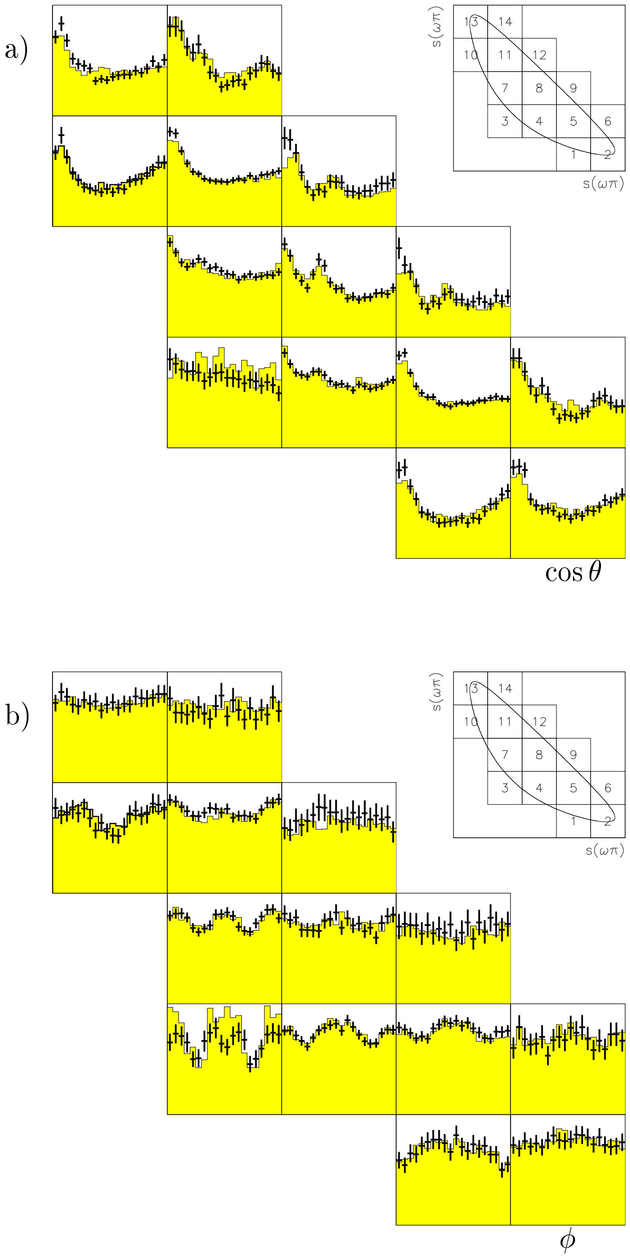

Figure 41: *(a) the* $\cos\theta$ *and (b) the* ϕ *distribution of fit* $\mathcal{F}1$

We get the best results by introducing a high mass $\rho(1700)$. Fit $\mathcal{F}4$ leads to a stable solution for a ρ at

$$m_\rho = 1738 \pm 1 \text{ MeV} \quad \text{and} \quad \Gamma_\rho = 327 \pm 63 \text{ MeV} \tag{96}$$

This state agrees well with the PDG values for $\rho(1700)$ (1723±11 MeV and 240±40 MeV). The χ^2 distribution displays no significant structures and the fitted angular distributions agree perfectly with the data (fig. 42 and 43). In order to enhance the sensitivity of the fit a scan for the D/S is performed (see tab. 21). The mass does not depend on D/S, whereas the width of the particle appears to be stable only up to a ratio of 0.25.

From fit $\mathcal{F}4$ one finds the mass and the width of the b_1 at

$$m_{b_1} = 1238 \pm 1 \text{ MeV} \quad \text{and} \quad \Gamma_{b_1} = 148 \pm 3 \text{ MeV} \tag{97}$$

and a ratio of

$$D/S = 0.20 \pm 0.02_{stat} \tag{98}$$

as well as a phase difference of $\Delta\phi = \phi_D - \phi_S =$ -1.31±0.06 (74.5±3.7°).

All attempts to describe the data with a two pole K-matrix parametrization for the $(\omega\pi)_P$ wave fail. Neither the pole structure $\rho(770, 1450)$ nor $\rho(770, 1700)$ nor $\rho(1450, 1700)$ result in stable parameters. Though χ^2 and NLL seem to favor such contributions, we can not draw definitive conclusions. The same occurs for an axial vector state at higher mass. Due to the uncertainties in the parameterization of these vector resonances we do not give upper limits for $\rho(770)$ and $\rho(1450)$.

$\mathcal{F}4.i$	D/S	$2NLL$	χ^2	m_{b_1}	Γ_{b_1}	m_ρ	Γ_ρ
1	0.00	8273.1	1.087	1235.2±1.4	144.5±2.0	1739.8±0.2	374.7±27.7
2	0.10	8231.7	1.083	1235.9±0.9	147.0±2.6	1738.3±0.7	300.64±50.3
3	0.20	8216.6	1.081	1238.0±0.6	147.5±1.8	1738.8±0.2	352.9±30.4
4	0.25	8221.2	1.083	1238.4±1.3	145.8±2.1	1738.8±1.0	470.1±21.7
5	0.30	8192.8	1.074	1236.4±1.2	140.1±2.1	1730.0±0.9	2352.5±184.2
6	0.40	8227.1	1.075	1236.9±0.8	141.4±1.5	1736.2±0.7	2389.9±140.5

Table 21: *Scan of D/S in fit $\mathcal{F}4$'*

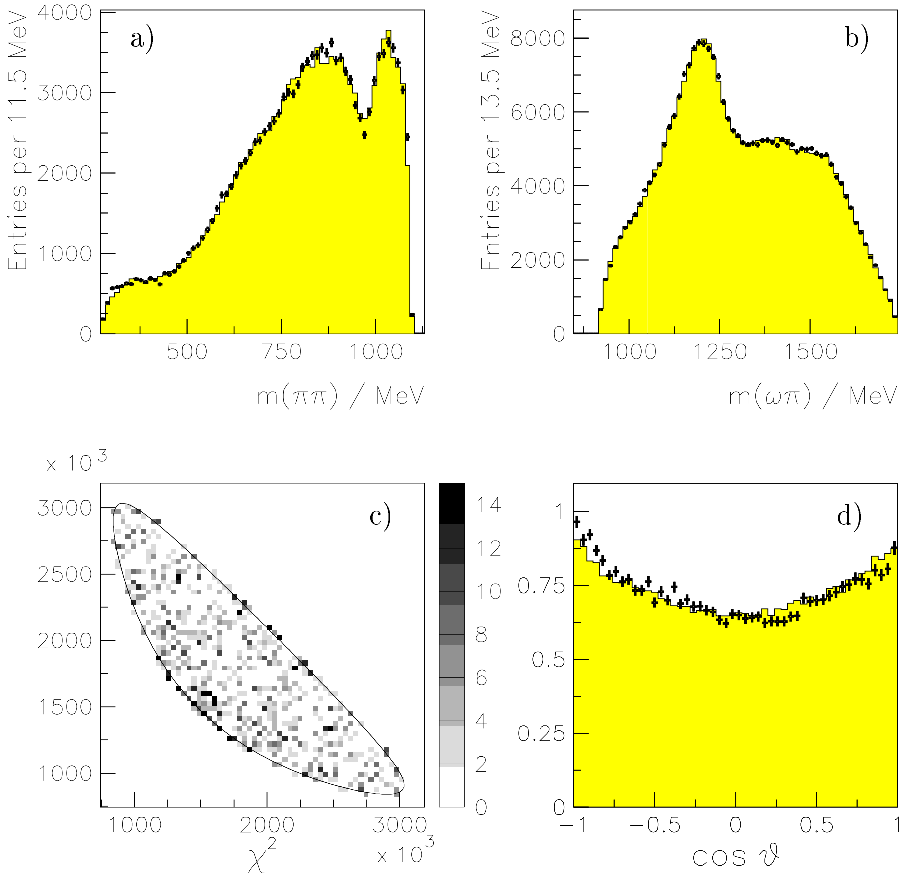

Figure 42: *Result of the fit $\mathcal{F}4$ for $\omega\pi^0\pi^0$: (a),(b) the $\pi^0\pi^0$ and $\omega\pi^0$ mass spectra; (c) the χ^2 distribution and (d) the $\cos\theta$ distribution*

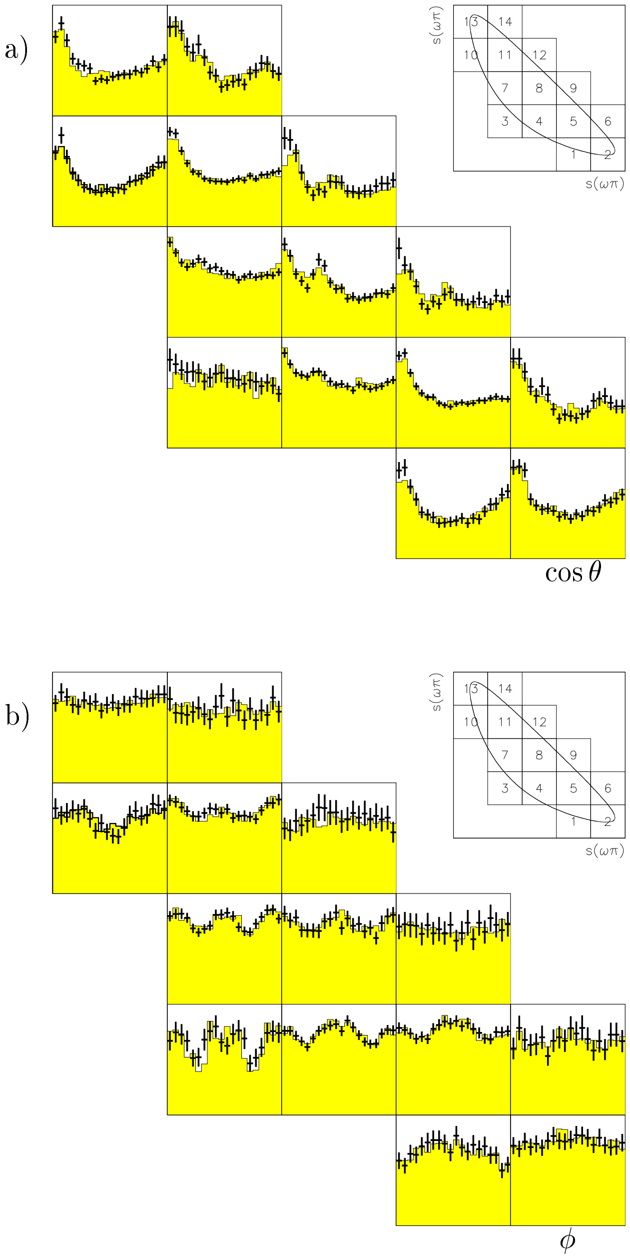

Figure 43: *(a) the* $\cos\theta$ *and (b) the* ϕ *distribution of fit* $\mathcal{F}4$

8.6 Fit Results of $\overline{p}p \rightarrow \omega\eta\pi^0$

For the analysis of the $\omega\eta\pi^0$ final state background is assumed to be phase space distributed (see sec. 6) and is taken into account by adding a constant w_{BG} to the weight function $w(\Omega) \rightarrow w(\Omega) + w_{BG}$. Since the background cannot be attributed to a single feedthrough channel, we do not use Monte Carlo Simulation. The Dalitz plot consists of $N_{DP} = 9 \times 1156$ bins with the size of $\Delta m^2_{\omega\eta} = 5'100\,\mathrm{MeV}^2$ and $\Delta m^2_{\omega\pi} = 7'800\,\mathrm{MeV}^2$, the angular distribution of $N_\omega = 25 \times 25$ bins and a resolution of $\Delta\phi = 14.4\,^\circ$ and $\Delta\cos\theta = 0.08$. The resonances considered in the partial wave analysis are listed in table 22.

Initial state	L	S	Resonance	l	s	F1	F2	F3	F3'	F4
${}^3S_1 \rightarrow a_0(980)\omega$	0	1	$a_0 \rightarrow \eta\pi^0$	0	0	x				
${}^3S_1 \rightarrow (\eta\pi)_S\omega$	0	1	$a_0 \rightarrow \eta\pi^0$	0	0		x	x	x	x
	2	1					x	x	x	x
${}^3S_1 \rightarrow a_2(1320)\omega$	0	1	$a_2 \rightarrow \eta\pi^0$	2	0	x	x	x	x	x
	2	1,2,3							x	
${}^3S_1 \rightarrow b_1(1235)\eta$	0	1	$b_1 \rightarrow \omega\pi^0$	0,2	1	x	x	x	x	x
	2	1				x	x	x	x	x
${}^3S_1 \rightarrow h_1'(1380)\pi^0$	0	1	$h_1' \rightarrow \omega\eta$	0	1		x	x	x	x
${}^3S_1 \rightarrow \omega(1420)\pi^0$	1	1	$\omega \rightarrow \omega\eta$	1	1					x
${}^3S_1 \rightarrow \omega(1600)\pi^0$	1	1	$\omega \rightarrow \omega\eta$	1	1			x	x	x
${}^1P_1 \rightarrow (\eta\pi)_S\omega$	1	1	$a_0 \rightarrow \eta\pi^0$	0	0			x	x	x
${}^1P_1 \rightarrow \omega(1420)\pi^0$	0	1	$\omega \rightarrow \omega\eta$	1	1					x
${}^1P_1 \rightarrow \omega(1600)\pi^0$	0	1	$\omega \rightarrow \omega\eta$	1	1			x	x	x

Table 22: *Decay chains of* $\overline{p}p \rightarrow \omega\eta\pi^0$ *considered in this analysis.*

The basic fit, referred to as $\mathcal{F}1$, contains the $a_0(980)$, the $b_1(1235)$ and the $a_2(1320)$. All three states are described by Breit-Wigner amplitudes. The mass and width of the a_2 and the b_1 are fixed to the PDG values [8]: 1318 and 1229.5 MeV, 107 and 142 MeV, respectively, while the mass and width of the $a_0(980)$, left free in the fit, converge to $m = 984.7 \pm 0.6$ MeV and $\Gamma = 65.3 \pm 2.1$ MeV in good agreement with PDG. However, this fit clearly fails to describe the data. The $\omega\eta$ mass distribution plotted in figure 44b displays a depletion around 1400 MeV and an enhancement at 1700 MeV also visible in the plots showing the relative difference of the measured and fitted Dalitz plots 44c,d. Furthermore, the $\cos\theta$ distributions shown in figure 45 are badly described.

Four hypotheses are considered in order to improve the description: (1) the 2×2 K-matrix parametrisation for $(\eta\pi)_S$ including the coupling to $\eta\pi$ and $K\overline{K}$, a pole

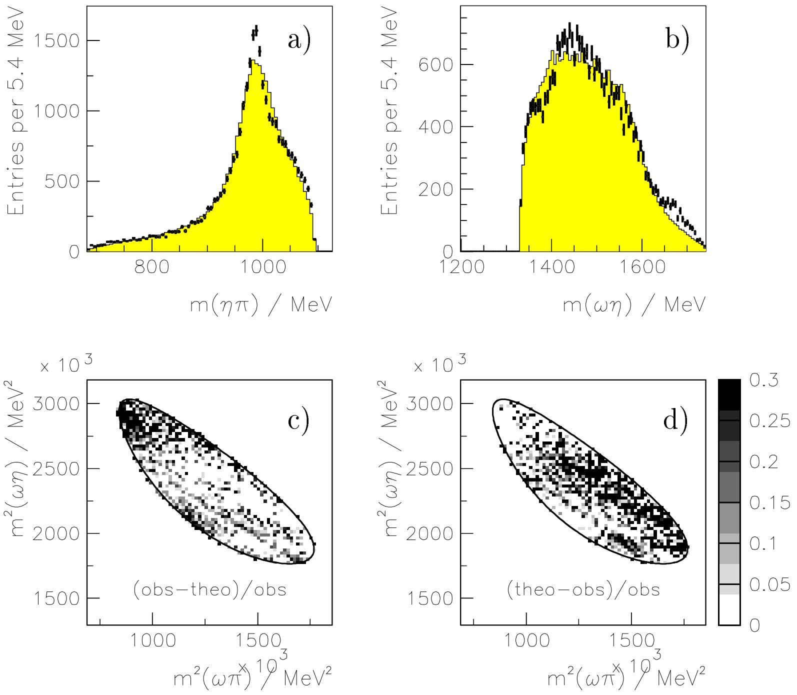

Figure 44: *Result of the fit $\mathcal{F}1$: (a,b) show the measurement (error bars) and the fit (solid line) of the invariant mass spectra $m(\eta,\pi)$ and $m(\omega\eta)$; and (c,d) the relative difference between measured and fitted Dalitz plot in $m^2(\omega\eta)$ vs $m^2(\omega\pi)$.*

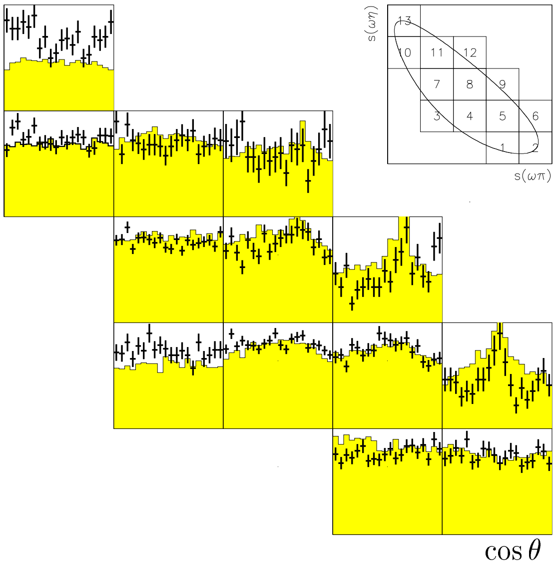

Figure 45: $\cos\theta$ *distribution of fit $\mathcal{F}1$*

for $a_0(980)$ and for $a_0(1450)$. (2) An axial vector (h_1) state decaying into $\omega\eta$. (3) A vector state (ω) decaying into $\omega\eta$ and (4) contribution from ${}^1P_1$ initial state.

This hypotheses are tested in following fits: In fit $\mathcal{F}2$ the $\eta\pi$ wave and an axial vector h_1 is included. Fit $\mathcal{F}3$ contains besides the ingredience of $\mathcal{F}2$ a vector meson decaying into $\omega\eta$ and includes ${}^1P_1$ initial state. Fit $\mathcal{F}3$' takes into account the $L = 2$ production of a_2 which may explain the intensity fluctuation along the $a_0(980)$. In fit $\mathcal{F}4$ a two pole solution for the $(\omega\eta)_P$ is tested.

For the $(\eta\pi)_S$ wave the K-matrix mass and partial width of the second pole are taken from the analysis of ref.[25, 70] whose K-matrix poles are given in table 23. The background weight w_{BG} is normalized to 6.9% of the total intensity of the signal. The $b_1(1235)$ mass is not fitted since the contribution of the resonance is small. The parameters of the various fits are given in table 24 (coupling parameters) and in table 25 (dynamical parameters). The contributions are calculated according to the method described in sec. 8.5 and listed in table 26.

pole α	m_α [MeV/c^2]	$\tilde{\Gamma}_{\alpha,\eta\pi}$ [MeV/c^2]	$\tilde{\Gamma}_{\alpha,K\overline{K}}$ [MeV/c^2]
1	995.4	92	0.8
2	1503.5	17.5	207.5

Table 23: K-matrix poles of the $(\pi\eta)_S$ wave from ref.[70]

Extending the basic fit, the description of the data can be improved considerably by including an axial vector state at 1400 MeV and by using a two pole 2×2 K-matrix for the $(\pi\eta)_S$ wave. In this analysis all parameters of the first pole are fitted while for the second pole only the coupling to $\bar{p}p$ β_2 is left free since the second pole is outside of phase space.

In a first attempt the axial vector is parametrized by a Breit-Wigner amplitude which converges to a mass of 1377.3±2.8 MeV and a width of 30.4±4.3 MeV. It interferes destructively with the $a_0(980)$ and contributes to the final state in the order of 1 %. This state may be the missing axial vector isosinglet and may correspond to a state observed in the $K\overline{K}^*$ decay mode at 1380 MeV [10] and at 1440 MeV [11], respectively. The latter possibility is investigated by a Flatté amplitude coupling to the $\omega\eta$ and to the $K\overline{K}^*$ channel which opens at around 1385 MeV, near the resonance maximum. The fitted couplings in $\mathcal{F}2$ shows that the Flatté form is indeed preferred to the Breit-Wigner (single coupling) and corresponds to a relative coupling of $g^2_{\omega\eta}/g^2_{K\overline{K}^*} = 1.4 \pm 0.5$. The mass distribution and the relative differences between

Fit		$\mathcal{F}1$	$\mathcal{F}2$	$\mathcal{F}3$	$\mathcal{F}3'$	$\mathcal{F}4$
2 NLL		691'637.7	691'024.1	690'789.2	690'742.4	690'736.6
N_{par}		12	22	29	36	36
χ^2/dof, $dof = 1156$		1.554	1.252	1.107	1.073	1.064
${}^3S_1 \to (\pi\eta)_S\omega$	$a_1(L=0)$	.735±.015	.876±.014	.883±.010	.896±.009	.862±.014
	$a_2(L=2)$		.255±.021	.088±.039	.221±.047	.157±.037
	$\phi_2(L=0)$		1.55±.056	4.65±0.14	4.25±0.20	4.73±0.10
${}^3S_1 \to a_2\omega$	$a_1(L=0)$	.498±.024	.299±.014	.271±.014	.269±.014	.251±.024
	$\phi_1(L=0)$	1.85±0.04	1.32±.074	1.39±0.07	1.41±0.07	1.36±0.13
	$a_2(2, S=1)$				.076±.022	
	$a_2(2, S=2)$				.053±.011	
	$a_2(2, S=3)$				.062±.009	
	$\phi_2(2, S=1)$				2.69±0.20	
	$\phi_2(2, S=2)$				4.20±0.27	
	$\phi_2(2, S=3)$				5.67±0.23	
${}^3S_1 \to b_1\omega$	$a_1(L=0)$	.310±.012	.265±.009	.204±.009	.150±.014	.180±.012
	$a_2(L=2)$	.077±.007	.073±.011	.070±.011	.076±.011	.061±.017
	$\phi_1(L=0)$	1.59±.03	1.57±0.03	1.45±0.04	1.53±0.04	1.40±0.07
	$\phi_2(L=2)$	2.42±.12	0.90±0.26	0.89±0.19	1.10±0.20	0.68±0.38
	D/S	.194±.036	.222±.053	.135±.063	.260±.083	.284±.069
	$\phi_3(D/S)$	0.26±.18	1.28±0.24	-0.76±0.52	-0.36±0.36	-1.28±.48
$h_1'\omega$	$a_1(L=0)$		.084±0.002	.073±.008	.121±.010	.011±.001
	$\phi_1(L=0)$		1.81±0.27	1.65±0.09	1.86±0.13	2.46±0.12
${}^3S_1 \to \omega(1)\pi^0$	$a_1(L=1)$			0.129±0.012	.152±.016	.094±.019
	$\phi_1(L=0)$			1.98±0.09	1.89±0.09	2.08±.18
${}^3S_1 \to \omega(2)\pi^0$	$a_1(L=1)$					.197±.024
	$\phi_1(L=0)$					2.81±0.09
${}^1P_1 \to a_0\omega$	$a_1(L=1)$			.218±0.001	.236±.041	.247±.033
${}^1P_1 \to \omega(1)\pi^0$	$a_1(L=1)$			.179±.010	.168±.009	.140±.034
	$\phi_1(L=0)$			3.45±0.18	3.11±0.16	1.30±0.26
${}^1P_1 \to \omega(2)\pi^0$	$a_1(L=1)$					.066±.025
	$\phi_1(L=0)$					-0.42±1.00
background	PS	10.6±0.6%	6.9%	6.9%	6.9%	6.9%

Table 24: *Fitted couplings* $\alpha_i = a\, e^{i\phi}$ *of* $\omega\eta\pi^0$ *(see text).*

Fit		$\mathcal{F}1$	$\mathcal{F}2$	$\mathcal{F}3$	$\mathcal{F}3'$	$\mathcal{F}4$
$(\pi\eta)_S$	m_{a_0}	984.7±.6	995.4±.1	995.40±.01	995.48±.01	995.39±.00
	$\tilde{\Gamma}_{\eta\pi}$	65.3±2.1	94.3±1.6	90.6±1.4	88.9±2.4	89.8±2.2
	$\tilde{\Gamma}_{KK}$		1.	1.69±0.14	2.06±.17	1.40±0.09
	$\beta_2\ \ {}^3S_1$		8.82±0.30	8.86±0.34	10.0±0.45	8.74±0.48
	ψ_2		2.02±0.51	2.42±0.04	2.21±0.05	2.36±0.06
	$\beta_2\ \ {}^1P_1$		17.5±5.30	5.26±3.91	4.56±2.72	6.22±3.93
	ψ_2		1.81±0.90	1.70±0.96	1.71±0.92	1.71±0.82
$h'(1380)$	m		1362.1±3.7	1379.5	1368.6±3.6	1379.5±2.6
	$g_{\omega\eta}$		709.±283.	356.±120.	476.±85.	584.0±81.0
	g_{KK^*}		509.±202.	310.±195,	581.±123.	346.4±91.0
ω	m_1					1443.3±3.6
	$\tilde{\Gamma}_1$					210.0±20.2
	m_2			1690.7±4.8	1705.0±7.4	1821.1±6.0
	$\tilde{\Gamma}_2$			107.8±3.5	114.9±4.1	210.5±22.0

Table 25: *Fitted dynamical parameters of $\omega\eta\pi^0$. Units in* MeV, *besides couplings $\beta = be^{i\phi}$*

Fit	$\mathcal{F}1$	$\mathcal{F}2$	$\mathcal{F}3$	$\mathcal{F}3'$	$\mathcal{F}4$
${}^3S_1 \to b_1\eta$	10.5%	7.8%	4.7%	3.0 %	3.9 %
${}^3S_1 \to (\pi\eta)_S\omega$	54.0%	83.1%	78.8%	85.1 %	76.7 %
${}^3S_1 \to a_2\omega$	24.8%	9.0%	7.3%	8.5 %	6.3 %
${}^3S_1 \to h_1\pi^0$		0.7%	0.53%	1.48 %	0.83 %
${}^3S_1 \to \omega(1420)\pi^0$					0.89 %
${}^3S_1 \to \omega(1600)\pi^0$			1.7%	2.32 %	3.9 %
$\sum {}^3S_1$	89.4%	93.1%	88.1 %	87.1 %	86.6 %
${}^1P_1 \to (\pi\eta)_S\omega$			4.8 %	5.6 %	6.1 %
${}^1P_1 \to \omega(1420)\pi^0$					2.0 %
${}^1P_1 \to \omega(1600)\pi^0$			3.2 %	2.8 %	0.4 %
$\sum {}^1P_1$			5.1 %	6.0 %	6.6 %
background	10.6 %	6.9 %	6.9 %	6.9 %	6.9 %
Signal					
$b_1\eta$	11.9±0.6 %	7.8±0.4 %	4.9±0.2 %	2.7±0.13 %	4.1±0.2 %
$(\pi\eta)_S\omega$	60.4±3.0 %	82.7±4.1 %	81.9±4.1 %	81.4±4.1 %	81.1±4.1 %
$a_2\omega$	27.7±1.4 %	8.9±0.4 %	7.6±0.4 %	7.6±0.4 %	6.6±0.3 %
$h_1\pi^0$		0.71±0.03 %	0.55±0.03 %	1.3±0.1 %	0.56±0.03 %
$\omega(1420)\pi^0$					4.5±0.25 %
$\omega(1600)\pi^0$			5.0±0.3 %	6.9±0.4 %	3.0±0.15 %

Table 26: *Contributions of $\omega\eta\pi^0$(see text).*

fitted and observed Dalitz plot are displayed in fig. 46 and the $\cos\theta$ distribution in fig. 47.

In the relative difference of the Dalitz plot it is clearly visible that a state in the region of 1700 MeV is still missing.

In the next extension of the fit hypothesis, an axial vector (1^{+-}) and a vector (1^{--}) state in the region 1600-1700 MeV are studied. The fit $\mathcal{F}3$ prefers a vector state at

$$m_V = 1690 \pm 5 \text{ MeV} \quad \text{and} \quad \Gamma_V = 108 \pm 4 \text{ MeV} \tag{99}$$

The vector state at 1690 MeV and the axial vector state at 1380 MeV contribute to a considerable improvement of likelihood and χ^2 (see tab. 24). Figure 48c,d displays now a fairly flat distribution of the relative deviation and the angular distributions in figure 49 and 50 fits well the data.

Some improvement is also due to the inclusion of the ${}^1P_1$ initial state. The mass of the vector state shifts slightly towards higher values if the $a_2(1320)$ is also allowed to be produced with $L = 2$, while the overall contribution from a_2 stays stable (fit $\mathcal{F}3$')

In fit $\mathcal{F}4$ a two pole parameterization for the $(\omega\eta)_P$ wave instead of the $\omega(1690)$ is included and leads to the stable states with the K-matrix poles at

$$m_1 = 1443 \pm 4 \text{ MeV} \quad \text{and} \quad \Gamma_1 = 210 \pm 20 \text{ MeV} \tag{100}$$

$$m_2 = 1821 \pm 6 \text{ MeV} \quad \text{and} \quad \Gamma_2 = 211 \pm 22 \text{ MeV} \tag{101}$$

However, the values for the likelihood of the three solutions $\mathcal{F}3$, $\mathcal{F}3$' and $\mathcal{F}4$ differ only little. The mass projections of fit $\mathcal{F}4$ are shown in fig. 51, the χ^2 Dalitz plot in fig. 52 and the angular distributions in fig. 53 and 54.

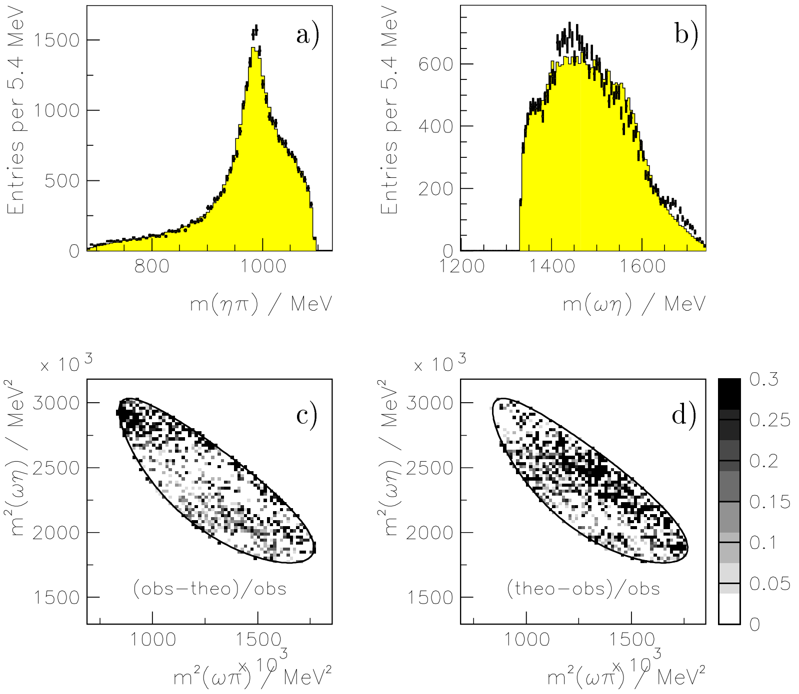

Figure 46: *Result of the fit $\mathcal{F}2$: (a,b) show the measurement (error bars) and the fit (solid line) of the invariant mass spectra $m(\eta,\pi)$ and $m(\omega\eta)$; and (c,d) the relative difference between measured and fitted Dalitz plot in $m^2(\omega\eta)$ vs $m^2(\omega\pi)$.*

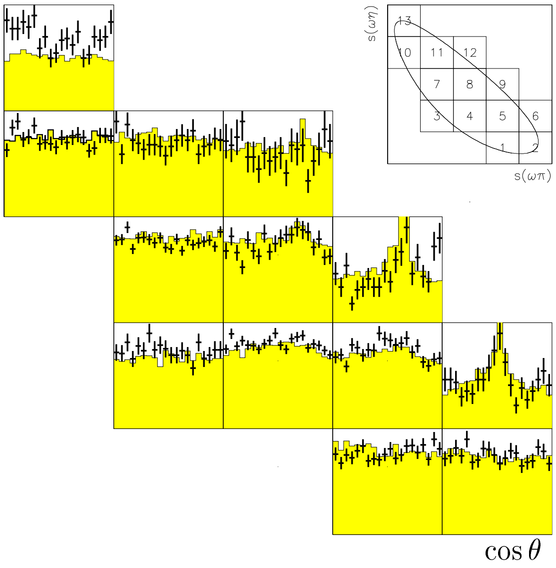

Figure 47: cos θ *distribution of fit $\mathcal{F}2$*

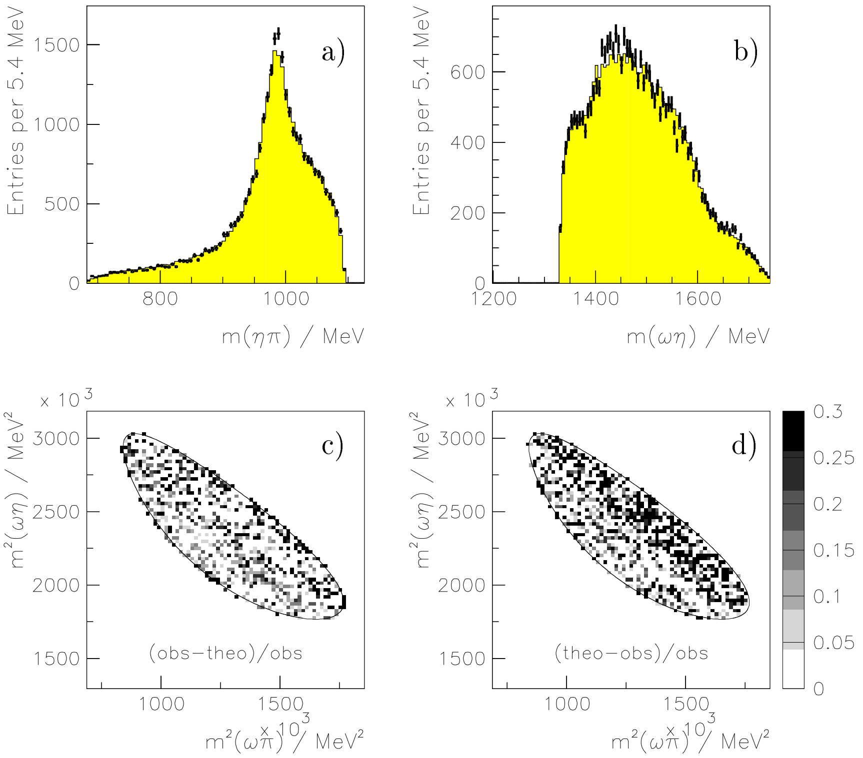

Figure 48: *Result of the fit $\mathcal{F}3$: (a,b) show the measurement (error bars) and the fit (solid line) of the invariant mass spectra $m(\eta,\pi)$ and $m(\omega\eta)$; and (c,d) the relative difference between measured and fitted Dalitz plot in $m^2(\omega\eta)$ vs $m^2(\omega\pi)$.*

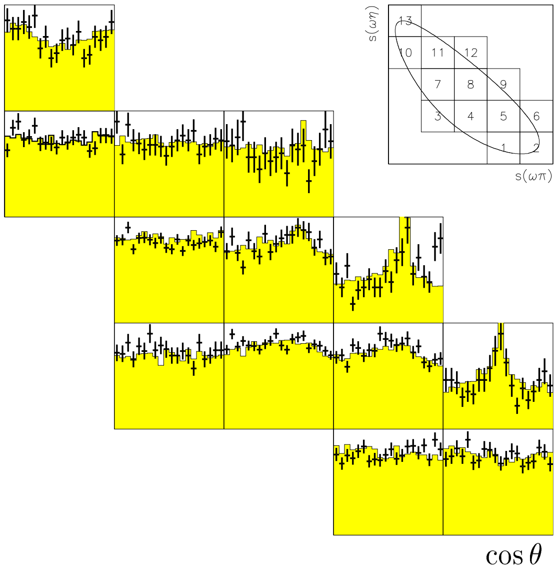

Figure 49: $\cos\theta$ *distribution of fit* $\mathcal{F}3$

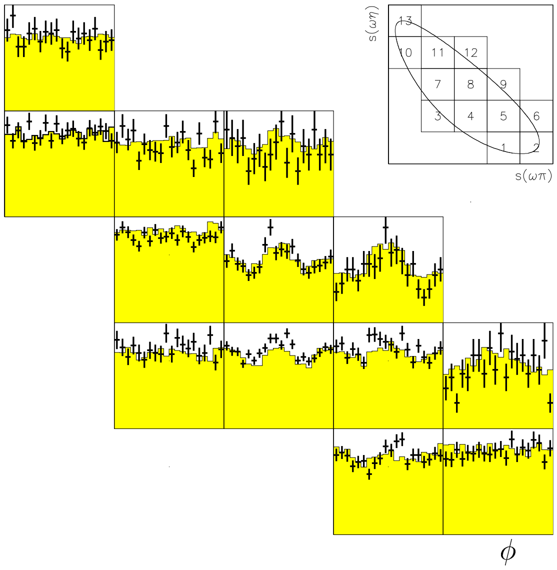

Figure 50: ϕ *distribution of fit* $\mathcal{F}3$

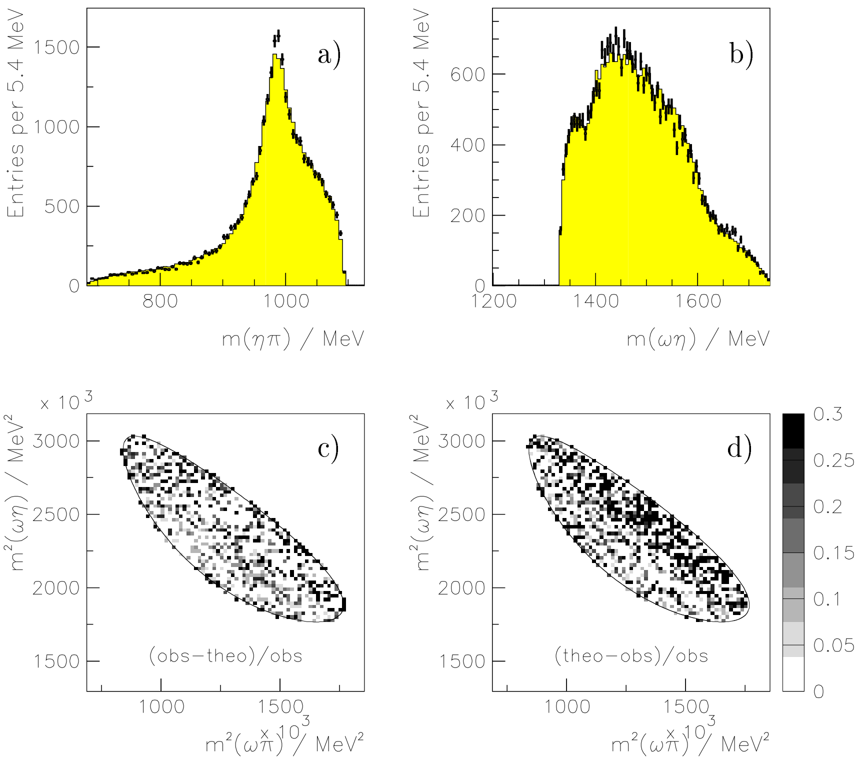

Figure 51: *Result of the fit $\mathcal{F}4$: (a,b) show the measurement (error bars) and the fit (solid line) of the invariant mass spectra $m(\eta,\pi)$ and $m(\omega\eta)$; and (c,d) the relative difference between measured and fitted Dalitz plot in $m^2(\omega\eta)$ vs $m^2(\omega\pi)$.*

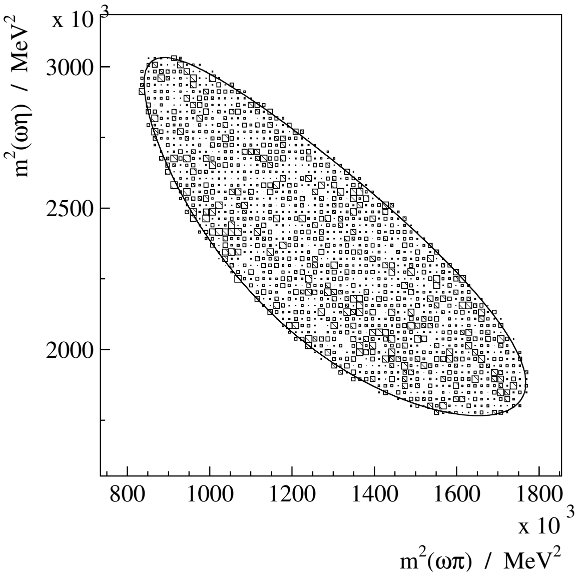

Figure 52: *χ^2 Dalitz plot of fit $\mathcal{F}4$*

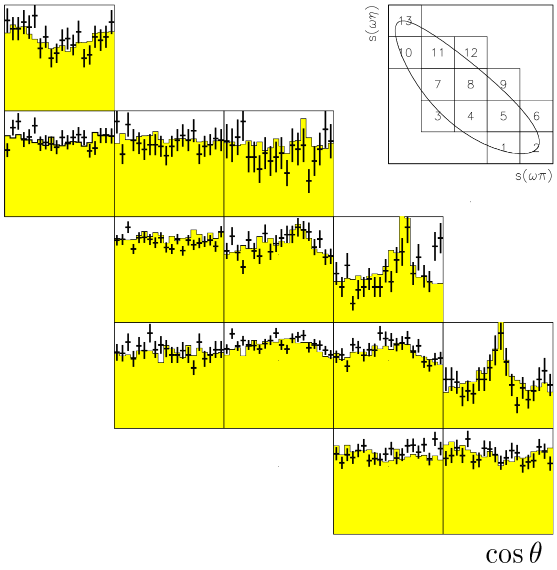

Figure 53: $\cos\theta$ *distribution of fit* $\mathcal{F}4$

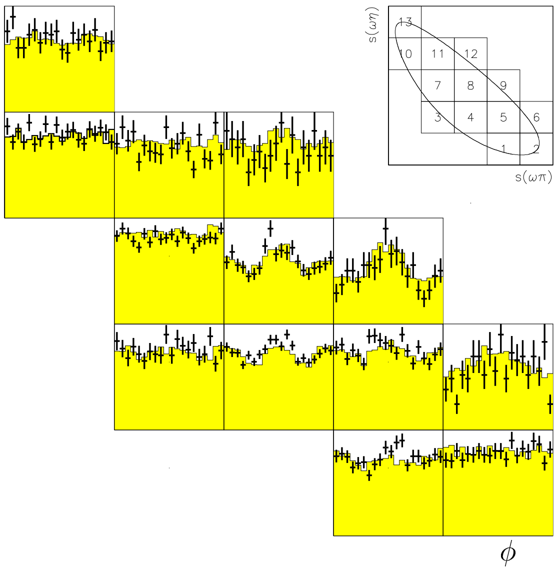

Figure 54: ϕ *distribution of fit* $\mathcal{F}4$

9 Discussion

9.1 Branching Ratios and Meson Production in $\bar{p}p$ Annihilation

The partial wave analysis shows that $\omega\pi^0\pi^0$ is well described by the $b_1(1230) \to \omega\pi^0$ (38±3 %[6]), the $(\pi\pi)_S$ wave (43±2 %) and the tail of the $f_2(1270) \to \pi^0\pi^0$ (17±4 %). The fitted contributions of the signal are fairly independent on the extension of the basic fit. The branching ratios for the meson production in $\bar{p}p$ are calculated from the contributions (tab. 19 and 26) and the known decay ratios from PDG [8] and are listed in table 27. The fit result can be improved without changing significantly the individual contribution of the involved mesons by inclusion of $^1P_1$ $\bar{p}p$ initial state which then contributes 39.5% whereas $^3S_1$ shrinks to 60.5%.

The fits of $\overline{p}p \to \omega\eta\pi^0$ require the $a_0(980) \to \eta\pi^0$ (81.5±4.1 %), $a_2(1320) \to \eta\pi^0$ (7.3± %0.3), the $b_1(1230) \to \omega\pi^0$ (3.9±0.6 %) and, in contrast to the previous analysis [30], an axial vector $h_1(1380) \to \omega\eta$ (0.80±0.25 %) and a vector meson $\omega(1700) \to \omega\eta$ (5.0±1.0 %). The contribution from $^1P_1$ initial state is small, around 6%. Table 27 contains the branching ratios averaged over the three relevant fits.

Branching ratios							
$B(\overline{p}p \to \omega\pi^0\pi^0)$	=	2.71	±	0.25	±	0.26	%
$B(\bar{p}p \to b_1^0\,\pi^0)$	=	1.04	±	0.05	±	0.14	%
$B(\bar{p}p \to \omega\,(\pi\pi)_S)$	=	3.43	±	0.12	±	0.46	%
$B(\bar{p}p \to f_2\,\omega)$	=	1.64	±	0.25	±	0.22	%
$B(\overline{p}p \to \omega\eta\pi^0)$	=	1.06	±	0.15	±	0.10	%
$B(\bar{p}p \to b_1^0\,\eta)$	=	4.1	±	0.7	±	0.8	$\times 10^{-4}$
$B(\bar{p}p \to (\pi\eta)_S\,\omega)$	=	8.6	±	0.2	±	1.6	$\times 10^{-3}$
$B(\bar{p}p \to a_0^0\,\omega)$	=	7.1	±	0.3	±	1.0	$\times 10^{-3}$
$B(\bar{p}p \to a_2^0\,\omega)$	=	5.3	±	0.2	±	0.9	$\times 10^{-3}$
$B(\bar{p}p \to h_1(1380)\,\pi^0,\ h_1 \to \omega\eta)$	=	8.5	±	2.6	±	1.6	$\times 10^{-5}$
$B(\bar{p}p \to \omega(1600)\,\pi^0, \omega \to \omega\eta)$	=	5.3	±	1.2	±	1.0	$\times 10^{-4}$

Table 27: *Meson production in $\overline{p}p \to \omega\pi^0\pi^0$ and $\overline{p}p \to \omega\eta\pi^0$. The branching ratios are calculated from the fitted contributions and the known decay ratios from PDG [8]. The first error refers to the fitted contribution, the second to the uncertainty of the branching ratios used for the calculation.*

---

[6] averaged over the relevant fits

The ratio of the branching ratios $B(\bar{p}p \to \omega(\pi\pi)_S)$ and $B(\bar{p}p \to \phi\pi^0\pi^0) = 9.7 \pm 2.6 \times 10^{-5}$ [11][7] is

$$r = \frac{B(\phi(\pi\pi)_S)}{B(\omega(\pi\pi)_S)} \frac{q_\omega m_\phi}{q_\phi m_\omega} = (1.4 \pm 0.4) \times 10^{-2} \tag{102}$$

and confirms the observation that ϕ meson production in $\bar{p}p$ annihilation is enhanced with respect to the $SU(3)$ prediction $r_{SU(3)} = 0.42 \times 10^{-2}$ [27].

9.2 The $(\pi\pi)_S$ Wave

In contrast to the previous analysis [29], the $\pi^0\pi^0$ mass projection in $\omega\pi^0\pi^0$ can be fully described now. The $(\pi\pi)_S$-wave contributing with 43 % to $\omega\pi^0\pi^0$ is parameterized by a 3×3 K-matrix including the coupling to $\pi\pi$, $\eta\eta$ and $K\overline{K}$, using the pole positions of the σ, $f_0(980)$ and $f_0(1370)$ from the coupled channel analysis of ref. [25]. The corresponding T-matrix poles are determined by applying the method described in ref. [69] and are listed in tab. 28. Like in $\bar{p}p \to 3\pi^0$, at the region of the $f_0(980)$, a dip occurs in the $(\pi\pi)_S$ production amplitude. Figure 55 displays the different line shapes of the $(\pi\pi)_S$ wave in the final states $\omega\pi^0\pi^0$, $\eta\pi^0\pi^0$ and $\pi^0\pi^0\pi^0$. The enhancement above the $f_0(980)$ is due to the presence of the $f_0(1370)$ and describes mainly the rise of the $\pi^0\pi^0$ mass spectrum in $\omega\pi^0\pi^0$. Besides the contribution from the tail of the $f_2(1270)$ no further resonances decaying into $\pi\pi$ are required above 1 GeV.

	II (- + +)		III (- - +)		IV (- - -)	
	m	Γ	m	Γ	m	Γ
σ	540±20	850±10	1088±10	266±5	1105±10	283±5
$f_0(980)$	1009±10	110±2	962±5	131±5	947±5	90±5
$f_0(1370)$	1350±10	272±5	1353±10	393±5	1330±10	402±5

Table 28: *T-matrix poles of the $(\pi\pi)_S$ wave in the three relevant Riemann sheets. Values are given in MeV.*

9.3 The $(\omega\pi)_P$ Wave

There is no evidence for the presence of a narrow vector meson decaying into $\omega\pi^0$, neither for $\rho(1260)$ reported in ref. [33] nor for $C(1480)$ observed in the $\phi\pi$ decay

---

[7] The ratio is derived using $B(\phi \to K_L K_S) = 0.341 \pm 0.006$ from [8].

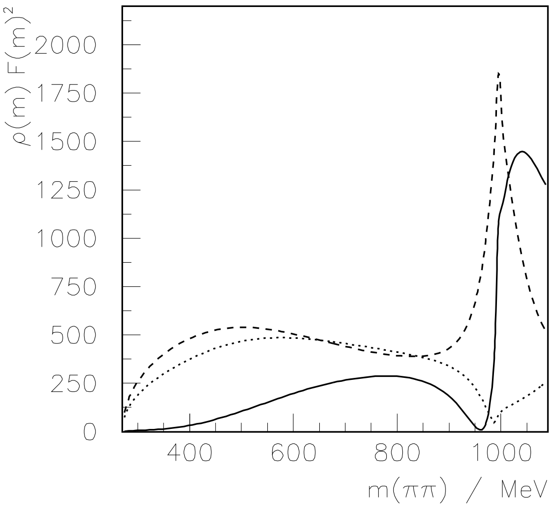

Figure 55: *$(\pi\pi)_S$,wave production amplitude squared $\mid F(m) \mid^2$; in $\omega\pi^0\pi^0$ (solid line), $\eta\pi^0\pi^0$ (dashed line) and $\pi^0\pi^0\pi^0$ (dotted line).*

mode [15]. The fits prefers large width for ρ contribution. However, no stable solution for mass and width can be found for the mass region around 1400 MeV. The inclusion of $^1P_1$ $\bar{p}p$ initial state allows an improved fit and leads to a stable result with a high mass ρ at

$$m_\rho = 1738 \pm 1 \text{ MeV} \quad \text{and} \quad \Gamma_\rho = 327 \pm 63 \text{ MeV} \tag{103}$$

with the branching ratio

$$B(\bar{p}p \to \rho(1700)\,\pi^0, \rho \to \omega\pi^0) = 1.07 \pm 0.16_{stat} \pm 0.14_{sys} \times 10^{-3}\,. \tag{104}$$

This state agrees well with the PDG values for $\rho(1700)$, 1723 ± 11 MeV and 240 ± 40 MeV. Though the angular distribution seems to favor contributions from ρ's, no stable results for masses and widths of more than one ρ pole in the $(\omega\pi^0)_P$ wave can be found.

9.4 D-Wave to S-Wave Amplitude Ratio for $b_1 \to \omega\pi^0$

The measured D-wave to S-wave amplitude ratio for $b_1 \to \omega\pi^0$ is very sensitive to the fit hypothesis. For the relevant fits of $\omega\pi^0\pi^0$ they vary over a range of 0.13 to 0.20 with an average of $D/S = 0.18 \pm 0.04$ and for $\omega\eta\pi^0$ over 0.14 to 0.28 with an average of $D/S = 0.23 \pm 0.08$. The errors reflects the variability of the ratios for various fits. Both D/S ratios are lower but still in agreement with the PDG average 0.29 ± 0.04 [8]. The relative phase of D-wave to S-wave is $-42 \pm 29\,^\circ$ and $-46 \pm 26\,^\circ$, respectively.

The $b_1 \to \omega\pi$ decay can be used to test the two competing models for strong hadronic decays – the ${}^3P_0$ and ${}^3S_1$ models. The strong hadronic decay proceeds by simple quark rearrangement and $q\bar{q}$ pair creation from vacuum either with $J^{PC}(q\bar{q}) = 0^{++}$ (${}^3P_0$) or with $J^{PC}(q\bar{q}) = 1^{--}$ (${}^3S_1$) [20]. The ${}^3S_1$ model predicts a $D/S \approx 0.05$ whereas ${}^3P_0$ requires a value around 0.25, clearly favored by our measurement.

9.5 Properties of the $a_0(980)$ Meson

From the fitted K-matrix partial width $\tilde{\Gamma}_{\eta\pi}$ and $\tilde{\Gamma}_{K\overline{K}}$ of the $(\pi\eta)_S$ wave (tab. 25) we retrieve the coupling ratio R of the $a_0(980)$ coupling to the channel $\eta\pi^0$ and $\overline{K}K$ (eq. (78):

$$R(a_0) = \frac{g^2(K\overline{K})}{g^2(\eta\pi^0)} = 1.06 \pm 0.07 \tag{105}$$

The values from fit $\mathcal{F}3$, $\mathcal{F}3$' and $\mathcal{F}4$ agree within their errors and are averaged. The error is statistical and reflects also the systematics owing to the three fits. The averaged couplings are $g_{K\overline{K}} = 377 \pm 23\,\mathrm{MeV}$ and $g_{\eta\pi} = 367 \pm 2\,\mathrm{MeV}$ and the averaged phase space factors $\rho(\eta\pi) = 0.6628 \pm 0.0001$ and $\rho(K\overline{K}) = (1.22 \pm 0.22) \times 10^{-2}$. The measured ratio R is in good agreement with $R = 1.03 \pm 0.14$ from the measurement $a_0^\pm \to K_L K^\pm$ [18], $R = 1.15 \pm 0.10$ from $a_0 \to \eta\pi^0$ [45] and $R = 0.91 \pm 0.10$ from $a_0^\pm \to \eta\pi^\pm$ [71].

Neglecting the second pole in the 2×2 K-matrix of the $(\pi\eta)_S$ wave one gets the Flatté formula (see sec. 8.3, eq. (77)):

$$\hat{F}_i(m) = \frac{\beta^0\,\hat{g}_i}{m_\alpha^2 - m^2 - i\{\rho_1\,g_1^2 + \rho_2\,g_2^2\}} \tag{106}$$

Figure 56 displays the $\eta\pi$ line shape with and without the second pole. The $a_0(1450)$ contributes with $8.0 \pm 0.5\%$ to the total intensity of the wave and is responsible for the enhancement towards higher mass. From the phase space integrated amplitudes F_i of the Flatté term one finds the ratio of branching ratios

$$r(a_0) = \frac{B(a_0(980) \to K\overline{K})}{B(a_0(980) \to \eta\pi^0)} = \frac{\int \rho(K\overline{K})\,|F(K\overline{K})|^2\,dm}{\int \rho(\eta\pi^0)\,|F(\eta\pi^0)|^2\,dm} = 0.35 \pm 0.08 \tag{107}$$

which is somewhat higher but still in good agreement with 0.23 ± 0.05 calculated from $B(\bar{p}p \to a_0\pi,\, a_0 \to \overline{K}K) = 5.92^{+0.46}_{-1.01} \times 10^{-4}$ [18] and $B(\bar{p}p \to a_0\pi^0,\, a_0 \to \eta\pi^0) = 8.7 \pm 1.6 \times 10^{-4}$ [45].

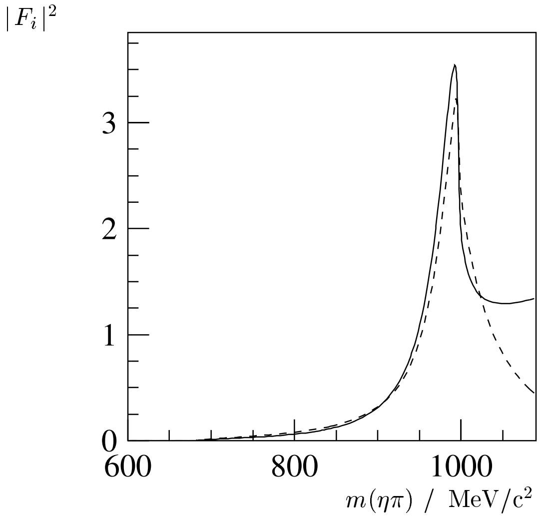

Figure 56: *$(\pi\eta)_S$ line shape, according to the two pole K-matrix solution (solid line) and the Flatté term corresponding to the first pole (dashed line).*

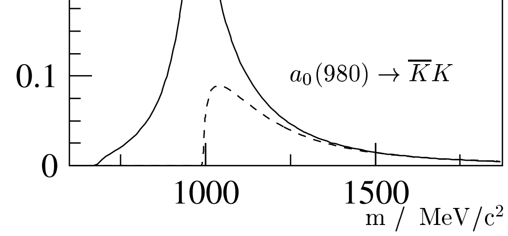

Figure 57: $a_0(980)$ *line shape given by the Flatté amplitude $\rho_i \mid F_i \mid^2$ of* $a_0(980)$ *for the channels $\eta\pi^0$ (solid line) and $K\overline{K}$ (dashed line).*

The T-matrix poles of the $(\pi\eta)_S$ are determined by applying the method described in ref. [69]. The pole positions in the complex energy plane ($E = m - i\Gamma/2$) corresponding to the fitted parameters coincide within their error for the fits $\mathcal{F}$3-4. The relevant pole lays on sheet III (see appendix B) at

$$m = 982 \pm 3\,\mathrm{MeV} \quad \Gamma = 91 \pm 2\,\mathrm{MeV} \tag{108}$$

The poles of $a_0(980)$ and $a_0(1450)$ from the fit $\mathcal{F}4$ are given in table 29.

	II (- +)		III (- -)	
	m	Γ	m	Γ
$a_0(980)$	1002.9±3	107.3±3	982±3	90.7±3
$a_0(1450)$	1509.9±5	232.1±5	1504.2±5	231.2±5

Table 29: *T-matrix poles of the $(\pi\eta)_S$ wave of fit $\mathcal{F}4$ in the two relevant Riemann sheets II and III. Values are given in MeV. The sheets are numbered according to the signs (in parenthesis) of the imaginary part of the break-up momenta for the decays into $\eta\pi$ and $K\overline{K}$.*

9.6 $h_1(1380) \to \omega\eta$ and the Axial Vector Nonet

The 1^{+-} state decaying to $\omega\eta$ is also described by a 2×2 K-matrix (Flatté formula), assuming the unobserved decay mode to be $K^*\overline{K}$. In contrast to the $a_0(980)$ the fitted K-matrix pole is below the second threshold and the relevant T-matrix pole, hence, occurs on sheet II (see appendix B) at

$$m = 1382 \pm 2\,\mathrm{MeV} \quad \Gamma = 65 \pm 14\,\mathrm{MeV} \tag{109}$$

whereas the "shadow" pole is on sheet III at $m = 1351 \pm 12\,\mathrm{MeV}$, $\Gamma = 31 \pm 16\,\mathrm{MeV}$. The state coincides with the $h_1'(1380)$, reported in the $K^*\overline{K}$ decay mode by LASS [10] ($m = 1380 \pm 20$ MeV, $\Gamma = 80 \pm 30$) and Crystal Barrel [11] ($m = 1440 \pm 60$ MeV, $\Gamma = 170 \pm 80$), but whose isospin has not been measured unambiguously. The line shape of the h_1' is displayed in figure 58. The dashed line shows the Flatté amplitude of the unobserved decay into $K^*\overline{K}$ and the dotted line the shape of the Breit-Wigner amplitude corresponding to the result of ref. [11]. The ratio of the decay branching ratios is determined by integrating the amplitudes and averaging over the fits $\mathcal{F}3$-$\mathcal{F}4$:

$$r(h_1') = \frac{B(h_1'(1380)\to K\overline{K}^*)}{B(h_1'(1380)\to\omega\eta)} = \frac{\int \rho(K\overline{K}^*)\,|F(K\overline{K}^*)|^2\,dm}{\int \rho(\omega\eta)\,|F(\omega\eta)|^2\,dm} = 0.17 \pm 0.06 \tag{110}$$

From this ratio and the measured branching ratio $B(\bar{p}p \to h_1'\pi^0,\, h_1' \to \omega\eta) = (0.85 \pm 0.26) \times 10^{-4}$ (tab. 27) we calculate the branching ratio $B(\bar{p}p \to h_1'\pi^0,\, h_1' \to K\overline{K}^*) = (0.14 \pm 0.06) \times 10^{-4}$ which is compatible with the measured ratio of $5.4 \pm 3.5 \times 10^{-4}$ in $\bar{p}p \to K_L K_S \pi^0\pi^0$ [11][8] if one considers the large errors. However, the $h_1'(1380)$ is not favored in an analysis of $\bar{p}p \to K_L K^\pm \pi^\mp \pi^0$ to explain the excess of events at 1400 MeV in $\overline{K}K^*$, though a significant contribution is expected [11, 68]. The branching ratio may be smaller and hence in better agreement with our measurement.

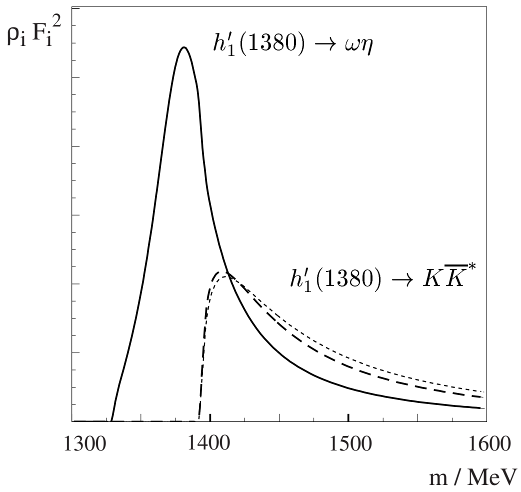

Figure 58: $h_1'(1380)$ *line shapes given by the fitted amplitude* $\rho_i \mid F_i \mid^2$ *of* $h_1'(1380)$ *for channels* $\eta\pi^0$ *(solid line) and* $K\overline{K}^*$ *(dashed line, multiplied by six) together with the Breit-Wigner amplitude for* $m =$*1440* MeV *and* $\Gamma=$*170* MeV *(dotted line).*

From the fitted coupling constants of the Flatté formula one gets the relative coupling

$$R(h_1') = \frac{g^2(\omega\eta)}{g^2(K\overline{K}^*)} = 1.6 \pm 0.6\ . \tag{111}$$

---

[8] The measured contribution of $h_1' \to K_L K_S \pi^0$ is multiplied by isospin factor 6 for $h_1' \to K\overline{K}\pi$.

The ratio can also be expressed in terms the of $SU(3)$ mixing angles and flavor symmetry assuming that the relative creation of $u\overline{u}$, $d\overline{d}$ and $s\overline{s}$ is equally probable. The final states in terms of $q\bar{q}$ are given by

$$\begin{aligned} |\,h\rangle &= \cos\alpha\,|\,n\bar{n}\rangle - \sin\alpha\,|\,s\bar{s}\rangle \\ |\omega\rangle &= \sin\psi\,|\,n\bar{n}\rangle + \cos\psi\,|\,s\bar{s}\rangle \\ |\,\eta\rangle &= \cos\phi\,|\,n\bar{n}\rangle - \sin\phi\,|\,s\bar{s}\rangle \end{aligned}$$

where $|\,n\bar{n}\,\rangle$ denotes the $|\,u\bar{u}+d\bar{d}\,\rangle$ system. From the evaluation of the quark line transition matrix M one finds for the ratio (derivation given in appendix C)

$$R \;=\; \frac{g^2(h\!\to\omega\eta\,)}{g^2(h\!\to\!K\overline{K}^*)} = \left[\frac{2\sin\alpha\cos\psi\sin\phi+\sqrt{2}\cos\alpha\sin\psi\cos\phi}{\sqrt{2}\cos\alpha-2\sin\alpha}\right]^2 . \tag{112}$$

Within the experimental limits (see eq. (111)) and taking into account the mixing angle for pseudoscalar and vector mesons ($\phi = 54.7^\circ + \theta_{PS} = 37.4^\circ$ [72] and $\psi = 54.7^\circ + \theta_V = 90.7^\circ$ [8]) one gets then two solutions for the mixing angle α (see fig. 59):

$$\begin{aligned} \alpha_1 &= 14.8\,{}^{+3.6}_{-5.5}\;{}^\circ \\ \alpha_2 &= 48.9\,{}^{+2.7}_{-1.6}\;{}^\circ \end{aligned}$$

The result can be compared with the two solutions from the Gell-Mann-Okubo mass formula and the linear mixing angle [8]. Taking into account the PDG masses for b_1 and h_1 [8], $m(K_{1B}) = 1340\,\mathrm{MeV}$[9] and $m(h_1') = 1382 \pm 2\,\mathrm{MeV}$ from this work, one finds the singlet-octet mixing angle $\theta_A^{\pm} = \pm(9.0 \pm 1.0 \pm 5.0)^\circ$ and the $q\bar{q}$ mixing angles $\alpha^+ = 63.7 \pm 1.0 \pm 5.0^\circ$ and $\alpha^- = 45.7 \pm 1.0 \pm 5.0^\circ$ ($\alpha = 54.7^\circ + \theta_A$), respectively. The first error stems from the measurement of the h_1' mass, the second error reflects the uncertainties of the remaining nonet masses. The second solution agrees well with α_2 which corresponds to the (measured) axial vector mixing angle

$$\theta_A = \alpha_2 - 54.7^\circ = -5.8\,{}^{+2.7}_{-1.6}\;{}^\circ . \tag{113}$$

The $h_1'(1380)$ is a nearly pure $SU(3)$ octet and the $h_1(1170)$ a pure $SU(3)$ singlet isoscalar (see eq. (1),(2)). It is interesting to note that pseudoscalar and axial vector mesons are both spin singlet ($S=0$) states with a small singlet-octet mixing, whereas the established spin triplet ($S=1$) nonets 1^{--}, 2^{++} and 3^{--} are almost ideally mixed ($\theta \approx 35.3^\circ$).

---

[9] K_{1B} is a nearly equal mix of $K_1(1270)$ and $K_1(1400)$ [19].

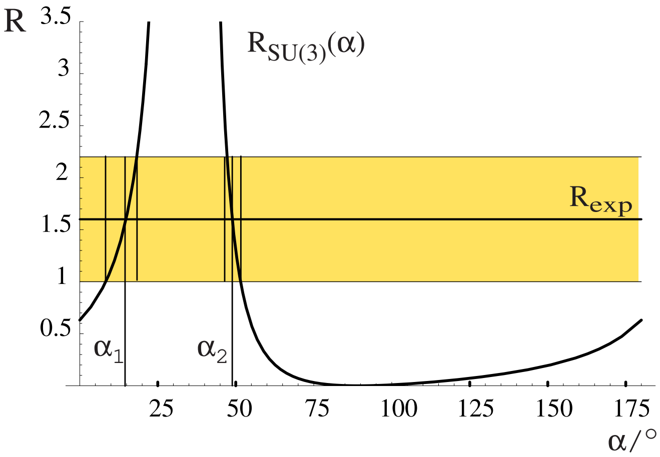

Figure 59: *The relative couplings of* $h_1'(1380)$. *The ratio* $R = g^2(\omega\eta)/g^2(K\overline{K}^*)$ *is determined from* $SU(3)$*-flavor symmetry depending on the axial vector mixing angle* α *(*$R_{SU(3)}(\alpha)$*, eq. (112)). The shaded area marks the experimental region from the measured Flatté couplings (*$R_{exp} = 1.6 \pm 0.6$*). The angles* α_1 *and* α_2 *denote the two solutions for the axial vector mixing.*

9.7 The $(\omega\eta)_P$ Wave

A resonance in the $(\omega\eta)_P$ wave at 1700 MeV is definitively required for a satisfactory description of the $\omega\eta\pi^0$ signal. The fitted mass and width for the vector state is $m = 1698 \pm 6$ MeV and $\Gamma = 111 \pm 4$ MeV - in agreement with PDG value for $\omega(1600)$ of $m = 1649 \pm 24$ MeV and $\Gamma = 220 \pm 35$. The slightly higher mass of our measurement may be due to the strong influence of the Blatt-Weisskopf damping for the $L = 1$ $\omega(1600)$ production at the border of phase space which shifts the mass peak to lower values.

The excess of events around 1450 MeV may be an indication for a further vector resonance - the $\omega(1420)$ observed dominantly in the $\rho\pi$ decay mode [8]. However, the inclusion of a second pole in the $(\omega\eta)_P$ wave shifts the higher mass outside of phase space and contributes only weakly to a better description. The T-matrix poles found for the two-pole solution are (on sheet II) $m_1 = 1369 \pm 10$ MeV, $\Gamma_1 = 128 \pm 10$ MeV and $m_2 = 1764 \pm 10$ MeV, $\Gamma_2 = 139 \pm 10$ MeV.

The line shapes of the two solutions differ mainly in the region of 1400 MeV, where some intensity may be missed due to an incomplete parametrization of the h_1' or to the absence of contributions from further initial states. On the other hand, we have also to consider that $\omega(1420)$ and $\omega(1600)$ couple to $\rho\pi$ and to $\omega\pi\pi$ and that their description may require a more sophisticated parameterization in K-matrix formalism.

10 Conclusions

For the first time the final states of $\overline{p}p \to \omega\pi^0\pi^0$ and $\overline{p}p \to \omega\eta\pi^0$ can be satisfactorily described including the angular distribution of $\omega \to \pi^0\gamma$. The analysis of $\overline{p}p \to \omega\pi^0\pi^0$ shows that, besides the $b_1(1235)$ and the $f_2(1270)$, the $(\pi\pi)_S$ wave in the parametrization of ref. [25] is the essential ingredient of the description. The inclusion of the $\rho(1700)$ and ${}^1P_1$ $\bar{p}p$ initial state leads to an improved and stable fit result. Though the angular distribution seems to favor contributions from ρ's, no stable results for masses and widths of more than one ρ pole in the $(\omega\pi^0)_P$ wave were found. The $\rho(1450)$ can neither be confirmed nor excluded in this final state. The good description around 1 GeV and the depleted region between the b_1 bands indicates that no further resonances occur in the $\pi^0\pi^0$ system.

The analysis of $\overline{p}p \to \omega\eta\pi^0$ reveals at least two resonances in the $\omega\eta$ system, a narrow axial vector at 1380 MeV and a vector at 1700 MeV. This is the first observation of such resonances decaying into $\omega\eta$ in $\bar{p}p$ annihilation. The state at 1380 MeV coincides with the axial vector observed in $K\overline{K}^*$ by LASS [10] and by Crystal Barrel [11]. The observation of the $\omega\eta$ decay mode resolves now the ambiguity of the isospin. The coupling to $\overline{K}^*K$ and the observed mass and width of this state confirm the interpretation as the $h_1'(1380)$ – the missing isoscalar of the 1^{+-} nonet. The measured couplings lead to an octet-singlet mixing angle of $\theta_A = -5.8^{+2.7}_{-1.6}\,^\circ$ which agrees well with the linear mixing angle of the axial vector nonet. The vector state at 1700 MeV is attributed to $\omega(1600)$. The evidence for a further vector state around 1400 MeV is questionable and needs further confirmation. Table 30 summarizes the masses and widths of mesons determined in this work.

Masses and widths		
$\omega(782)$	m = $781.86 \pm 0.05 \pm 0.1$ MeV	
$\omega(782)$	m = $782.58 \pm 0.11 \pm 0.2$ MeV	
$a_0(980)$	m = 982 ± 3 MeV	$\Gamma = 91 \pm 2$ MeV
$b_1(1235)$ $^{(a)}$	m = 1238 ± 1 MeV	$\Gamma = 148 \pm 3$ MeV
$h_1'(1380)$	m = 1382 ± 2 MeV	$\Gamma = 65 \pm 14$ MeV
$\rho(1700)$	m = 1738 ± 1 MeV	$\Gamma = 327 \pm 63$ MeV
$\omega(1700)$ $^{(b)}$	m = 1698 ± 6 MeV	$\Gamma = 111 \pm 4$ MeV

Table 30: *Summary of the masses and widths of* $\overline{p}p \to \omega\pi^0\pi^0$ *and* $\overline{p}p \to \omega\eta\pi^0$. *Remarks: (a) The* b_1 *mass is taken from the best fit* ($\mathcal{F}4$) *of* $\omega\pi^0\pi^0$ *and (b) the ω(1700) corresponds to the one pole solutions for the* $(\omega\eta)_P$ *wave in* $\omega\eta\pi^0$.

A Examples of Helicity Amplitudes

Helicity amplitude of the ω decay:

$$H^{111}(\omega \to \pi^0\gamma) = \frac{1}{\sqrt{2}} \begin{pmatrix} \frac{1+\cos\theta}{2}\, e^{-i\phi} & 0 & -\frac{1-\cos\theta}{2}\, e^{-i\phi} \\ -\sin\theta/\sqrt{2} & 0 & -\sin\theta/\sqrt{2} \\ \frac{1-\cos\theta}{2}\, e^{i\phi} & 0 & -\frac{1+\cos\theta}{2}\, e^{i\phi} \end{pmatrix}^T \tag{114}$$

Examples of the angular part of $\tilde{A}_i$ (see eq. 69)[10] :

$$\tilde{H}^{LSls}_{M;\lambda}({}^3S_1 \to b_1\pi^0, b_1 \to \omega\pi^0, L=0, l=0)$$

$$\begin{aligned} H_{1;\lambda} &= \begin{pmatrix} \cos(\frac{t1+t2+t3}{2})^2 \\ \frac{\sin(t1+t2+t3)}{\sqrt{2}} \\ \sin(\frac{t1+t2+t3}{2})^2 \end{pmatrix}^T \\ H_{2;\lambda} &= \begin{pmatrix} -\frac{\sin(t1+t2+t3)}{\sqrt{2}} \\ \cos(t1+t2+t3) \\ \frac{\sin(t1+t2+t3)}{\sqrt{2}} \end{pmatrix}^T \\ H_{3;\lambda} &= \begin{pmatrix} \sin(\frac{t1+t2+t3}{2})^2 \\ -\frac{\sin(t1+t2+t3)}{\sqrt{2}} \\ \cos(\frac{t1+t2+t3}{2})^2 \end{pmatrix}^T \end{aligned} \tag{115}$$

---

[10] $(t1, t2, t3)$ are the rotation angles in the three-body decay plane $(\theta_0^{(i)}, \theta_R^{(i)}, \theta_{(i)1})$. See section 8.2

$$\tilde{H}^{LSls}_{M;\lambda}(^3S_1 \to b_1\pi^0, b_1 \to \omega\pi^0, L = 2; l = 2)$$

$$\begin{aligned}
H_{1;\lambda} &= \begin{pmatrix} \frac{4-3\,\cos(t1-t2-t3)-3\,\cos(t1+t2-t3)+9\,\cos(t1-t2+t3)+\cos(t1+t2+t3)}{80} \\ \frac{3\,\sin(t1-t2-t3)+3\,\sin(t1+t2-t3)+9\,\sin(t1-t2+t3)+\sin(t1+t2+t3)}{40\,\sqrt{2}} \\ \frac{4+3\,\cos(t1-t2-t3)+3\,\cos(t1+t2-t3)-9\,\cos(t1-t2+t3)-\cos(t1+t2+t3)}{80} \end{pmatrix}^T \\
H_{2;\lambda} &= \begin{pmatrix} \frac{-(-3\,\sin(t1-t2-t3)-3\,\sin(t1+t2-t3)+9\,\sin(t1-t2+t3)+\sin(t1+t2+t3))}{40\,\sqrt{2}} \\ \frac{3\,\cos(t1-t2-t3)+3\,\cos(t1+t2-t3)+9\,\cos(t1-t2+t3)+\cos(t1+t2+t3)}{40} \\ \frac{-3\,\sin(t1-t2-t3)-3\,\sin(t1+t2-t3)+9\,\sin(t1-t2+t3)+\sin(t1+t2+t3)}{40\,\sqrt{2}} \end{pmatrix}^T \\
H_{3;\lambda} &= \begin{pmatrix} \frac{4+3\,\cos(t1-t2-t3)+3\,\cos(t1+t2-t3)-9\,\cos(t1-t2+t3)-\cos(t1+t2+t3)}{80} \\ \frac{-(3\,\sin(t1-t2-t3)+3\,\sin(t1+t2-t3)+9\,\sin(t1-t2+t3)+\sin(t1+t2+t3))}{40\,\sqrt{2}} \\ \frac{4-3\,\cos(t1-t2-t3)-3\,\cos(t1+t2-t3)+9\,\cos(t1-t2+t3)+\cos(t1+t2+t3)}{80} \end{pmatrix} \end{aligned} \tag{116}$$

$$\tilde{H}^{LSls}_{M;\lambda}(^3S_1 \to a_2\omega, L = 2, S = 1, l = 2)$$

$$\begin{aligned}
H_{1;\lambda} &= \begin{pmatrix} \frac{4-3\,\cos(t0-t2)-3\,\cos(t0-2\,t1-t2)+\cos(t0+t2)+9\,\cos(t0+2\,t1+t2)}{80} \\ \frac{3\,\sin(t0-t2)+3\,\sin(t0-2\,t1-t2)+\sin(t0+t2)+9\,\sin(t0+2\,t1+t2)}{40\,\sqrt{2}} \\ \frac{4+3\,\cos(t0-t2)+3\,\cos(t0-2\,t1-t2)-\cos(t0+t2)-9\,\cos(t0+2\,t1+t2)}{80} \end{pmatrix}^T \\
H_{2;\lambda} &= \begin{pmatrix} \frac{-(-3\,\sin(t0-t2)-3\,\sin(t0-2\,t1-t2)+\sin(t0+t2)+9\,\sin(t0+2\,t1+t2))}{40\,\sqrt{2}} \\ \frac{3\,\cos(t0-t2)+3\,\cos(t0-2\,t1-t2)+\cos(t0+t2)+9\,\cos(t0+2\,t1+t2)}{40} \\ \frac{-3\,\sin(t0-t2)-3\,\sin(t0-2\,t1-t2)+\sin(t0+t2)+9\,\sin(t0+2\,t1+t2)}{40\,\sqrt{2}} \end{pmatrix}^T \\
H_{3;\lambda} &= \begin{pmatrix} \frac{4+3\,\cos(t0-t2)+3\,\cos(t0-2\,t1-t2)-\cos(t0+t2)-9\,\cos(t0+2\,t1+t2)}{80} \\ \frac{-(3\,\sin(t0-t2)+3\,\sin(t0-2\,t1-t2)+\sin(t0+t2)+9\,\sin(t0+2\,t1+t2))}{40\,\sqrt{2}} \\ \frac{4-3\,\cos(t0-t2)-3\,\cos(t0-2\,t1-t2)+\cos(t0+t2)+9\,\cos(t0+2\,t1+t2)}{80} \end{pmatrix}^T \end{aligned} \tag{117}$$

B The Relevant Riemann Sheets for T-Matrix Poles of $a_0(980)$ and $h_1'(1380)$

The relevant T-matrix poles are on the Riemann sheet closest to the physical region (sheet I, $Im\, q_i > 0$). For the two-channel case, depending on the righthand cuts of the complex energy plane ($E = m - i\Gamma/2$) given by the energy thresholds E_1 and E_2 of the two channels, one finds the relevant poles on sheet II or III [65]. It is useful to consider the "origins" of the poles which one obtains by switching off the coulpling to the second channel. For the one pole case, the "origin" coincide with the K-matrix pole (see sec. 8.3). For the $a_0(980)$ the fitted K-matrix pole is above both thresholds E_1, E_2 where the physical sheet (sheet I) is connected directly with sheet III and hence with the pole on sheet III (fig. 60a). In contrast, the "origin" of the $h_1'(1380)$ is below the second threshold and the relevant pole therefore on sheet II (fig. 60b).

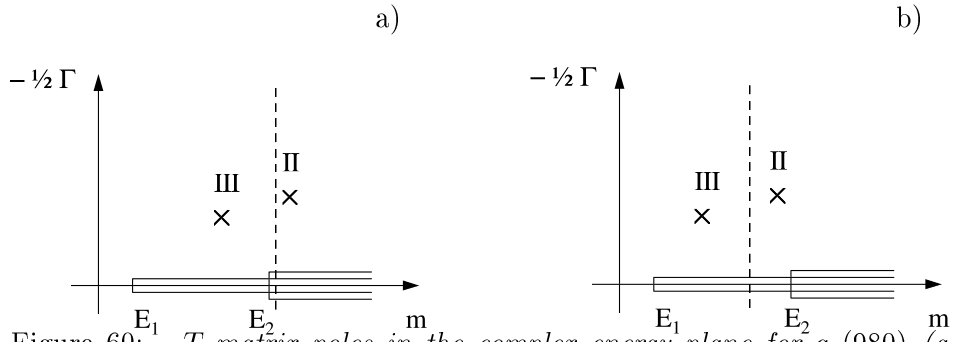

Figure 60: *T-matrix poles in the complex energy plane for $a_0(980)$ (a) and $h_1'(1380)$ (b) with the fitted K-matrix mass pole m_0 (dashed line). The relevant pole for $a_0(980)$ is on sheet III and for $h_1'(1380)$ on sheet II (see text).*

C The Coupling of $h_1' \to \omega\eta$ and $h_1' \to K^*\overline{K}$ According to $SU(3)$-Flavor Symmetry

From $SU(3)$-flavor symmetry, assuming the relative creation of $u\bar{u}$ or $d\bar{d}$ versus $s\bar{s}$ is equally propable, the flavor independent coupling to the sea quarks is given in terms of the transition amplitude M by

$$g_0 = \langle\, q\overline{q} \mid M \mid q\overline{Q}, Q\overline{q}\,\rangle \; . \tag{118}$$

The coupling g_0 depends on the $SU(3)$ nonet membership of the mother and the daugther particles and on the quantum numbers L, S of the final state. For the reactions $h_1' \to \omega\eta$ and $h_1' \to K^0\bar{K}^{*\,0}{+}cc.$ the coupling to the sea quarks is therefore equal. The involved particles expressed in terms of $q\bar{q}$ states and $SU(3)$ mixing angles ϕ, ψ and α, describing the mixing of the pseudovector, the vector and the axialvector mesons, are defined by

$$\begin{aligned}
|\,\omega\,\rangle &= \sin\psi\,|\,n\bar{n}\,\rangle + \cos\psi\,|\,s\bar{s}\,\rangle \\
|\,\eta\,\rangle &= \cos\phi\,|\,n\bar{n}\,\rangle - \sin\phi\,|\,s\bar{s}\,\rangle \\
|\,K^0\,\rangle &= |\,d\overline{s}\,\rangle \\
|\,h_1'\,\rangle &= \cos\alpha\,|\,n\bar{n}\,\rangle - \sin\alpha\,|\,s\bar{s}\rangle
\end{aligned}$$

while

$$|\,n\overline{n}\,\rangle = \sqrt{\frac{1}{2}}\,\left(|\,u\overline{u}\rangle + |\,d\overline{d}\,\rangle\right) \; .$$

The final states are then given by

$$\begin{aligned}
|\,1\,\rangle &= |\,K^0\bar{K}^{*\,0}{+}\,cc., I{=}0,\, C{=}{-1}\,\rangle = \sqrt{\frac{1}{2}}\,\left(|\,d\overline{s}, s\overline{d}\,\rangle + |\,s\overline{d}, d\overline{s}\,\rangle\right) \\
|\,2\,\rangle &= |\,\omega,\eta\,\rangle = \sin\psi\cos\phi\,|\,n\overline{n}, n\overline{n}\rangle - \cos\psi\sin\phi\,|\,s\overline{s}, s\overline{s}\rangle \; .
\end{aligned}$$

Applying eq. (118) one finds for the couplings of the h_1' to the final states:

$$\begin{aligned}
\langle\, h_1' \mid M \mid 1\,\rangle &= \cos\alpha\langle n\overline{n} \mid M \mid 1\,\rangle + \sin\alpha\langle s\overline{s} \mid M \mid 1\,\rangle \\
&= g_0\big(\frac{1}{2}\cos\alpha - \sqrt{\frac{1}{2}}\sin\alpha\big) && (119) \\
\langle\, h_1' \mid M \mid 2\,\rangle &= \cos\alpha\langle n\overline{n} \mid M \mid 2\,\rangle + \sin\alpha\langle s\overline{s} \mid M \mid 2\,\rangle \\
&= g_0\left[\sqrt{\frac{1}{2}}\sin\psi\cos\phi\cos\alpha + \cos\psi\sin\phi\sin\alpha\right] && (120)
\end{aligned}$$

with

$$\begin{aligned}
\langle\, n\overline{n} \mid M \mid 1\,\rangle &= \sqrt{\frac{1}{2}}\sqrt{\frac{1}{2}}\,\langle d\overline{d} \mid M \mid d\overline{s}, s\overline{d}\rangle = \frac{1}{2}\,g_0 \\
\langle\, s\overline{s} \mid M \mid 1\,\rangle &= \sqrt{\frac{1}{2}}\,\langle s\overline{s} \mid M \mid s\overline{d}, d\overline{s}\rangle \\
\langle\, n\overline{n} \mid M \mid 2\,\rangle &= \sqrt{\frac{1}{2}}\,\frac{1}{2}\,\sin\psi\,\cos\phi\,(\langle u\overline{u} \mid M \mid u\overline{u}, u\overline{u}\,\rangle + \langle d\overline{d} \mid M \mid d\overline{d}, d\overline{d}\,\rangle) \\
\langle\, s\overline{s} \mid M \mid 2\,\rangle &= -\cos\psi\,\sin\phi\,\langle s\overline{s} \mid M \mid s\overline{d}, d\overline{s}\rangle
\end{aligned}$$

Taking into account the isospin factor 2 for $h_1' \to K\bar{K}^* + cc.$ one gets the ratio of the couplings

$$R \;=\; \frac{g^2(h\to\eta\omega\,)}{g^2(h\to K\overline{K}^*)} = \frac{(2\sin\alpha\cos\psi\sin\phi + \sqrt{2}\cos\alpha\sin\psi\cos\phi)^2}{2\,(\cos\alpha - \sqrt{2}\sin\alpha)^2}\;. \qquad (121)$$

References

[1] R.P. Feynman in "The Best Short Works of Richard Feynman", Perseus Books, Reading, Mass. 1999

[2] C. Amsler and F.E. Close, "Is $f_0(1500)$ a scalar glueball?", Phys. Rev. **D 53** (1996) 295

[3] C. Amsler et al. (Crystal Barrel Collab.), "A high-statistics study of $f_0(1500)$ decay into $\pi^0\pi^0$", Phys. Lett. **B342** (1995) 433

C. Amsler et al. (Crystal Barrel Collab.), "A high-statistics study of $f_0(1500)$ decay into $\eta\eta$", Phys. Lett. **B353** (1995) 571

C. Amsler et al. (Crystal Barrel Collab.), "A study of $f_0(1500)$ decays into 4 π^0's in proton antiproton annihilation into 5 π^0's at rest", Phys. Lett. **B380** (1996) 453

C. Abele et al. (Crystal Barrel Collab.), "Observation of $f_0(1500)$ decay into K_LK_L", Phys. Lett. **B384** (1996) 425

[4] A. Abele et al. (Crystal Barrel Collab.), "Exotic $\eta\pi$ state in $\bar{p}d$ annihilation at rest into $\pi^-\pi^0\eta p_{spectator}$", Phys. Lett. **B 423** (1998) 175

A. Abele et al. (Crystal Barrel Collab.), "Evidence for a $\pi^0\eta$-wave with odd angular momentum in antiproton-proton-annihilations at rest into $\pi^0\pi^0\eta$", Phys. Lett. **B 446** (1999) 349

[5] P.E. Eugenio, "The search for new mesons in the $\omega\eta$ and $\omega\pi$ systems produced in the reaction $\pi^-p \to \pi^+\pi^-4\gamma n$ at 18 GeV/c", Ph.D. thesis, University of Massachusetts Amherst, 1998

[6] M. Gell-Mann, Y. Ne'eman, "The Eightfold Way", review and collected reprints, New York, 1964

[7] G. Zweig, "An SU_3 Model for Strong Interaction Symmetry and Its Breaking", CERN 8419/TH.412 (1964) unpublished

[8] C. Caso et al. (Particle Data Group), "Review of Particle Physics", Eur. Phys. J. **C3** (1998)

[9] E. Klempt and K. Peters, "Meson Decays and SU(3)", Proceedings of Hadron 91, 521-528.

[10] D. Aston et al., "Evidence for two strangeonium resonances with J^{PC}=1^{++} and 1^{+-} in K^-p interactions at 11 GeV/c", Phys. Lett. **B201** (1988) 573-578

[11] A. Abele et al. (Crystal Barrel Collab.), "Antiproton-proton annihilation at rest into $K_LK_S\pi^0\pi^0$", Phys. Lett. **B 415** (1997) 280

[12] A. Donnachie et al., “The Decays of the ρ'_1 and ω'_1 mesons”, Z. Phys. **C 51** (1991) 689
A.B. Clegg, A. Donnachie, “Higher vector meson states produced in electron-positron annihilation”, Z. Phys. **C 62** (1994) 455-469

[13] N.N. Achasov and A.A. Kozhevnikov, “ρ''s in analyzing e^+e^- annihilation: MARK III, LASS and ARGUS data”, Phys. Rev. **D 55** (1997) 2663-2671

[14] D. Aston et al., “Observation of an $\omega\pi^0$ state of mass 1.25 GeV produced by photons of energy 20 GeV - 70 GeV”, Phys. Lett. **92B** (1980) 211 D. Aston et al., “Evidence for $\rho_1(1270)$ production in the reaction $K^-p \to \pi^+\pi^-\Lambda$”, Nucl. Phys. Proc. Suppl. **21** (1991) 105

[15] S.I. Bityukov et al., “Study of a possible exotic $\phi\pi^0$ state with a mass of about 1.5 GeV/c^2”, Phys. Lett. **B 188** (1987) 383

[16] F.E. Close and H.J. Lipkin, “New experimental evidence for four quark exotics: The Serpukhov $\phi\pi$ resonance and the GAMS $\eta\pi$ enhancement”, Phys. Lett. **B 196** (1987) 245-250

[17] A. Abele et al.(Crystal Barrel Collab.), “High-mass ρ-meson states from $\bar{p}d$-annihilation at rest into $\pi^-\pi^0\pi^0 p_{spectator}$”, Phys. Lett. **B 391** (1997) 191

[18] A. Abele et al. (Crystal Barrel Collab.), “$\bar{p}p$ annihilation at rest into $K_L K^\pm \pi^\mp$”, Phys. Rev. **D 57** (1998) 3860

[19] Mahiko Suzuki, “Axial-Vector meson mixing in orthocharmonium decays”, Phys. Rev. **D 55** (1997) 2840

[20] P. Geiger and E.S. Swanson, “Distinguishing among strong decay models”, Phys. Rev. **D50** (1994) 6855-6882

[21] N.A. Törnqvist, “The Axial Mesons in the Unitarized Quark Model”, University of Helsinki HU-TFT81-37 (1981) preprint, Nucl. Phys. **B203** (1982) 268

[22] T. Barnes et al., “Higher Quarkonia”, Phys. Rev. **D55** (1996) 4157-4188

[23] M. Atkinson et al., “A peak in the $\eta\omega$ mass spectrum from diffractive photoproduction”, Z. Phys. **C 34** (1987) 303-306

[24] Y.D. Prokoshkin and V.D. Samoilenko, “Discovery of a narrow 1650 MeV meson decaying into the $\omega\eta$ channel”, Phys. Dokl. **41** (1996) 247

[25] C. Amsler et al. (Crystal Barrel Collab.), “Coupled channel analysis of $\bar{p}p$ annihilation into $\pi^0\pi^0\pi^0$, $\pi^0\eta\eta$ and $\pi^0\pi^0\eta$”, Phys. Lett. **B 355** (1995) 425

[26] C.J. Batty, “S- and P-state annihilation in $\bar{p}p$ interactions at rest”, Nucl. Phys. **A 601** (1996) 425-444

[27] C. Amsler, "Proton-Antiproton annihilation and meson spectroscopy with Crystal Barrel", Rev. Mod. Phys. **70** (1998) 1293-1340

[28] M.G. Sapozhnikov, "Experimental Results on Stangeness Production", Proc. LEAP 98 Conf., Villasimius, Italy, Nucl. Phys. **A655** (1999) 151-160

[29] C. Amsler et al. (Crystal Barrel Collab.), "Antiproton-proton annihilation at rest into $\omega\pi^0\pi^0$", Phys. Lett. **B 311** (1993) 362

[30] C. Amsler et al. (Crystal Barrel Collab.), "Study of antiproton-proton annihilation at rest into $\omega\eta\pi^0$", Phys. Lett. **B 327** (1994) 425

[31] R. Bizzarri et al., "Experimental results on the $\omega\pi$ and $\pi\pi$ systems as observed in the $\bar{p}p$ annihilations at rest: $\bar{p}p \to \omega^0\pi^+\pi^-$", Nucl. Phys. **B 14** (1969) 169

[32] S.U. Chung, L. Montanet, S. Reucroft, "Analysis of the annihilation process $\bar{p}p \to \pi^+\pi^-\omega$ at rest using Venziano-type amplitudes", Nucl. Phys. **B 30** (1971) 525-534

[33] P. Frenkiel et al., "Resonance production in six prong $\bar{p}p$ annihilations at 2.5 GeV/c", Nucl. Phys. **B 47** (1972) 61

[34] P. Weidenauer et al., "$N\bar{N}$ annihilation at rest into five pions", Z. Phys. **C 59** (1993) 387-398

[35] E. Aker et al.(Crystal Barrel Collab.), "The Crystal Barrel Spectrometer at LEAR", Nucl. Instr. and Meth. **A 321** (1992) 69-108

[36] D.J. Simon, "The CERN PS Complex: A Versatile Particle Factory", CERN PS-96-019 (1996)

[37] A. Abele et al. (Crystal Barrel Collab.), "Measurement of the $\omega \to \eta\gamma$ decay branching ratio", Phys. Lett. **B 411** (1997) 361

[38] C. Amsler et al. (Crystal Barrel Collab.), "Observation of a scalar resonance decaying to $\pi^+\pi^-\pi^0\pi^0$ in $\bar{p}p$ annihilation at rest", Phys. Lett. **B 322** (1994) 431

[39] O. Czyzewski, "Three-Body Final State", published in "Kinematics and Multiparticle Systems", ed. by M. Nikoliç, New York, 1968, 87-113

[40] F.-H. Heinsius,T. Kiel, P. Schmidt, "BCTRAK - Crystal Reconstruction Software", CB-note **92** (1995)
M. Burchell, M. Doser, "GTRACK - Global Tracking Software", CB-note **118** (1995)
G. Folger, "CBOFF - Crystal Barrel Offline Software", CB-note **121** (1995)

F.H. Heinsius, “CCDBCB - Calibration Constants Database Software”, CB-note **122** (1991)
P. Hidas, “CBKFIT - Kinematic Fitting Software”, CB-note **138** (1997)
R. Bossingham, “CBGEANT - Monte Carlo Software”, CB-note **169** (1992)
N.P. Hessey, “Splitoff recognition with Dolby-C”, CB-note **199** (1997)

[41] CERN Program Library entry **Q121** Version (1998) 2.09/18
“PAW, Physics Analysis Workstation, An Introductory Tutorial”, CERN Program Library Long Writeup Q506 (1995)

[42] F. James and M. Roos, CERN Program Library entry **D506** (1994-1998) Version 96.03
F. James, “MINUIT, Reference Manual”, CERN Program Library Long Writeup D506 (1998)

[43] A. Abele et al. (Crystal Barrel Collab.), “Study of $\overline{p}p \to \eta\pi^0\pi^0\pi^0$ at rest”, Nucl. Phys. **B 514** (1998) 45

[44] C. Amsler et al. (Crystal Barrel Collab.), “High-statistics study of $f_0(1500)$ decay into $\pi^0\pi^0$”, Phys. Lett. **B 342** (1995) 433

[45] C. Amsler et al. (Crystal Barrel Collab.), “Observation of a new $I^G(J^{PC}) = 1^-(0^{++})$ resonance at 1450 MeV”, Phys. Lett. **B 333** (1994) 277

[46] C. Amsler et al. (Crystal Barrel Collab.), “High-statistics study of $f_0(1500)$ decay into $\eta\eta$”, Phys. Lett. **B 353** (1995) 571

[47] P. Illinger, “Zerfall von Protonium in $\pi^0\pi^0\pi^0\pi^0$”, Ph.D. thesis, Ludwig-Maximilians-Universität München, 1994

[48] A. Amsler et al. (Crystal Barrel Collab.), “Antiproton-proton annihilation at rest into two-body final states”, Z. Phys. **C 58** (1993) 175

[49] C. Amsler et al. (Crystal Barrel Collab.), “E decays to $\eta\pi\pi$ in $\overline{p}p$ annihilation at rest”, Phys. Lett. **B 358** (1995) 389

D. Urner, “Search for E/ι to $\eta\pi\pi$ in Proton-Antiproton Annihilation at Rest”, Ph.D. thesis, University of Zurich, 1995

[50] D. Herndon, P. Söding and R.J: Cashmore, “A Generalized Isobar Model Formalism”, Phys. Rev. **D 11** (1975) 3165

[51] M. Jacob and G.C. Wick, “On the General Theory of Collisions for Particles with Spin”, Ann. Phys. **7** (1959) 404-428

[52] S.U. Chung, “Spin Formalisms”, CERN Yellow Report 71-8 (1971)

[53] C. Amsler and J.C. Bizot, "Simulation of Angular Distributions", Comput. Phys. Commun. **30** (1983) 21

[54] S.U. Chung, "General formulation of covariant helicity-coupling amplitudes", Phys. Rev. **D 57** (1998) 431

[55] J.D. Hansen et al., "Formalism and Assumptions Involved in Partial-Wave Analysis of three-Meson Systems", Nucl. Phys. **B 81** (1974) 403

[56] S.M. Berman and M. Jacob, "Systematics of Angular and Polarization Distributions in Three-Body Decays", Phys. Rev. **139** (1965) B1023

[57] J.D. Richman, "An Experimenter's Guide to the Helicity Formalism", Pasadena, 1968, CALT-68-1148

[58] F. v. Hippel and C. Quigg, Phys. Rev. **D 5** (1972) 624

[59] C. Amsler, "Spin simulation program SPIN", CB-note **153** (1991)

[60] I.J.R. Aitchison, "The K-Matrix Formalism for Overlapping Resonances", Nucl. Phys. **A 189** (1972) 417-423

[61] S.U. Chung, J. Brose, R. Hackmann, E. Klempt, S. Spanier, and C. Strassburger, "Partial wave analysis in K-Matrix formalism", Ann. Phys. **4** (1995) 404-430

[62] S.M. Flatté et al., "Analysis Of The Observed Anomaly in $\pi\pi$ S Wave Scattering Near $K\overline{K}$ Threshold", Phys. Lett. **B 38** (1972) 232

S.M. Flatté, "Coupled-Channel Analysis of the $\pi\eta$ and $K\overline{K}$ Systems Near $K\overline{K}$ Threshold", Phys. Lett. **B 63** (1976) 224

[63] G.F.Chew, "Resonances, Particles and Poles from the Experimenter's Point of View", University of California, Berkeley, 1966, Report UCRL-16983

[64] R.J. Eden, P.V. Landshoff, D.I. Olive, J.C. Polkinghorne, "The Analytic S-Matrix", 1966, Cambridge

[65] A.M. Badalyan, L.P. Kok, M.I. Polikarpov, Y.A. Simonov, "Resonances in Coupled Channels in Nuclear and Particle Physics", Phys. Rept. **82** (1982) 31

[66] T.F. Degener, "TARA - an object-oriented program for a partial wave analysis of sequential two body decays", Comput. Phys. Commun. **118** (1999) 34

[67] St. Bischoff, Ph.D. Thesis, University of Karlsruhe, in preparation

[68] A. Abele et al. (Crystal Barrel Collab.), "Antiproton-proton annihilation at rest into $K_L K^{\pm}\pi^{\mp}\pi^0$ – manifestation of isospin interference", Phys. Lett. **B 415** (1997) 289

[69] S. Spanier, "Die Beobachtung einer isovektoriellen 0^{++}-Resonanz mit einer Masse von 1470 MeV/c^2 im $\pi^0\pi^0\eta$-Endzustand der Proton-Antiproton-Vernichtung in Ruhe", Ph.D. thesis, Johannes Gutenberg-Universität Mainz, 1994

[70] S. Spanier, private communication

S. Spanier, "Coupled channel analysis of the $\bar{p}p$-annihilation into $\pi^0\pi^0\pi^0$, $\pi^0\pi^0\eta$ and $\pi^0\eta\eta$ at rest and $\pi\pi$ scattering data", CB-note **274** (1995)

[71] S. Teige et al.(E852 Collaboration), "Properties of the $a_0(980)$ meson", Phys. Rev. **D 59** (1999) 12001
preprint hep-ex/9608017 (1996)

[72] C. Amsler et al.(Crystal Barrel Collab.), "The pseudoscalar mixing angle θ_{PS} from η and η' production in $\bar{p}p$ at rest", Phys. Lett. **B 294** (1992) 451

List of Figures

List of Tables

Acknowledgments

In contemporary particle physics many people contribute to the success of an experiment. I would thus like to thank all members of the Crystal Barrel collaboration for their constant help and support.

In particular I would like to express my gratitude to Professor Claude Amsler, my advisor, for initiating this project and patiently supporting my work. His expertise and knowledge in this research field were important guidelines and contributed significantly to the progress of this work.

I wish to thank Stefan Spanier, who gave me a fast and efficient introduction into partial wave analysis. His experience and help in applying the K-matrix formalism and in the interpretation of the $(\pi\pi)_S$ wave had been very valuable.

I am grateful for many illuminating discussions I had with K. Braune, S.U. Chung, L. Montanet and Č. Zupančič. I appreciated very much their opinion and experience.

Deep acknowledgment belongs to Michael Doser for his valuable help for a lot of the daily problems at CERN, for many discussions on physics and beyond and for his English support. His and Silvia Wyder's hospitality contributed considerably to the pleasant atmosphere I encountered at CERN and in Geneva.

I wish to thank the whole Zurich group for their support and the inspiring working atmosphere, particularly Matthias Heinzelmann, Farid Ould-Saada, Christian Regenfus and Sven von Dombrowski whose experience in the analysis of the Crystal Barrel data has been very fruitful for me.

Finally I am especially indebted to my friends and of course to Regula Waldis for their patience and understanding during all the time of my thesis work.

This thesis was supported by the Swiss National Science Foundation.

Curriculum Vitae

Personalien

Name	Giarritta
Vorname	Peppino Beat
Geboren	25.12.1966, Schwyz
Bürgerort	Schwyz und Patti (Italien)

Bildungsgang

1974-1980	Primarschule Rickenbach (SZ)
1980-1987	Mathematisch-Naturwissenschaftliches Gymnasium an der Kantonsschule Kollegium Schwyz
1987-1995	Studium der Physik (Mathematik, Geophysik) an der Universität Zürich
1995	Diplom in Experimentalphysik Diplomarbeit: ”Aufbau eines Flash-ADC Auslesesystems für die Messung des magnetischen Moments des Neutrinos“ unter der Leitung von Prof. Dr. C. Amsler und Dr. F. Ould-Saada
1995-1999	Wissenschaftliche Mitarbeit beim MUNU Neutrino Experiment in Bugey und beim Crystal Barrel Experiment am LEAR (CERN) in Genf. Dissertation bei Prof. Dr. C. Amsler, ”Search for New Mesons in Antiproton-Proton Annihilation into $\omega\pi^0\pi^0$ and $\omega\eta\pi^0$“

Dozentenverzeichnis

H. Amann
C. Amsler
D. Brinkmann
E. Brun
M. Carrier
R. Engfer
P. Gabriel
G. Karrer
W. Kündig
W. Lowrie
M. Mali
P.F Meier
St. Müller
R.E. Pixley
R. Rasche
P. Schaber
B. Schmid
N. Straumann
U. Straumann
A. Thellung
P. Truöl
D. Wyler